High-accuracy laser spectroscopy of the molecular hydrogen ion H_2^+

Inaugural-Dissertation

zur Erlangung des Doktorgrades
der Mathematisch-Naturwissenschaftlichen Fakultät
der Heinrich-Heine-Universität Düsseldorf

vorgelegt von

Magnus Roman Schenkel
aus Bad Tölz

Düsseldorf, July 2025

aus dem Institut für Experimentalphysik
der Heinrich-Heine-Universität Düsseldorf

Contents

Eidesstattliche Versicherung

Ich versichere an Eides statt, dass die Dissertation von mir selbstständig und ohne unzulässige fremde Hilfe unter Beachtung der "Grundsätze zur Sicherung guter wissenschaftlicher Praxis an der Heinrich-Heine-Universität Düsseldorf" erstellt worden ist.

Düsseldorf, 09.07.2025

Magnus Roman Schenkel

Abstract

To explore the limits of contemporary knowledge is a prime objective of studies in fundamental physics. The group of systems of molecular hydrogen ions (MHIs) offers many prospects in this regard: From spectroscopic data, one may extract fundamental constants or test theoretical predictions. MHI spectroscopy, in particular that of HD^+, has undergone exceptional progress in recent years. A key achievement has been the recent determination of the ratio of its reduced nuclear mass to the electron mass with state-of-the-art precision.

However, in order to extract generally applicable constants from spectroscopic data of HD^+, such as the proton-electron mass ratio, it is necessary to combine it with data from other experiments. In particular, the deuteron-proton mass ratio, obtained from cyclotron frequency measurements in Penning traps. To avoid this dependency and obtain purely spectroscopic values, an alternative approach is to measure transition frequencies in the closely related molecule H_2^+. But, despite its unique status as the simplest molecule in the universe, the highly accurate measurements necessary for such an endeavor have so far remained elusive, due to the experimental challenges posed by H_2^+.

This thesis will demonstrate how these challenges can be overcome through the development of a capable spectroscopy laser system and its integration into a spectroscopy apparatus with a linear radio-frequency ion trap at its core. The laser system is characterized and found to have a relative frequency stability of better than 1×10^{-14} over timescales between 1 and 10^7 seconds, coupled with a frequency accuracy relative to the SI second of a similar magnitude. Its output power is at the watt-level; sufficiently high in order to drive electric-quadrupole transitions in molecular hydrogen ions. The combination of the spectroscopy laser and the ion trap allows for two spectroscopic studies based on laser excitation of H_2^+ to be performed.

The initial study encompasses the observation of a Doppler-broadened rovibrational transition in H_2^+, thereby achieving an experimental objective that was envisioned decades ago. This observation is accompanied by the first study of systematic effects on an electric-quadrupole transition in a molecular ion, specifically of Doppler-free single Zeeman components in HD^+. These results represent only the second time that an electric-quadrupole transition has been observed in a molecular ion, but with a precision that is a factor $\sim 10^6$ greater than that of the first observation. The study demonstrates that achieving ultra-high accuracy for this type of transition is a realistic prospect.

The second study improves the H_2^+-result, surpassing the Doppler-effect and achieving a relative accuracy of the transition frequency of 8×10^{-12}. This represents the most accurate measurement of any H_2^+ property to date, exhibiting a factor of $\simeq 10^3$ improvement over the previous record. The obtained line resolution also surpasses the highest resolution achieved with HD^+. By combining the measurement with theory and constants obtained from hydrogen spectroscopy, the proton-electron mass ratio is derived with an accuracy similar to that of the current CODATA standard and independent of Penning trap mass spectrometry. It is the first time that this fundamental mass ratio has been derived from spectroscopic data alone. The values for the mass ratio, obtained through different experiments and theories, are in agreement.

Furthermore, the result may be combined with HD^+ data in order to yield the deuteron-proton mass ratio with similar accuracy. Alternatively, the measurements can be compared with theory to result in a test of the underlying theoretical framework, where agreement is found at a relative level of 8×10^{-12}, representing one of the most accurate experiment-theory comparisons in physics.

The work introduces precision spectroscopy of H_2^+ into the field of fundamental physics. The results demonstrate that ultra-high accuracy spectroscopy of transition frequencies of molecular hydrogen ions, specifically of electric-quadrupole transitions, has the potential to become a new standard for the metrology of fundamental constants. Furthermore, this work lays the experimental foundation of a vision proposed decades ago: the comparison of H_2^+ with its antimatter counterpart, the anti-molecule $\overline{H_2}^-$.

1. Molecular hydrogen ions – applications in fundamental physics

The field of fundamental physics is concerned with our elementary understanding of the world we live in. At this level, fundamental theories of physics have been subject to rigorous scrutiny and have undergone significant transformations. Because of this nature, fundamental physics is heavily intertwined with the field of precision physics, in which experiments and theories are compared at the highest level of accuracy. To date, such accuracies have reached a relative level of up to 10^{-12}, demonstrated by some of the most accurate determinations of physical properties: the g-factor measurement of the electron [1] and the transition frequencies of the hydrogen atom. These examples are simple single- and two-particle systems, respectively. This is not surprising, given that such a level of accuracy demands a highly sophisticated theoretical model, the development of which is a daunting task for complex systems.

Where to draw the line between simple and complex systems may not be without discussion. However, in all cases, the logical next step in the progression of complexity would be that of three-particle systems. Among this category are the simplest molecules, the molecular hydrogen ions (MHIs). This group encompasses all molecules consisting of a single electron and two singularly positively charged nuclei. Given that three variants of such nuclei are known, namely the proton, the deuteron, and the triton, the group consists of three homonuclear isotopologues (H_2^+, D_2^+, T_2^+) and three heteronuclear isotopologues (HD^+, HT^+, DT^+). This distinction is much more relevant as it may seem at first glance, since symmetry or asymmetry between the center of mass and the center of charge of the two nuclei each lead to far reaching consequences. Being such simple, yet complex systems, they are at the intersection of calculable and interesting systems. They are sufficiently complex to be subject to a multitude of fundamental interactions and potential new physics, while still retaining adequate simplicity to allow for rigorous theoretical calculations. Consequently, they are ideal candidates to join single and two particle systems in the realm of precision physics and contribute to the ongoing endeavor of testing our theoretical models and our understanding of the universe.

The underlying theory for all these systems is quantum electrodynamics (QED). As a result of its ability to accurately describe a multitude of phenomena and systems, including those previously mentioned, it has been designated as the most accurate theory in physics and is also regarded as one of the most tested ones. As is the case for one- and two-particle systems, highly accurate predictions of MHIs' quantum mechanical energy levels are calculated within the framework of QED. It is therefore unsurprising that all aims of MHI studies involve QED to some extent. Two principal approaches may be distinguished: One may either assume the theory to be correct in order to extract fundamental constants or test the theoretical framework for correctness and completeness by comparing it with measurements.

This dissertation is dedicated to the pursuit of ultra-high accuracy spectroscopy of H_2^+ in order to contribute to the aspiration of an ever-better understanding of our world at an elementary

level. The structure is as follows: A general overview of the main objectives of MHI fundamental physics studies is presented in Fig. 1.1 and discussed in greater detail in the subsequent Sections 1.1 and 1.2, followed by a discussion of the particular relevance of the MHIs H_2^+ and HD^+ in Sec. 1.3. In particular, the importance of studies on H_2^+ will be highlighted to provide motivation for the work presented in this thesis. A brief introduction into the theory and a review of undertaken experiments with H_2^+ will be given in Chapter 2. For a more comprehensive introduction, the reader is directed to [2]. In Chapter 3 the aims of this thesis will be discussed, with details of the experimental setup and procedures in the subsequent Chapter 4. Chapter 5 will present manuscripts that are relevant to and developed in connection to this thesis, while a summary of their results is given in Chapter 6. Chapter 7 will conclude the work with an outlook.

1.1. Determination of fundamental constants

Two groups of fundamental constants can be distinguished: Those that describe an attribute of a particle, such as mass or charge, and those that define a scale between a physical interaction and the measured value, e.g. the Planck constant. Yet, all of these constants have in common that they are fundamental in the sense that their numerical value does not result from the theoretical model in which they are employed. Instead, their values must be obtained through alternative means, which in the majority of cases is through measurement. In order to perform this procedure, the theoretical model is essential; it defines the relationship between the measured property, the constants, and the physical interactions. For example, if a model describes a property A as depending on a set of constants $\{c_i, c_j, ...\}$, one may set up the equation

$$A^{(\text{expt})} \overset{!}{=} A^{(\text{theor})} (c_i, c_j, ...) \,, \tag{1.1}$$

where "expt" and "theor" correspond to the experimentally measured and theoretically predicted value, respectively. Assuming the constants to be unknown, their value can be determined by imposing the correctness of the equation. Obviously, since already in the above example the property depends on multiple constants, a single measurement does not contain sufficient information. At the same time, there may exist multiple measurements of various properties that have a partial or total overlap with respect to the set of constants they depend on. Moreover, there can be correlations between different properties and constants which should be taken into account.

A general and maximal unbiased method for determining a set of constants that best describes all measurements and additional information is therefore required. One possibility is to set up an equation similar to eq. 1.1 for each measured property and then adjust the set of constants until, on average, all equations are best-matched. In light of the abundance of measurements and corresponding models in today's world, this is a demanding task. Nevertheless, the task can be completed, which is done by the Committee on Data (CODATA) of the International Science Council. Typically, updated values for fundamental constants are published every four years, providing a set of reference values based on the most accurate measurements and their models. The most recent set of constants has been published and is abbreviated in this work as "CODATA22" [3]. Note that a detailed description of their determination, similar to that provided for the preceding set ("CODATA18", [4]), is available at this point in time only as a pre-print [5].
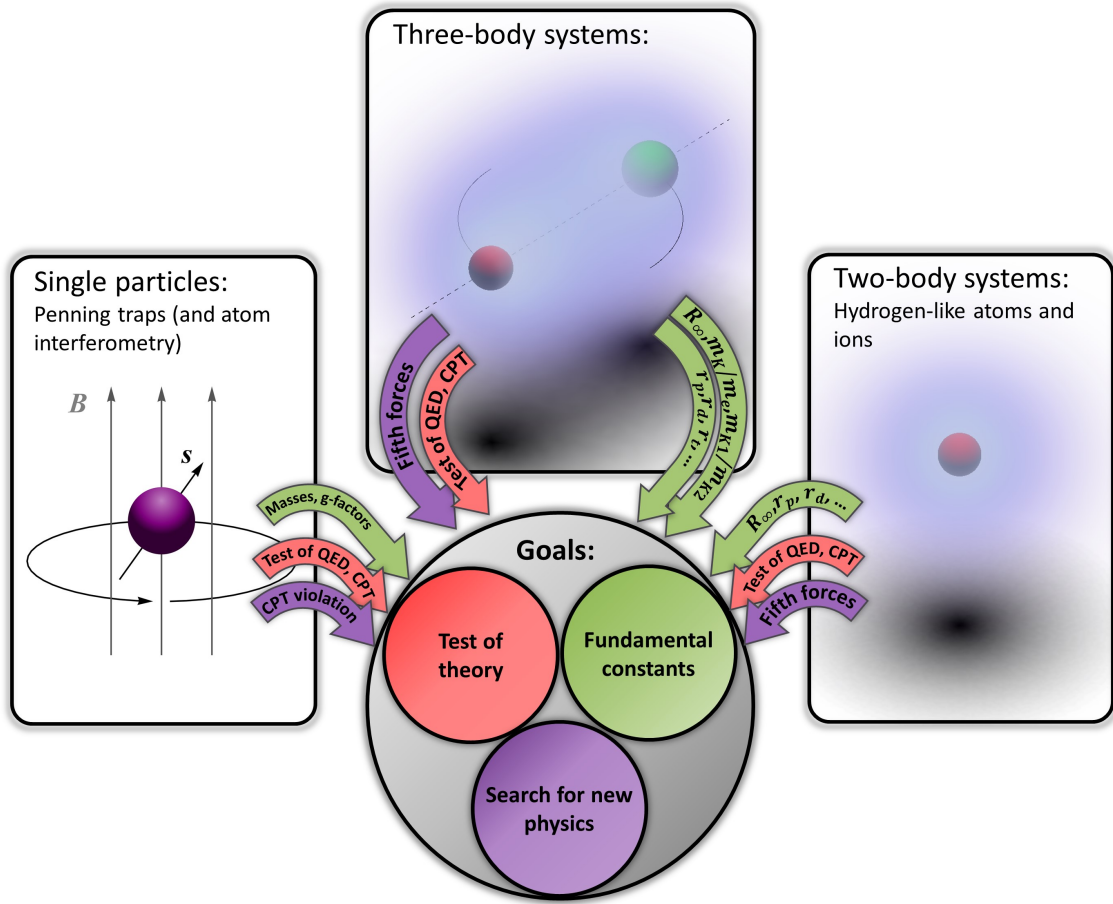
Figure 1.1.: Goals of studies with "simple" systems. Three groups of systems are distinguished: single, two- and three-body systems. For each group, an example is shown. Respectively they are: a single particle with its spin precessing in a Penning-trap (left), the hydrogen atom with the electron cloud in the ground state (right) and a molecular hydrogen ion with a similar depiction for the electron (center-top). In the latter two examples, the size of the nuclei is exaggerated, and the "shadow" beneath both electron clouds is their center cross-section. The arrows and corresponding labels illustrate the type of information that can be contributed by each system to the encircled goals in the center-bottom. The arrows' colors are chosen to match with the most closely related goal. It should be noted that the example systems and arrows are not exhaustive; for instance other three-body systems, such as helium or helium-like ions, may offer similar or other prospects as MHIs. Additionally, the shown systems may offer other possibilities for contributing to research goals that are not shown. The term "single particles" is used loosely in the context of this figure, including also multiple particle systems that are subject to an environment in which their composition can be neglected (e.g. atom interferometry). QED: quantum electrodynamics. CPT: charge-parity-time conjugation.

Table 1.1.: Values of constants relevant for the computation of MHI transition frequencies for both recent data sets CODATA18 and CODATA22. A value for r_t is not provided by CODATA, instead the value is taken from [6].

Constant (unit)	Rydberg constant cR_∞ (Hz)		
CODATA18	$3.289\,841\,960\,2508(64) \times 10^{15}$		
CODATA22	$3.289\,841\,960\,2500(36) \times 10^{15}$		
,,	mass ratios		
	m_p/m_e	m_d/m_p	m_t/m_p
	$1\,836.152\,673\,43(11)$	$1.999\,007\,501\,39(11)$	$2.993\,717\,034\,14(15)$
	$1\,836.152\,673\,426(32)$	$1.999\,007\,501\,2699(84)$	$2.993\,717\,034\,03(10)$
,,	nuclear charge radii		
	r_p (m)	r_d (m)	r_t (m)
	$8.414(19) \times 10^{-16}$	$2.127\,99(74) \times 10^{-15}$	-
	$8.4075(64) \times 10^{-16}$	$2.127\,78(27) \times 10^{-15}$	-
[6]	-	-	$1.7591(36) \times 10^{-15}$

MHI studies may contribute to this endeavor. Owing to a highly advanced theoretical model for transition frequencies f between two internal states, an equation of the form of eq. 1.1 can be set up. In the case of rovibrational transition frequencies of MHIs, the most relevant constants are the Rydberg constant R_∞, the mass ratio of the reduced nuclear mass μ to the electron mass m_e, and the charge radii of any involved nucleus r_i, such that eq. 1.1 can be written in the specific form

$$f^{(\text{expt})} \overset{!}{=} f^{(\text{theor})}\left(R_\infty, \mu/m_e, r_i\right) . \tag{1.2}$$

Current CODATA reference values for these or related constants are given in Tab. 1.1.

In this context, an important property is the sensitivity of a frequency to a fundamental constant, which also results from the theoretical framework employed. For the transition frequencies, the sensitivities β can simply be defined as the derivative of the frequency to a constant $c_i \in \{R_\infty, r_i, \mu/m_e\}$

$$\beta_{c_i} = \frac{\partial f^{(\text{theor})}}{\partial c_i} .$$

The sensitivities can be used to set up an approximate linearized form of eq. 1.2, by expanding around the theoretical value obtained from the CODATA reference values [7]

$$f^{(\text{expt})} \overset{!}{=} f^{(\text{theor})}\left(R_{\infty,0}, (\mu/m_e)_0, r_{i,0}\right) + \beta_{R_\infty} c\Delta R_\infty + \beta_\lambda \Delta\lambda + \beta_{r_i}\Delta(r_i^2) . \tag{1.3}$$

Here, the subscript "0" denotes the CODATA reference values, and $\Delta c_i = c_i - c_{i,0}$ (note that explicitly $\Delta(r_i^2) = r_i^2 - r_{i,0}^2$). The equation is approximate, since the sensitivities are defined as partial derivatives, and therefore correlations between constants are not taken into account. There is, for example, a strong correlation between R_∞ and r_p [4]. Usually, such correlations are considered in the adjustment algorithm by introducing an additional equation which links the values of the two constants. Equation 1.3 contains an implicit summation over

the index i for heteronuclear MHIs, while it reduces to a single contribution for homonuclear ones. To give a specific example and using the CODATA18 reference values, the transition $(v, N) : (1, 0) \rightarrow (3, 2)$ in H_2^+ (an introduction to these quantum numbers and the type of transition will follow in Sec. 2) can be expressed by the equation [7, 8]

$$
\begin{aligned}
f_{(1,0)\rightarrow(3,2)}^{(\text{expt})} \overset{!}{=} \quad & 124\,487\,032\,442.3 \quad \text{kHz} \\
+ \quad & 0.24 \quad \text{kHz} \times \frac{c\Delta R_\infty}{u\left(cR_{\infty,0}\right)} \\
- \quad & 3.27 \quad \text{kHz} \times \frac{\Delta(m_p/m_e)}{u\left([m_p/m_e]_0\right)} \\
- \quad & 0.16 \quad \text{kHz} \times \frac{\Delta(r_p^2)}{u\left(r_{p,0}^2\right)} .
\end{aligned}
\tag{1.4}
$$

The pure theoretical uncertainty associated with this value is $0.9\,\text{kHz}$, and does not account for the constants' uncertainties. The latter can be immediately calculated from the contributions, which are given in a form relative to the uncertainty of the CODATA18 constants (compare Tab. 1.1). The individual sensitivities will determine the level of accuracy obtainable for a constant, when a certain accuracy is reached through experiment and theory. As illustrated by eq. 1.4, the sensitivity is the highest for the mass ratio. This is not exclusive to the example given here; it is rather a characteristic of all rovibrational transitions in MHIs. The underlying reason can be found already in simple models: the rotary and vibratory motions of the nuclei are strongly dependent on their masses (see Sec. 2.1.1). Importantly, the transition frequency between two rovibrational states exhibits higher sensitivities to the mass ratios when compared to many transition frequencies in atoms. In fact, these sensitivities are larger than those found in the hydrogen atom [2]. This makes MHIs particularly well-suited for the determination of these ratios.

One may distinguish two approaches based on the above procedure.

The first is simply to contribute to the initially discussed endeavor for ever higher accuracy in the fundamental constants. For this to be an attractive prospect, both theory and experiment must become accurate enough to be able to challenge other means of determining the constants. The determination of the MHI frequency (eq. 1.2) could then be considered in the adjustment done by CODATA and contribute to the resulting constants' accuracies. The inclusion of results obtained with the MHI HD^+ in the most recent set CODATA22 [3] demonstrates that this prospect is achievable.

The second approach is to determine an independent value for a constant based on eq. 1.2 and then compare that value to the CODATA reference. In light of the sensitivities discussed above, it is preferable to assume a fixed value for the constants with smaller sensitivity, namely R_∞ and the r_i, and adjust the constant with the highest sensitivity, the mass ratio (values for R_∞ and r_i may then be taken from CODATA). The comparison of the obtained mass ratio with that of CODATA will contain rich information: Firstly, the competitiveness of MHI spectroscopy in determining the mass ratio can be verified. Only if the accuracy of this determination is competitive with the reference value, it can be reasonably expected that the inclusion of the MHI data would significantly affect the CODATA adjustment. Secondly, it will contain a consistency check of both the MHI result and the measurements and models

underlying the CODATA value. This is especially noteworthy when one considers the main historical methodologies employed in the determination MHI-relevant constants. While R_∞ and the charge radii are derived from measurements on atomic hydrogen (both electronic and muonic) involving QED, the mass ratios have been determined primarily through measurements of classical oscillatory motion of particles in a Penning trap. Consequently, an agreement between mass ratios determined from MHI studies and those obtained through measurements of cyclotron frequencies in Penning traps necessitates employment of identical fundamental constants within both underlying theoretical frameworks. This may appear obvious at first glance, but should not be taken for granted, given that two theories with significant conceptual differences are being compared: Quantum mechanics and Newtonian mechanics. Therefore, determining fundamental constants through MHI studies is not just an endeavor to achieve higher accuracy; it also allows for a comparison of two of the most prominent theories of physics.

These two approaches can be pursued with a single transition measurement in MHIs. When considering measurements within multiple MHIs, the possibilities expand [7, 9]. Due to the dependency of transition frequencies on the reduced nuclear mass, different masses of fundamental particles are involved for different MHIs. A combined set of measured transitions of various MHIs would therefore allow for the extraction of the individual mass ratios of proton-electron m_p/m_e, deuteron-electron m_d/m_e, and triton-electron m_t/m_e, rather than of each reduced nuclear mass. For example, a transition frequency in HD$^+$ depends on a combination of m_p/m_e and m_d/m_e. If a measurement of H$_2^+$, that only depends on m_p/m_e, were available in addition to a measurement of HD$^+$, the data could be combined to yield both m_p/m_e and m_d/m_e. Importantly, the exact sensitivity differs for each transition, and as a result, optimized sets of transitions can be found, whose measurement would enable the most sensitive determination of the constants [7]. It is interesting to note that, in such a scenario, an improved determination of the charge radii seems also achievable.

In conclusion, highly accurate values for fundamental constants, especially mass ratios, can be obtained through measuring transition frequencies of MHIs. The resulting values can be compared with those obtained through other methods, realizing a test of agreement of different theoretical frameworks, or alternatively be combined with other data to improve the uncertainty of common constants.

1.1.1. Time dependence of fundamental constants

It has been proposed, that fundamental constants, contrary to their name, are not in fact constant but instead vary in time. Such a variation would have to be extremely small to evade detection to date. The highly precise determination of fundamental constants sought with MHIs, combined with their high sensitivity to some of the constants, makes them natural candidates for searching for the presence or absence of such variations. One approach to achieve this is to repeatedly measure the same transition over time. The presence or absence of a variation in the transition frequency can be used to infer a time-dependence or independence of the involved fundamental constants. For a more detailed discussion, see e.g. [10, 11].

1.2. Comparing with theory and probing for new physics

The determination of fundamental constants assumes the correctness of the theoretical model. It is likewise pertinent to ask if that model is correct.

The most straightforward answer to this question can be obtained through the second approach already discussed in Sec. 1.1: utilize the set of constants provided by CODATA, insert them into MHI theory, and then compare the result with an experimental determination of the same property. In Sec. 1.1 the aim of this comparison was to determine fundamental constants. However, an alternative approach would be to assume the reference values for the constants to be correct and then test whether the theory is able to correctly predict the measured property. In this case, the uncertainty attributed to each constant by CODATA will affect the uncertainty of the theory prediction, thereby limiting the comparison between experiment and theory. Similarly, the theoretical uncertainty stemming from the computation itself can limit this comparison.

An approach to solve these limitations is to compute the ratios of transition frequencies of MHIs, which have been introduced in [7, 12]. The principle idea is to compute the ratio of two transition frequencies that exhibit comparable sensitivity to a certain constant or to the theoretical uncertainty. The influence of these contributions on the ratio, and consequently also the impact of their uncertainty, will be minimized. The idea can be extended by computing the ratios to some power and adequately choosing the power in a manner that minimizes the influence of a specific property. Given the varying dependency of each transition frequency on a given constant and the numerous theoretical terms, it is generally impossible to entirely eliminate all contributions. Nevertheless, the ratios strongly reduce the influence of the specific contributions, thereby facilitating a comparison between theory and experiment that is mostly independent of other measurements, models, and theoretical limits. Note that the ratios may also be computed for two frequencies of different MHI species.

Naturally, an agreement between theory and experiment is not a certainty; rather, there may be a discrepancy. Such a discrepancy may be indicative of an imperfect experiment, for example caused by an error introduced by the experimenter or unknown or improperly calibrated systematic effects. Alternatively, or additionally, it may be indicative of an error in the theoretical computation of the value. In the event that these errors can be entirely excluded, an intriguing possibility presents itself: the theoretical model is unable to accurately describe the physics, necessitating the development of new models to address the shortcoming.

Such new physics are, at the current point in time, of speculative nature and can be investigated in various ways. In the context of MHIs, one example has already been mentioned above: the test of time dependence of fundamental constants (Sec. 1.1.1). Other examples are the comparison of an MHI with its antimatter counterpart, and the search for a potential fifth fundamental force.

1.2.1. Matter-antimatter comparison

QED and as an extension also the Standard Model (SM) of particle physics are theoretical models that are built upon the CPT theorem [13]. It states that the product of charge conjugation (C), parity (P), and time (T) of a particle must be even under reversal. This concept of symmetry is challenged by the observation that there is a strong preponderance of matter in the

universe. As a consequence, phenomenological theories (referred to as "SM extensions") have been developed which consider physics in the presence of small CPT and Lorentz invariance violations.

The CPT theorem can be investigated experimentally by comparing matter and antimatter. Since the current understanding is that these two forms of matter are identical except for the sign of their charge, a comparison between them will investigate the CPT principle. A prominent example of such an undertaking is the Baryon Antibaryon Symmetry Experiment (BASE). Notable recent achievements include the comparison of the proton-antiproton magnetic moment [14] and charge-mass ratios [15] at a relative level of 1.5×10^{-12} and 1.6×10^{-11}, respectively. For both attributes, no difference between matter and antimatter was observed within the limits of the measurements' uncertainties. Similarly, experiments investigating antihydrogen, the antimatter counterpart to the hydrogen atom, have been conducted and have been able to verify CPT invariance at a level of 1.6×10^{-8} [16]. An improved test is anticipated in the near future, based on the recently demonstrated spectroscopic precision of an antihydrogen transition at a relative level of 10^{-12} [17].

Continuing the trend of extending what has been achieved with one- and two-particle systems, it has been proposed to compare H_2^+ with its antimatter counterpart [18]. This is an attractive proposition, as this molecule is more sensitive than hydrogen to a potential asymmetry in the constituents' mass ratios and their hyperfine interactions compared to hydrogen [19]. Additionally, a CPT test based on H_2^+ and anti-H_2^+ would be more encompassing, as it would include interactions between the nuclei. From an experimental point of view, it appears advantageous to pursue because it is charged and therefore easier to confine. One could take advantage of the techniques developed for the antiproton experiments, where antiparticle trapping times of several months have been achieved [20]. However, a necessary requirement in order to compete with the above limits are highly accurate measurements of the energy levels of both H_2^+ and anti-H_2^+. The results presented in this thesis pave the way towards such an experiment. As will be demonstrated, ultra-high precision spectroscopy of H_2^+ is realizable, representing the first, albeit simpler, part of the comparison.

1.2.2. Fifth force

In relation to the four fundamental forces included in the SM, another proposed new model of physical interaction is that of the fifth force. A simple yet general form for such an interaction between two particles is given by the Yukawa-potential

$$V_{\text{Yukawa}}(r) = \beta \frac{e^{-r/\Lambda}}{r} \, ,$$

where r is the separation of the two particles, between which the interaction takes place. The parameters β and Λ are free parameters that describe the strength of the interaction and the range of the potential, respectively.

Since the origin of the force associated with this potential is unknown, it may manifest between any combination of particles that are part of the SM. To investigate all potential combinations, a significant number of experiments is required. This is why it is attractive to study a potential fifth force with MHIs. The different variants contain three of the most abundant SM particles: the proton, the neutron, and the electron. Consequently, they could be sensitive to a force between any combination of these particles.

Due to the uncertainties associated with both experiment and theory, it is impossible to definitively rule out the existence of a potential fifth force. Instead, if an agreement between experiment and theory (one that does not take into account such a force) is found, an upper bound for the interaction strength β, the range of the force Λ, or some combination thereof can be determined. Recently, this could be done for a potential baryon-baryon interaction based on measurements done in HD^+ [12].

1.3. The particular MHIs H_2^+ and HD^+

The aims of MHI studies discussed so far could, in principle, be pursued with any member. However, a clear hierarchy can be defined experimentally. The radioactivity and rarity of tritium render its procurement challenging and expensive, which in turn makes the investigation of MHIs containing it difficult. Excluding it, three isotopologues remain: H_2^+, HD^+ and D_2^+. Of these, HD^+ is the only heteronuclear one and thus the only one that allows for electric-dipole transitions (see Sec. 2.1.4); a clear advantage from an experimental point of view. It is therefore unsurprising that recent experimental studies have focused on this member of the MHI family. These studies have successfully accomplished the majority of goals discussed above in recent years. Key achievements include a competitive determination of the mass ratios involved and a constraint on a potential fifth force between the nuclei [21, 12, 22, 23, 24]. This was made possible by significant advancements in the precision of spectroscopy experiments and a similar progress in theory [25, 26]. However, these achievements would be greatly complemented by results of comparable accuracy in the spectroscopy of H_2^+, for several reasons:

Firstly, the type of mass-related fundamental constants that can be extracted from MHI data is always a convolution of all constituents' individual masses. Specifically for HD^+, the accessible mass ratio is

$$\frac{\mu}{m_e} = \frac{m_p m_d}{(m_p + m_d)} \frac{1}{m_e} \,,$$

where μ is the reduced nuclear mass and m_e, m_p, m_d are the masses of electron, proton and deuteron, respectively. Such a combination, however, is not as relevant as the individual masses or mass ratios would be. It has therefore been customary to make use of the proton-deuteron mass ratios obtained from Penning trap cyclotron frequency measurements [27] in order to obtain the proton-electron mass ratio. An alternative and independent approach is to study H_2^+. Given that H_2^+ is a homonuclear molecule, the constant obtainable from its data is the more attractive and simpler ratio of its nuclear mass to the electron mass, i.e. the proton-electron mass ratio. Furthermore, it is possible to combine H_2^+ and HD^+ spectroscopic data to obtain the proton-electron and deuteron-electron mass ratios, as previously discussed in Sec. 1.1.

A second reason is the potential of a CPT test, by comparing H_2^+ and its antimatter counterpart. Such a test appears to be much more feasible with the simplest MHI, given the inherent challenges associated with generating antimatter molecules. The generation of anti-H_2^+ is actively discussed [28, 29], and is suggested to be feasible based on already experimentally investigated antihydrogen.

A third argument is the aforementioned desire to measure a multitude of transition frequencies in several MHIs, as their combination is predicted to allow for a significant improvement in the determination of fundamental constants [7]. This argument becomes even more relevant

when one considers that the techniques developed for H_2^+ should also be applicable to the other homonuclear MHIs. It is therefore imperative to develop techniques for H_2^+ spectroscopy and to demonstrate that high-accuracy spectroscopy is possible, similar to HD^+.

Finally, there is the issue of the generally complicated internal structure of a transition in MHIs (see Sec. 2.1.3). Understanding and measuring this structure is a necessity for the objectives detailed above. However, a substantial number of measurements are required to fully determine the structure experimentally [2, 30]. This is a daunting task, given that successful experimental techniques have been rather slow. To avoid this issue, recent measurements on HD^+ have had to rely, to some extent, on spin-theory results in order to extract the property of interest: the spin-averaged frequency (for an introduction, see Sec. 2.1.2). An independent experimental verification is highly desirable, given that there has been some tension between theoretical predictions and experimental observations for some of the measurements [31]. In this regard, H_2^+ offers an attractive prospect: special cases exist, for which the spin-structure is drastically simplified and only a few measurements are required in order to fully characterize all components of a transition. The results could then be compared with the theoretical computation. A verification of the theory results would provide greater confidence in its use for transitions, for which a fully experimental approach seems unrealistic. Similarly, the comparison could highlight potential oversights of previous HD^+ experiments.

2. Introduction to H_2^+

This section will provide an introduction to the theoretical framework underlying H_2^+, followed by an overview of the experimental achievements that have been made in the field. For a more extensive discussion, as well as a broader historical review of MHI in general, both experimental and theoretical, the reader is directed to [2].

2.1. From the atom to the molecule

In comparison to the hydrogen atom the additional proton in H_2^+ gives rise to additional degrees of freedom associated with nuclear motion. In a classical interpretation these degrees of freedom reveal themselves as oscillatory motion of the two nuclei: they can vibrate and rotate around their center of mass (see Fig. 2.1, left). From the perspective of quantum mechanics, this motion translates to additional sets of quantum states, which are described by two quantum numbers: v for vibration and N (or L) for rotation. As a consequence, the internal structure of H_2^+ is more complex than that of an atom. Each electronic state is comprised of numerous sub-levels, which are termed rovibrational and are distinguished by individual sets (ν, N).

The electronic ground state of H_2^+ is typically in the focus of consideration, since it is the only state with a deep potential minimum. The electronic wavefunction of this state is illustrated in Fig. 2.1, on the right. All other electronic states are either only very weakly bound, or not at all [32]. The total molecular energy in the electronic ground state and its internal rovibrational sub-levels is depicted in Fig. 2.2. Immediatly accessible with spectroscopy experiments are not the energy levels, but rather the transitions between them. For this reason, the subsequent discussion will focus on transition frequencies f, which are related to two energy levels $E_1 < E_2$ by the well-known equation $f = (E_2 - E_1)/h$, with Planck's constant h. Some transitions of interest are indicated within Fig. 2.2.

2.1.1. Simple models

Already during the early days of quantum mechanics, simple models of H_2^+ were considered. For instance, the rotational frequencies can be evaluated, using the model of the quantum mechanical rigid rotor, in which the two nuclei are fixed by an (imaginary) rod and rotate around a central axis that penetrates their center of mass. By solving this problem with the Schrödinger equation, one can obtain expressions for the quantized rotational frequencies [2]:

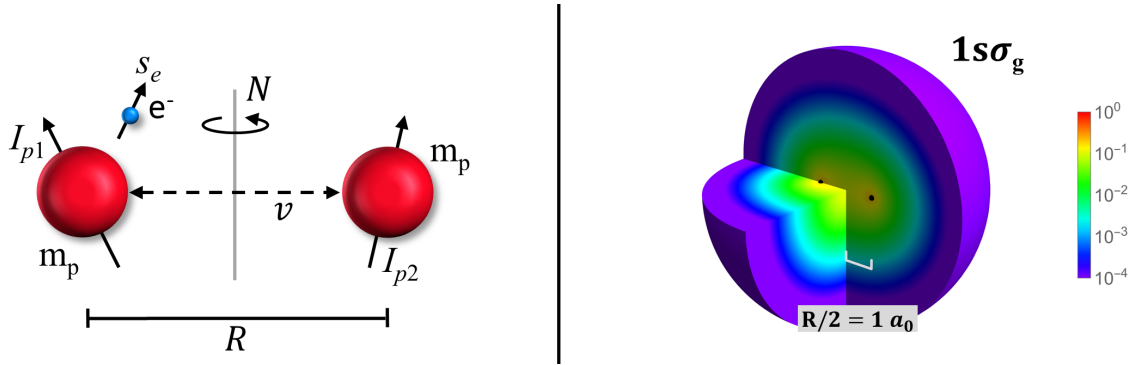$$f_{\text{rot}} \sim \frac{m_e}{\mu} c R_\infty \,. \tag{2.1}$$

Figure 2.1.: Basics of H_2^+. Left: Semi-classical depiction of H_2^+. The two protons with mass m_p, shown in red, are separated by a distance R. They may rotate around a central axis or vibrate around their center of mass. The electron (blue) is at some distance to the nuclei. The spins of the particles I_{p1}, I_{p2}, and s_e are indicated by corresponding arrows. **Right**: The electronic wavefunction of the electronic ground state ($1s\sigma_g$), shown as the probability density and obtained in the Born-Oppenheimer approximation (see text) for a fixed distance $R = 2a_0$. $R = 2a_0$ is the approximate mean separation of the nuclei in the electronic ground state, with a_0 being the Bohr radius.

With regard to the vibrational frequencies, a pedagogically useful model is provided by the Born-Oppenheimer approximation [34]. In this approximation, the entire molecule is described by a wavefunction, which is assumed to be the product of a nuclear and an electronic part. Similar to the rigid rotor, the distance between the nuclei R is fixed, thereby enabling the electronic wavefunction to be determined for "clamped" nuclei. The procedure is motivated by the assumption that the electronic motion is significantly faster than that of the nuclei. Consequently, the nuclear wavefunction is assumed to remain nearly constant during the motion of the electron. An expression for the wavefunction of H_2^+ as a function of R can be obtained in this model [35], allowing for a depiction as the one shown in Fig. 2.2. In the vicinity of the minimum, the potential is approximately harmonic. This reflects in the equation for vibrational frequencies, which resembles that of a quantum mechanical harmonic oscillator [2]:

$$f_{\text{vib}} \sim \sqrt{\frac{m_e}{\mu}} c R_\infty \, . \tag{2.2}$$

The dependence of the formulas 2.1 and 2.2 on the masses, i.e. the sensitivies of transition frequencies to these fundamental constants, is one primary reason for an interest in MHI studies, as it is stronger than in the case of the hydrogen atom. Consequently, if one desires to extract these constants from spectroscopic data, the experimental accuracy required to achieve a certain level of uncertainty for the constants is lower for MHIs.

However, the shortcomings of the models are apparent: For example, in contrast with the discussion of Chapter 1, there is no contribution from the nuclear charge radius. This is not surprising, given that the nuclear radius also enters as a reduced size effect in the hydrogen atom. It is therefore essential to develop a more complex model for the aims of MHI spectroscopy, in order to achieve the level of accuracy necessary for the research studies' goals.
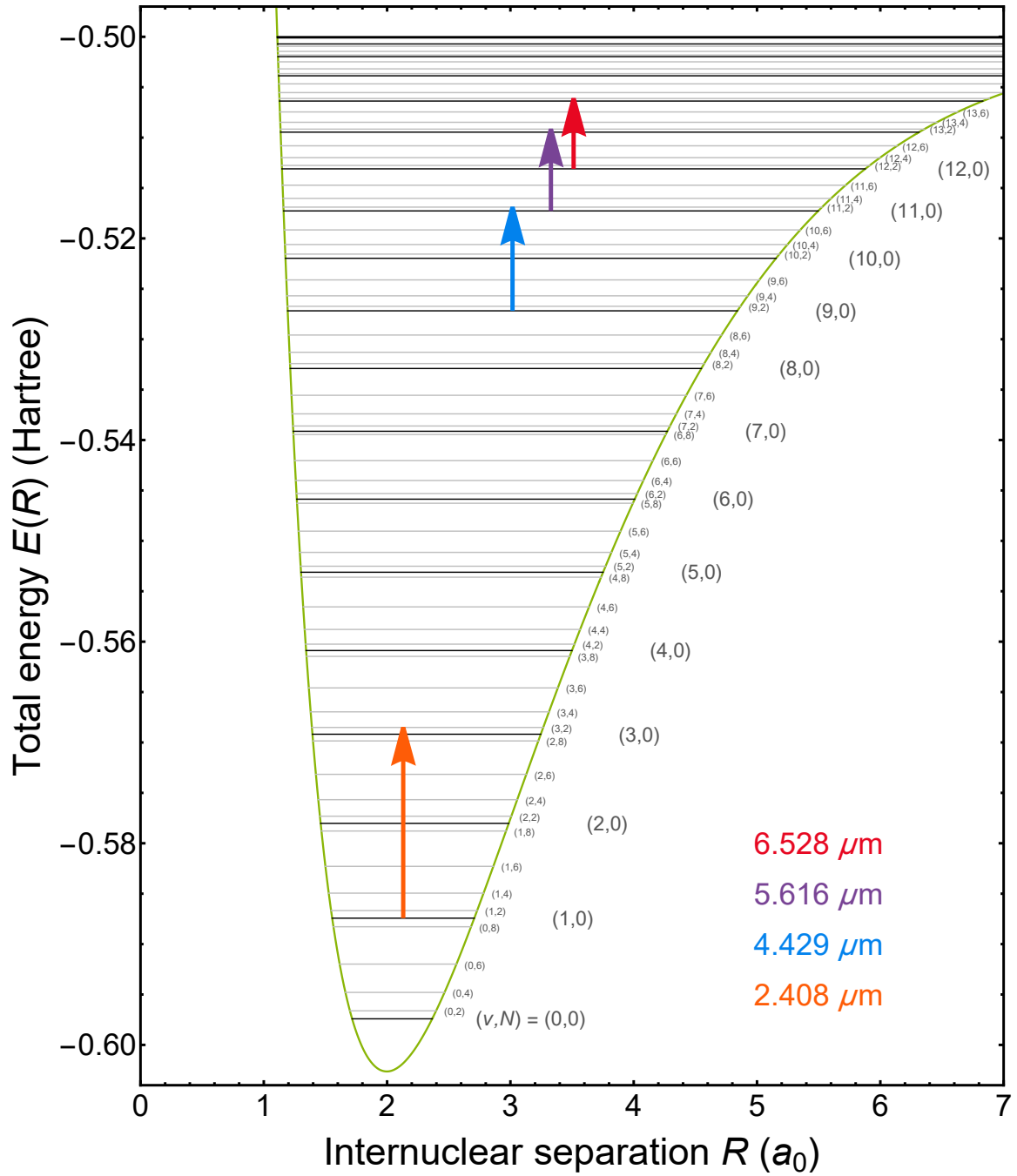
Figure 2.2.: Total molecular energy and rovibrational states of H_2^+. Shown in green is the total energy of the molecule as a function of the separation of the nuclei R for the ground electronic state, which can be obtained from the Born-Oppenheimer approximation (see Sec. 2.1.1). Within the energetic potential well, rovibrational bound states exist, displayed as gray lines. The states are labeled with their respective set of quantum numbers (v, N). For the sake of clarity, only states with zero or even N and a maximum $N_{max} = 8$ for $v < 7$ and $N_{max} = 6$ for $v \geq 7$ are shown; however, states with larger or odd N exist as well. For each vibrational quantum number, the ground rotational state is indicated by a larger label and in a darker color. Some transitions of interest, discussed in more detail in [7], are shown as colored arrows, with their respective wavelengths given in the lower right in corresponding color. The orange transition is of particular interest in the context of this thesis. The total energy as a function of R can be found e.g. in [32]. The transition wavelengths have been computed with the data provided in [33]. 1 Hartree $\simeq 27.2$ eV.

2.1.2. The spin-averaged frequency

A more complex model is realized with the spin-averaged transition frequency, which is computed within the framework of non-relativistic QED (NRQED; for an introduction see [36]). As the name suggests, this frequency is the expected theoretical value for a given transition when the internal angular momenta dependent structure (spin structure, Sec. 2.1.3) is disregarded. The accurate computation of this quantity is a complex topic that has been the subject of study for multiple decades. Most recently, predictions have reached relative uncertainties at a level of 8×10^{-12} [25]. This uncertainty results from two contributions: not (yet) computed terms in the QED expansion, and the uncertainties of fundamental constants, which serve as input data for the computation.

The largest zero-order contribution is the non-relativistic frequency. It is obtained by solving the three-body Schrödinger equation for the Coulomb interaction with so-called variational wavefunctions [37, 38]. The principle idea is to solve the equation with a sum of analytically relatively simple basis functions that have free ("variational") parameters. The specifics of the chosen ansatz and determination of these basis functions require both *a priori* and empirical knowledge, as well as substantial computational power. It is therefore unsurprising that highly accurate values for the non-relativistic energies could not be obtained until the advent of the modern age, when computing power became inexpensive and readily available. The current level of accuracy for the non-relativistic energy is significantly beyond the limits of what can be achieved with current experimental techniques.

However, it is widely acknowledged that the Schrödinger equation does not accurately describe quantum physics. Accordingly, corrections to this non-relativistic frequency of QED and relativistic nature must be computed [25, 39], distinguished in terms proportional to different powers of the fine-structure constant α. The challenge of computing these terms increases likewise with their order. The current limit of theoretical accuracy is partially attributable to the lack of computation of certain terms, which are instead only estimated in size and then treated as the theoretical uncertainty.

Recently, the Dirac-equation has been solved for this system [40, 41], providing an alternative approach to a zero-order term, which then already includes relativistic contributions.

An example of these individual contributions to the transition investigated in this thesis, namely $(v = 1, N = 0) \rightarrow (v' = 3, N' = 2)$ in H_2^+, is shown in Table 2.1.

2.1.3. Structure of a transition

The spins of elementary particles, in addition to the rotational angular momenta within the system, can interact in a multitude of ways. As a consequence, a minuscule substructure that depends on the specific values and orientations of the spins and angular momenta, exists for each quantum state. In the case of the hydrogen atom, this is a part of the cause for the well-known fine and hyperfine structure. For MHIs the complexity increases. In general, all three constituents possess a non-zero spin, and even in the electronic ground state, rotational angular momentum is present due to the rotation of the nuclei. Because of the numerous possible combinations of relative spin and angular momentum orientations, the result is a complex spin-structure, which must be considered alongside the spin-averaged frequency.

Table 2.1.: Contributions to the *ab initio* spin-averaged transition frequency of the transition $(v = 1, N = 0) \rightarrow (v' = 3, N' = 2)$ **in H**$_2^+$ (Methods Section 3 of Sec. 5.3, [42])**. The individual contributions are computed within the framework of NRQED. The last column lists the names of the main contributions to each order. For further details on these contributions, see e.g. [25, 39]. The final prediction for the value of spin-averaged transition frequency, $f_{\text{spin-avg}}^{(\text{theor})}$, is given in the bottom row. In the computation, the CODATA22 set of fundamental constants was used.

Term	Relative order	Contribution (kHz)		Origin
$f^{(0)}$	1	124 485 554 550.71		Non-relativistic three-body Schrödinger solution
$f^{(2)}$	α^2	2 002 698.73		Relativistic corrections in Breit-Pauli approximation; nuclear radii
$f^{(3)}$	α^3	−521 345.53		Leading-order one-loop radiative corrections
$f^{(4)}$	α^4	−3 689.05		One- and two-loop radiative corrections; relativistic corrections
$f^{(5)}$	α^5	228.67		Up to three-loop radiative corrections; Wichmann-Kroll contribution
$f^{(6)}$	α^6	−1.62		One- and two-loop radiative diagrams; Wichmann-Kroll contribution
f^{other}		0.54		Muon and hadron vacuum polarization
$u\left(f_{\text{spin-avg}}^{(\text{theor})}\right)$			1.32	Combined uncertainty stemming from QED theory and fundamental constants
$\mathbf{f_{spin\text{-}avg}^{(theor)}}$		**124 487 032 442.5**	**(1.3)**	**Total transition frequency**

In detail, the three particle spins s_1, s_2 and s_3 couple with the rotational angular momentum N via the formulas

$$G_1 = s_1 + s_2, \qquad G_2 = G_1 + s_3, \qquad F = G_2 + N .$$

The particle spins and first two coupled momenta are here denoted in a general way, since the coupling schemes chosen in the literature for various MHIs are not always of the same type. The total angular momentum F, which is independent of the chosen coupling scheme, is the most important property, as it defines the physically measurable states. To give an example, the left side of Fig. 2.3 illustrates the coupling scheme for a specific state of HD$^+$.

The general form of the spin Hamiltonian, which describes all interactions between the angular momenta, contains numerous terms and corresponding coefficients. For examples, see [2, 43]. The coefficients can be computed with high accuracy, most recently with a relative uncertainty at the level $\sim 10^{-6}$ [31, 44]. In many cases, the resulting manifold of sub-states is disadvantageous from an experimental standpoint, as it results in an exponential increase in spin transitions between two given rovibrational states. As previously discussed (Sec. 1.3), determining the full spin structure and obtaining the spin-averaged frequency solely through measurements is challenging with the current experimental techniques.
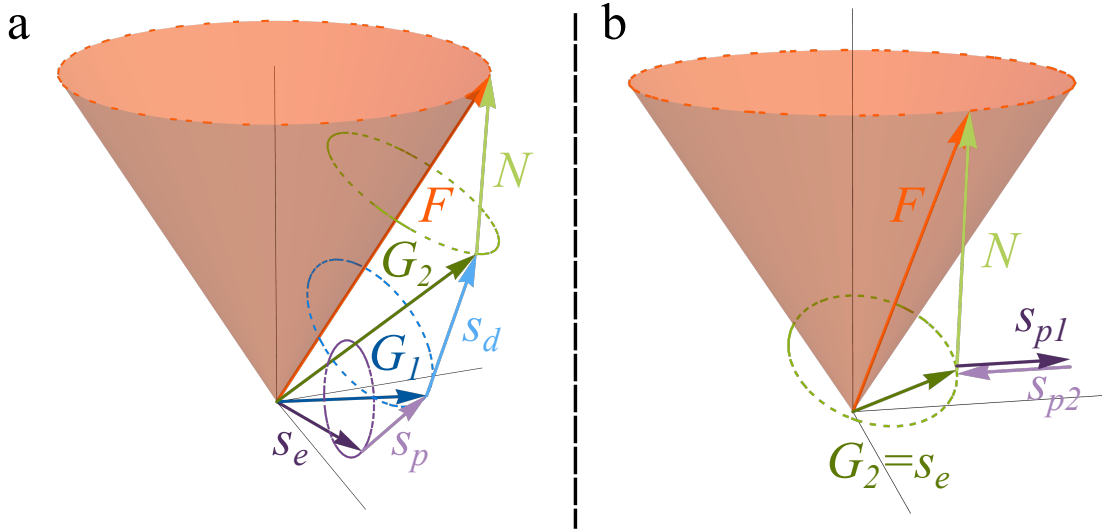
Figure 2.3.: Some angular momenta coupling schemes for MHIs. Left: Coupling scheme for HD$^+$ shown as an example for the state $(v, N, G_1, G_2, F) = (v, 1, 1, 2, 3)$. The electron spin $s_e = 1/2$ and proton spin $s_p = 1/2$ couple to $G_1 = 1$, which then couples with the deuteron's spin $s_d = 1$ to $G_2 = 2$. A final coupling step with the rotational angular momentum $N = 1$ results in the total angular momentum $F = 3$, which is precessing around the z-axis. The orange cone illustrates the precession for an angular momentum projection $m_F = 3$. **Right**: The coupling scheme for para-H$_2^+$ and $N = 2$. Due to the anti-permutation symmetry of the nuclei (see text), the two proton spins do not contribute to the coupling, which is illustrated by the two anti-parallel purple arrows. As a result, only coupling between s_e and N is possible, resulting in $F = G_2 + N = s_e + N = 5/2$. The precession (orange cone) is shown for $m_F = 5/2$.

However, there are a few special cases, in which the spin structure simplifies. One such case is para-H$_2^+$, for which the total nuclear spin $I = s_{p1} + s_{p2}$ is zero. This is a consequence of the anti-permutation symmetry that must hold for the total nuclear wave function, since the protons are fermions. Given that the spatial component of the wave function is symmetric for $N = 0$ or $N = even$ levels, the spin component must be anti-symmetric, resulting in a zero total spin. The only remaining spins and angular momenta that may interact to split the levels are the electron's spin s_e and the angular momentum of the nuclei N (the electron's angular momentum is zero, since only the electronic ground state is considered). The result is a spin-structure comprising of only a single state for $N = 0$ and two sub-states for N being an even number. The total angular momentum of the state is then simply given by $F = s_e$ for $N = 0$ or $F = N \pm s_e$ for $N > 0$, see right side of Fig. 2.3 for an illustration of the latter. In this situation, the spin Hamiltonian of a state reduces to a simple expression,

$$H_{\mathrm{spin}} = c_e \left(s_e \cdot N \right) , \tag{2.3}$$

since all other terms vanish. For example, consider a transition from $N = 0$ to $N' = 2$ between any vibrational quanta v, v' as shown in Fig. 2.4. In order to measure the complete internal structure, only two components need to be measured: $(F = s_e \rightarrow F' = N \pm s_e)$. From the difference of these two transition frequencies, the coefficient c_e of the upper level can be determined immediately, while the spin-averaged frequency can be easily obtained by their weighted sum (see Sec. 5.2).

It should be noted that the spin structure of ortho-H_2^+ (uneven N) is more complex (see e.g. [2, 30]), since $I \neq 0$ in this case.

Importantly, the total angular momentum F also defines the number of Zeeman sub-levels present in a given spin state. Each of these states will be split into $2F + 1$ states with quantum number $m_F = -F, ..., +F$. As is well-established, in the presence of a non-zero magnetic field, the Zeeman effect gives rise to a splitting of these previously degenerate states, thereby further complicating the situation. Given that a magnetic field is essential for the experiment (for instance, to provide a clearly defined quantization axis for the polarization) the effect cannot be disregarded. Fortunately, the Zeeman shift is well understood, and theoretical calculations [30, 45] can serve to predict the splittings if the magnetic field value is known with sufficient precision.

In this thesis, advantage will be taken of the simplicity of para-H_2^+ by investigating a transition of the type $N \rightarrow N' : 0 \rightarrow 2$. It is therefore of interest to discuss the coefficient c_e in more detail. Physically, it is the coupling constant between the measurable energy splittings and the interaction of the electron spin with the nuclear rotational angular momentum. It is computed within the framework of perturbation theory, similar to the spin-averaged frequency. The coefficient was initially addressed in theoretical works from the 1960s [46], with subsequent improvements in calculations over the years [47, 48, 49]. However, for an extended period, the theory was unable to find a good match with the limited experimental data available, most importantly a set of hyperfine transitions observed by Jefferts in 1969 [50]. A part of the challenge was related to the fact that the measurements predominantly comprised of transitions of ortho-H_2^+ and as a consequence more spin-spin and spin-rotation interactions had to be considered. It was assumed that the issue could be resolved by computing higher-order terms not yet considered in the calculation [48, 49]. Following a reconsideration of the effective spin Hamiltonian in the form of the Breit-Pauli Hamiltonian [43], a satisfactory match was found for the majority of transitions observed by Jefferts, although not for all of them. It took another decade, and in total half a century after the transitions were measured, for theorists to be able to explain all experimental data with a competitive level of uncertainty [51, 44]. The result is a highly accurate and experimentally verified theoretical framework for the spin interactions of H_2^+. In contrast and as previously mentioned, there has been some tension between recent observations of spin splittings and their predictions for HD^+. Therefore, a further experimental investigation, also for H_2^+, is desirable.

2.1.4. Transitions in MHI

In principle, the frequency of a transition between any two states of a MHI can be calculated. However, it does not yet include the relevant information whether or not that transition is actually physical, i.e. if the transition can take place under any type of physical interaction. This must be analyzed by computing the value of the interaction operator A between the wavefunction of initial ψ_{initial} and final ψ_{final} states, i.e.

$$\langle \psi_{\text{initial}} | A | \psi_{\text{final}} \rangle . \tag{2.4}$$

This quantity is termed transition moment and only if it is non-zero, the transition is physically possible under the interaction A and therefore of interest to spectroscopy. Two important properties can be derived from the transition moment. For one, its magnitude determines the
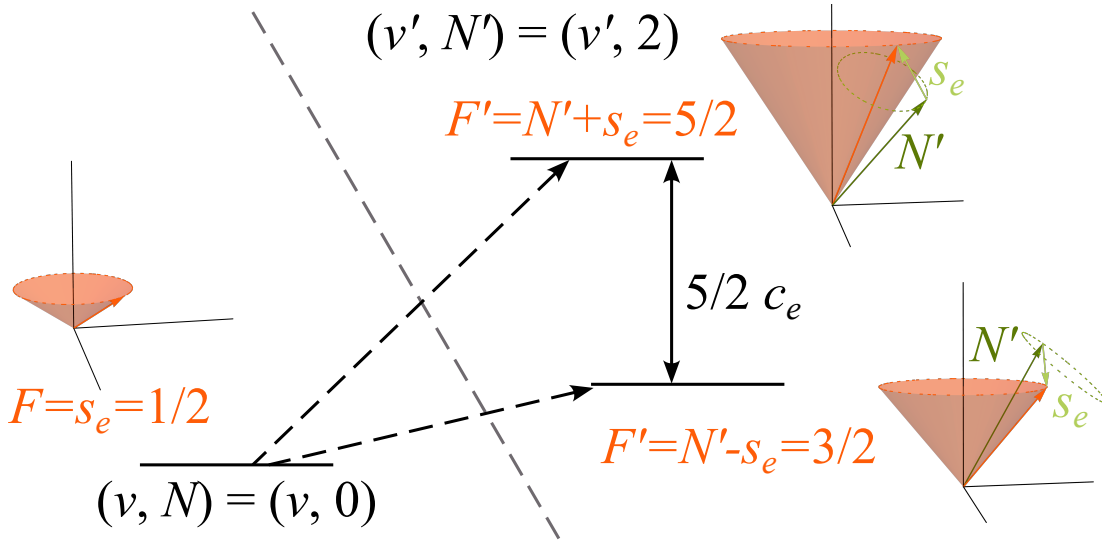
Figure 2.4.: Schematic representation of the hyperfine structure of para-H_2^+ for a transition of the type $N \to N' : 0 \to 2$. The angular momentum coupling scheme is shown for each hyperfine sub-state. In the arbitrarily chosen energetically lower state $(v, N = 0)$, the only angular momentum is the electron's spin s_e and thus no sub-structure exists. In the upper state $(v, N' = 2)$, s_e couples with the rotational angular momentum N. Two coupling variants are possible, resulting in two hyperfine sub-states, which are split due to the spin-rotation interaction $(s_e \cdot N')$ and weighted by the constant c_e. The depictions of the coupling of the angular momenta in the form similar to Fig. 2.3 are chosen for the maximum angular momentum projection quantum number $m_F = F$. Other projections $m_F \in \{-F, ..., F - 1\}$ are also possible. In the presence of an external magnetic field, these states would be further split due to the Zeeman effect, a depiction of which will follow later (Sec. 4.2.3).

strength of the transition. From an experimental point of view, this property is significant as it defines the relationship between the driving fields and the excitation probability per unit time. Secondly, there are specific combinations of quantum numbers of the initial and final states for which the transition moment vanishes and therefore the transition is "forbidden". From this principle, the so-called selection rules can be derived, which are rules that define a relation between the transition's initial and final quantum numbers.

In this context, an important property of H_2^+ is the symmetry of center-of-mass and center-of-charge of its nuclei. Essentially, this symmetry results in the permanent dipole moment of the nuclei becoming null, thereby causing electric-dipole (E1) transitions between rovibrational levels in the electronic ground state of H_2^+ to be forbidden. In terms of the property 2.4, this follows immediately from the fact, that the electric dipole operator sandwiched between the two states vanishes, and therefore any combination of states will have a transition moment equal to zero. The functional absence of E1 transitions in H_2^+ poses a major challenge for experimentalists, as these transitions are typically the strongest type and as such are the easiest to interrogate. It is therefore unsurprising that recent experiments have focused on HD^+, given that in this isotopologue the asymmetry of the masses of proton and deuteron causes the nuclei's center-of-mass to shift, resulting in a non-zero dipole moment and allowing E1 transitions. For H_2^+, however, an alternative has to be sought.

With the next higher-order electric interaction, electric-quadrupole (E2) transitions are intro-

duced. These transitions are allowed in H_2^+, but are orders of magnitude weaker in comparison to the dipole variant in HD^+, as a consequence of the considerably smaller transition moments. The first theoretical consideration of electric quadrupole transitions in H_2^+ was conducted by Bates and Poots [52], with subsequent, increasingly precise works published over the years [53, 54]. A complete treatment that encompasses both the hyperfine structure and the influence of the electric field polarization has been presented by Korobov et al. [55]. Regarding the selection rules for the quantum numbers v and N, these have been derived from the quadrupole transition moments [55]. The result is that no selection rule exists for v (although the transition moment has a strong dependence on v, see below). In contrast, selection rules do exist for N of the following form: $N' = N$, $N \pm 2$ for $N > 0$, and $N' = N + 2$ for $N = 0$. Therefore, the type of transition $N \to N' : 0 \to 2$ with a simple hyperfine structure, discussed in the previous section 2.1.3, is allowed.

An alternative option to investigate are magnetic dipole transitions (M1) [56]. However, these are predicted to be orders of magnitude weaker than E2 transitions and are thus not as attractive to pursue. It should additionally be noted, that very weak E1 transitions are predicted in H_2^+ due to spurious spin interactions [57]. Similar to M1 transitions, their strength is far below that of E2 transitions.

In order to compensate for the inherent weakness of E2 transitions, it is necessary to employ higher field strengths of the driving electric field, a laser. A calculation of the rates of E2 transitions is thus of interest in order to estimate the necessary parameters for the experiment. In the following, estimates will be presented based on the quadrupole transition moments computed in [55], to motivate the requirements for the spectroscopy laser system developed in this work (Sec. 5.1). Typically, published values are given in the form of Einstein A coefficients, which are properties related to the transition moment eq. 2.4. A straightforward and approximate form of the relationship between these properties and the laser parameters can be obtained as follows:

The probability per unit time $\mathcal{P}_{fi}$ to excite a transition between a final state f and an initial state i is proportional to the transition's squared Rabi-frequency Ω_{fi} [58]

$$\mathcal{P}_{fi} \propto |\Omega_{fi}|^2 \; . \tag{2.5}$$

The Rabi-frequency can be expressed in terms of the transition's Einstein A_{fi} coefficient and angular frequency ω_{fi}, in combination with the electric field strength E [59]

$$\Omega_{fi} = \frac{ec}{\hbar\sqrt{\alpha}} \, |E| \sqrt{\frac{A_{fi}}{\omega_{fi}^3}} \sigma \; . \tag{2.6}$$

Here, e, $\hbar$, c and α are the elementary charge, the reduced Planck constant, the speed of light, and the fine-structure constant, respectively. The quantity σ is a dimensionless factor of $\mathcal{O}(1)$ that includes hyperfine and electric field polarization dependent contributions. A simplified case will be considered, neglecting the hyperfine structure of a transition, and assuming a linear polarization of the spectroscopy wave. In this case, $\sigma \approx 1$. Substituting eq. 2.6 into 2.5 and considering the relation between electric field and intensity ($I = (\epsilon_0 c/2) |E|^2$), the rate $\mathcal{P}_{fi}$ can then be expressed as

$$\mathcal{P}_{fi} \propto \frac{2e^2 cI}{\hbar^2 \alpha \epsilon_0} \frac{A_{fi}}{\omega_{fi}^3} \; . \tag{2.7}$$

MHI	$(v, N) \rightarrow (v', N')$	A_{fi} (s^{-1})	$\omega_{fi}/(2\pi)$ (s^{-1})
	$(0,0) \rightarrow (1,2)$	0.160207×10^{-6}	70.6×10^{12}
H_2^+	$(1,0) \rightarrow (3,2)$	0.784599×10^{-7}	124.5×10^{12}
	$(0,0) \rightarrow (3,2)$	0.497870×10^{-8}	190.2×10^{12}
HD$^+$	$(0,0) \rightarrow (5,1)$	0.015	259.8×10^{12}

Table 2.2.: Values for the Einstein coefficients A_{fi} and frequencies ω_{fi} of selected MHI transitions. Data for H_2^+ are taken from [55]. A_{fi} for HD$^+$ is computed by inserting the value of the oscillator strength of the transition, as found in [61], into eq. (2) of [62], while ω_{fi} can be found, for example, in [12].

The aim of this discussion is to estimate the required laser power necessary within the present apparatus to sufficiently excite an E2 transition. Accordingly, a target value for $\mathcal{P}_{fi}$ can be provided by previous experiments conducted in the same apparatus on HD$^+$. For example, the transition HD$^+$: $(0,0) \rightarrow (5,1)$ [12] has been measured under a nominal power of $P^{(\mathrm{E1,HD}^+)} \approx 0.6\,\mathrm{mW}$ [60]. If the same excitation rate for an E2 transition is required, the necessary E2-power can be computed as

$$\mathcal{P}_{fi}^{(\mathrm{E2},H_2^+)} = \mathcal{P}_{fi}^{(\mathrm{E1,HD}^+)}$$

$$\overset{\text{eq. 2.7}}{\Longleftrightarrow} \qquad \left(I\frac{A_{fi}}{\omega_{fi}^3}\right)^{(\mathrm{E1,HD}^+)} = \left(I\frac{A_{fi}}{\omega_{fi}^3}\right)^{(\mathrm{E1,HD}^+)}$$

$$\Rightarrow \qquad P^{(\mathrm{E2},H_2^+)} = \left(P\frac{A_{fi}}{\omega_{fi}^3}\right)^{(\mathrm{E1,HD}^+)} \left(\frac{\omega_{fi}^3}{A_{fi}}\right)^{(\mathrm{E2},H_2^+)}. \qquad (2.8)$$

In order to obtain the bottom expression, it was additionally assumed that the E1 and E2 spectroscopy waves are similarly focused, such that $I^{(\mathrm{E2},H_2^+)}/I^{(\mathrm{E1,HD}^+)} = P^{(\mathrm{E2},H_2^+)}/P^{(\mathrm{E1,HD}^+)}$. Values for the Einstein coefficients $A_{fi}^{(\mathrm{E2},H_2^+)}$ and frequencies $\omega_{fi}^{(\mathrm{E2},H_2^+)}$ of selected E2 transitions in H_2^+, as well as the transition $(0,0) \rightarrow (5,1)$ in HD$^+$, can be found in Tab. 2.2. Data for a wide range of E2 transitions in H_2^+ are found in [55].

It is important to note that eq. 2.8 is valid only in the case that the exposure times to each laser wave are (approximately) equal. Therefore, the resulting power level $P^{(\mathrm{E2},H_2^+)}$ should be understood as the necessary power level only in the case that other experimental parameters remain unchanged. In practice, this was not the case, which can however be motivated by the results discussed here. As will be seen, the necessary value $P^{(\mathrm{E2},H_2^+)}$ computed for the transition of interest in the context of this work, $(1,0) \rightarrow (3,2)$ in H_2^+, is roughly 10 times larger than the available power from the spectroscopy laser system (see Sec. 5.1). To compensate for this, the exposure time to the E2 wave was chosen to be longer than that of the E1 wave by a similar factor.

Figure 2.5 shows $P^{(\mathrm{E2},H_2^+)}$ computed according to eq. 2.8, for a range of transitions. It is evident that smaller values of Δv are more favorable, since the power level increases strongly with Δv.

Specifically highlighted in Fig. 2.5 as a red point is the transition $(1,0) \rightarrow (3,2)$ with a required power of $P^{(\mathrm{E2},H_2^+)} = 12.8\,\mathrm{W}$, which is chosen as an interrogation target for this thesis. This choice is generally not straightforward, given the vast number of potential candidates. However, a few key considerations significantly reduce the number of attractive transitions. Firstly,
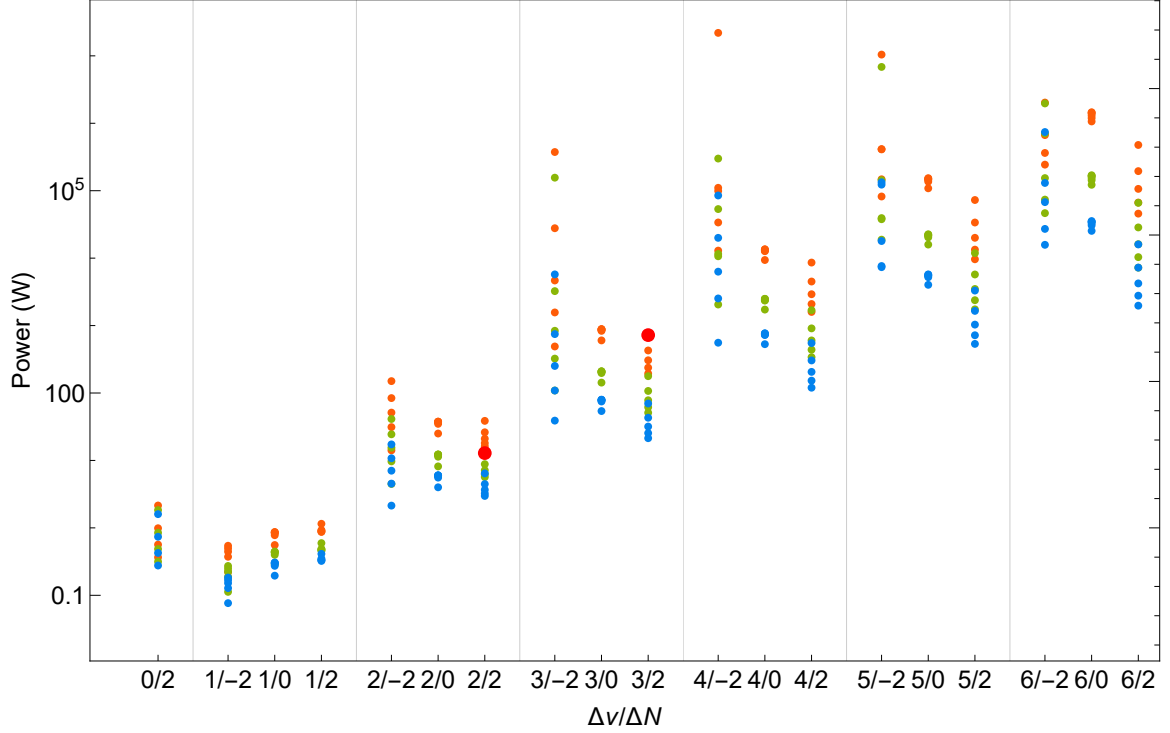
Figure 2.5.: The estimated necessary laser powers $P^{(\mathbf{E2}, \mathbf{H_2^+})}$ for various E2 transitions $(v, N) \to (v', N')$ **in $\mathbf{H_2^+}$**, computed according to eq. 2.8. The three colors correspond to different ground vibrational levels of the transition: $v = 0, 1, 2$ is shown in orange, green, blue, respectively. For these three cases, all transitions for which data is provided in Ref. [55] are displayed. The data are sorted according to Δv and ΔN of the transition. The red data points highlight two transitions: $(1, 0) \to (3, 2)$, which has been studied in this work, and $(0, 0) \to (3, 2)$, which has been proposed as an interrogation target [63].

there is the discussion of this section, i.e. that the necessary power level should be realizable experimentally. Restricting the discussion to this argument, transitions of the type $\Delta v = 1$ are the first choice, given that they necessitate the lowest required power level. Expanding the discussion, a second, simple argument is that the pursuit of the highest relative accuracy is most readily accomplished by a transition of the highest frequency. It is therefore desirable to maximize the frequency of the interrogated transition. Thirdly, the spectroscopy laser system must be referenced and stabilized by some means, and in this context the majority of effort has been directed towards wavelengths in the near-infrared regime. In light of all of these considerations, transitions of the type $\Delta v = 2$ represent a compromise: their required power level remains within the capabilities of current commercial laser systems, while their transition wavelengths ($\sim 2 - 3 \, \mu$m) fall close to the NIR range. In principle, any transition of the type $\Delta v = 2$ can be similarly considered. The specific choice of transition in this work is motivated by other factors, both experimental and theoretical (e.g. the simple HFS already outlined in Sec. 2.1.3), and will be further discussed in Sec. 4.2.3.

Similarly, the transition $(0, 0) \to (3, 2)$ has been proposed as an interrogation target [63]. The required power level is 721 W (see Fig. 2.5). This exceptionally high level is a daunting task, especially considering the necessary frequency stability for a spectroscopic application. However, the transition has been proposed in the context of single particle traps, in which the regional constraint of the ion is much smaller than that in the cluster trap underlying this work

(see Sec. 4.1.1). Therefore, a much tighter focusing of the spectroscopy wave should be feasible, thereby reducing the necessary power level to achieve the desired intensity. If the radius of the spectroscopy laser at the ion's position is reduced by the reasonable factor 10^2, the transition's required power reduces to $0.7\,\text{W}$ at a wavelength of $1.58\,\mu\text{m}$. At this wavelength such a power level is widely available. An approach towards providing this radiation at a level suitable for spectroscopic applications using the laser system utilized in this work is discussed in Sec. 5.1.

Note, that for a more precise calculation, the transition rates must be multiplied by a hyperfine and polarizability dependent factor (see $\mathcal{W}^{\text{hfs}}$ and $\mathcal{W}^{\text{pol}}$ in [55]), both of which are smaller than one. Accordingly, the values presented here should be regarded as an upper bound for the actual excitation rate of a single Zeeman component of a transition. As a consequence, a higher intensity than the one estimated here is desirable for the experiment.

2.2. Historical overview

In light of the highly advanced theory, it is imperative that experiments are conducted with equal accuracy as a means of achieving the aims of the physics studies discussed in Sec. 1. However, these types of experiments have been scarce, in part due to the difficulty of investigating E2 transitions, which require, for example, a highly advanced laser system as discussed in the previous section.

A limited number of studies have been conducted on the spin structure of the molecule, next to a few measurements of its rovibrational intervals. An overview of these measurements is provided in Figure 2.6. A distinction is made between direct and indirect measurements. Direct measurements are those where the interrogation subject was always H$_2^+$, irrespective of the technique employed. Indirect measurements have been done mostly on Rydberg states of neutral H$_2$, from which energy intervals of H$_2^+$ have been inferred. This method has proven more fruitful in the past, since experiments with ions have historically presented a greater challenge for a number of reasons, including the necessity of a more complex apparatus and the smaller number of available particles.

With regard to the spin structure, one noteworthy study is that of Jefferts in 1969 [50], in which relative inaccuracies of transition frequencies of up to 1.2×10^{-6} were achieved. This study is of significant interest as it permits a full description of the internal structure of the interrogated transitions, thereby facilitating a comparison with theory, where agreement is found [64]. Further improvements in accuracy were achieved by Menasian and Dehmelt in 1973 [65], with accuracies at a relative level of 1.3×10^{-7}, also in agreement with theory [44]. No improvements in measurements of the spin structure have been achieved since. There have been indirect measurements based on Rydberg spectroscopy of H$_2$, as well as one further study on H$_2^+$ [66], but these have not been able to improve the achieved accuracy. A very recent work using quantum-logic spectroscopy of a single H$_2^+$ shows a promising resolution at a level of 1×10^{-9} [67], but has yet to demonstrate a characterization of systematic effects in order to enable a comparison with theory.

Greater attention has been devoted to rotational and rovibrational intervals of H$_2^+$, with a number of direct and indirect measurements being conducted over the last five decades. The highest relative accuracy achieved up until recently was 2.8×10^{-7}, as reported by Arcuni et al. [68]. This record has remained unchallenged for over three decades, and has been surpassed by the first result presented in this thesis (Schenkel et al. in Fig. 2.6, more details in Sec. 5.2).
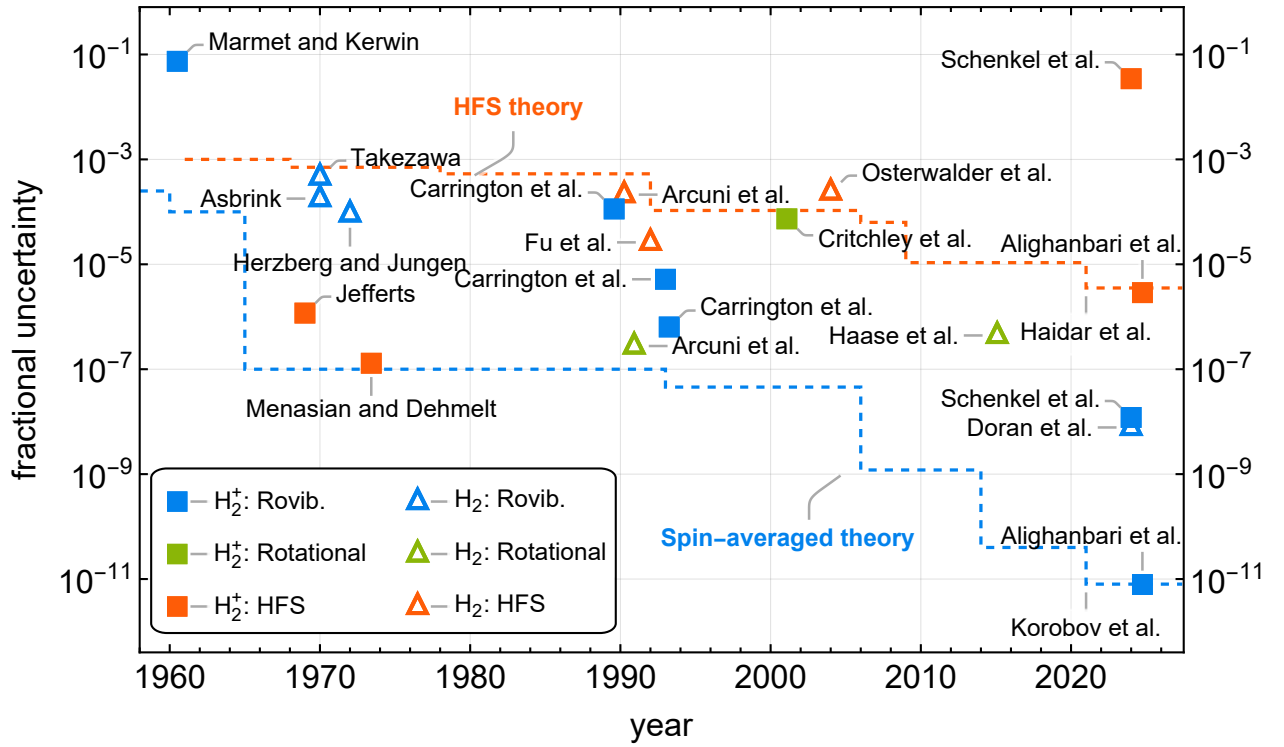
Figure 2.6.: Historical overview of some H_2^+ studies. The color of the data point serves to indicate the property that was measured. The color blue represents vibrational or rovibrational energy intervals, green indicates rotational energy intervals, and orange denotes spin structure measurements. The shape of the data point indicates the type of measurement, where a square represents a measurement done directly on H_2^+, while a triangle denotes measurements done on Rydberg states of H_2. The progress of theoretical calculations is shown as dashed lines. The results presented in this thesis are labeled as "Schenkel et al." (Sec. 5.2) and "Alighanbari et al." (Sec. 5.3). For a list of references of the shown works, see Sec. A.

A study based on H_2-Rydberg spectroscopy, contemporary to this thesis, measured the ground vibrational interval of H_2^+ with an improved relative accuracy of 7.8×10^{-9} ([69], Doran et al. in Fig. 2.6). Yet none of these measurements have reached an uncertainty competitive with theory, which has left the aims of MHI studies unattainable.

Finally, as part of this thesis, our group has achieved the next leap, by determining a rovibrational energy interval with a relative inaccuracy of 7.9×10^{-12} and measuring the transition's spin structure (Alighanbari et al. in Fig. 2.6, more details in Sec. 5.3). The work represents the first time, that an experimental determination of a rovibrational transition frequency in H_2^+ has achieved a level of accuracy competitive with theory.

3. Aims of this work

With the primary objectives of MHI research studies laid out in Chapter 1, the necessity for highly accurate spectroscopy of H_2^+ becomes apparent. However, as outlined in the historical overview in Sec. 2.2, prior experiments have not met the expectations set forth by the theory. Thus, the main goal of this thesis was the spectroscopic investigation of a rovibrational transition in H_2^+, with the aim of improving the experimental accuracy to a level which approaches that of theory.

In order to accomplish this goal, it was necessary to design, set up, characterize, and implement a suitable spectroscopy-grade laser system. The system must provide high frequency stability and accuracy, as well as sufficient power to drive E2 transitions in H_2^+ (see Sec. 2.1.4). Furthermore, it is essential that the laser's frequency is traceable to the International System of Units (SI) to ensure comparability with CODATA.

Additionally, the experimental procedures developed by our group for HD^+ must be adapted or replaced when transitioning to H_2^+. This is particularly relevant with regard to the quantum state preparation of the interrogated species, which is tailored towards HD^+ and cannot readily be transferred to H_2^+.

The experimental setup and details of the procedures will be presented in Sec. 4.1 and 4.2, respectively. The developed spectroscopic laser system will be summarized in Sec. 4.1.2, with additional details provided in Sec. 5.1. Following its development and characterization, the spectroscopy laser system was then utilized together with the trapping apparatus to investigate a rovibrational transition in H_2^+. The specifics of the chosen transition are detailed in Sec. 4.2.3. The work was conducted in two subsequent studies.

First, the conditions under which the interrogation yielded discernible signals were identified by measuring a Doppler-broadened rovibrational transition. This represents the first instance of driving and detecting such a transition in H_2^+ using lasers. The measurement was conducted in combination with a study of the systematic effects of an analogous transition in HD^+. Here we demonstrated that a detailed systematic investigation of an E2 transition in molecular ions is achievable at the level of accuracy desired for the research aims. The choice to demonstrate this in HD^+ was made in order to make use of the well-tested procedures that have been developed for this isotopologue. The study is presented in Sec. 5.2.

Second, under a modification of the spectroscopy procedure, the accuracy of the determined transition frequency in H_2^+ was increased by three orders of magnitude compared to the first study. This was achieved by resolving single Doppler-free Zeeman components of the transition, including a study of their systematic effects. The determined transition frequency represents the most accurate measured property of H_2^+ to date. In Sec. 5.3 the results of the spectroscopic study are presented. They allow for a state-of-the-art determination of the proton-electron mass ratio, thereby achieving one of the primary objectives of MHI studies. Other evaluations of the type discussed in Sec. 1.2 are also demonstrated. A summary of the results is provided in Chapter 6.

4. Spectroscopy of molecular hydrogen ions

4.1. Experimental setup

In order to interrogate MHIs, it is necessary to prepare a controlled environment in which to detect, store, and manipulate the particles. For this purpose, trapping techniques have been envisioned for multiple decades, with some regarded significant enough to award their development and realization with the Nobel prize in physics [70, 71].

Among these techniques, specifically the ones designed for ionized matter are of interest with regards to MHIs. The main candidates in this subcategory are the linear RF trap (also known as the Paul trap) and the Penning trap. The latter requires a strong magnet due to its reliance on a large magnetic field to contain the particles along one Cartesian direction. Today, such magnets are realized by the use of superconductors, which necessitates a considerable amount of experimental effort and a continuous supply of liquid nitrogen for realizing the required temperatures. For these reasons, the linear RF trap is arguably a more simple method.

It is therefore unsurprising that the first experiments achieving the controlled preparation of MHIs have been performed on such traps [72, 73]. In order to simultaneously cool and detect the trapped MHIs, Doppler-cooled beryllium ions were co-trapped. Although initially challenging, the technique has now been adopted by multiple groups for regularly preparing ensembles of cold MHIs [12, 24, 74, 75] or even single MHI [76, 77]. Recently, also the first experiments on a single MHI confined in a Penning trap have been reported [78].

4.1.1. The ion trap apparatus

The apparatus used in this work is the same one used in recent experiments performed on HD$^+$ [21, 12, 23]. The specifics of the design of its linear RF trap and other components have been previously developed and described in detail [79, 80, 81, 82].

The trap is employed for the loading of clusters comprising a few thousand beryllium ions, which can be Doppler-cooled using a laser with a wavelength of 313 nm. The thereby scattered photons are partially collected by a specially designed imaging system and serve as the signal for almost all applications. The apparatus is capable of achieving temperatures of a few millikelvin, as determined through spectroscopic linewidth measurements. In these conditions, the confined ions will form crystalline structures, known as Coulomb crystals. Once the beryllium crystal has been prepared via electron impact ionization and subsequent Doppler-cooling, MHIs can be loaded into the trap. This is achieved by leaking a small quantity of neutral gas of the desired isotopologue into the vacuum chamber, which is subsequently ionized by electron impact. The

ionized version of the molecule can then be confined by the RF field of the trap and cooled through Coulomb interaction with the beryllium ions, a process known as sympathetic cooling.

After this procedure, the external degrees of freedom of the MHIs are adequately prepared. Nevertheless, residual Doppler-broadening exists, with a magnitude of a few megahertz in the case of MHIs contingent upon the transition frequency and the mass of the isotopologue. Furthermore, and of significant importance for spectroscopy, the internal degree of freedom (the quantum state of the molecule) has yet to be considered. Both of these issues are addressed through the implementation of appropriate techniques. The methods used for preparing the internal state and surpass the Doppler-broadening will be discussed in Sec. 4.2.1 and 4.2.2, respectively.

An important property of particles confined within the linear RF trap, which is leveraged for the spectroscopy, is their secular motion. It can be shown analytically that a particle in the trap exhibits a specific resonance frequency, which is contingent on its charge-to-mass ratio [71]. Assuming singly charged particles, this secular frequency $\omega_{\mathrm{sec}}(m)$ is simply a function of the mass m of the particle and can be employed to determine the type of particle present in the trap. This is achieved by applying a voltage with a frequency ω, which will excite the classical motion of the confined ions if ω is close to $\omega_{\mathrm{sec}}(m)$. As a consequence of the Coulomb interaction between all trapped particles, such an excitation will, to a certain extend, be transferred to the beryllium ions. Since the fluorescence of the beryllium ions is dependent on their temperature, the excitation will be visible in the fluorescence signal. The signal strength is hereby related to the amount of trapped ions with mass m. In summary, by varying ω and observing the resonances in the correlated fluorescence signal, the confined amount of particles of any mass can be determined. An example of the fluorescence trace when applying a voltage with a scanning frequency ω is provided in Sec. 4.2.2, Fig. 4.3.

4.1.2. Spectroscopy laser system

4.1.2.1. Setup

One of the main challenges of this work was the development of a laser system capable of driving E2 transitions in H_2^+. As stated before, the system should provide: (1) sufficient power to excite a rovibrational E2 transition of an MHI, (2) a high degree of frequency stability, and (3) a highly accurate measurement of its frequency, which is linked to the SI-standard. An additional desirable feature would be the ability to tune the wavelength while maintaining the former three requirements, thereby allowing for a certain degree of flexibility regarding the target transition.

The demonstrated solution to provide all of these aspects simultaneously is a continuous-wave (CW) optical-parametric oscillator (OPO), which is stabilized and measured through an optical frequency comb (OFC). CW OPOs are capable of providing high output power at the watt level over their signal and idler ranges, which are two radiations down-converted from the so-called pump by three-wave mixing in a nonlinear optical material. For details, see e.g. [83]. The relationship between the three is expressed by the simple equation $\omega_p = \omega_s + \omega_i$, where ω_p, ω_s and ω_i are the pump, signal, and idler frequencies, respectively.

In this work, the idler radiation is of main concern, as it is typically the one with the proper frequency to address many E2 transitions in H_2^+ with $\Delta v = 2$. Given that these wavelengths
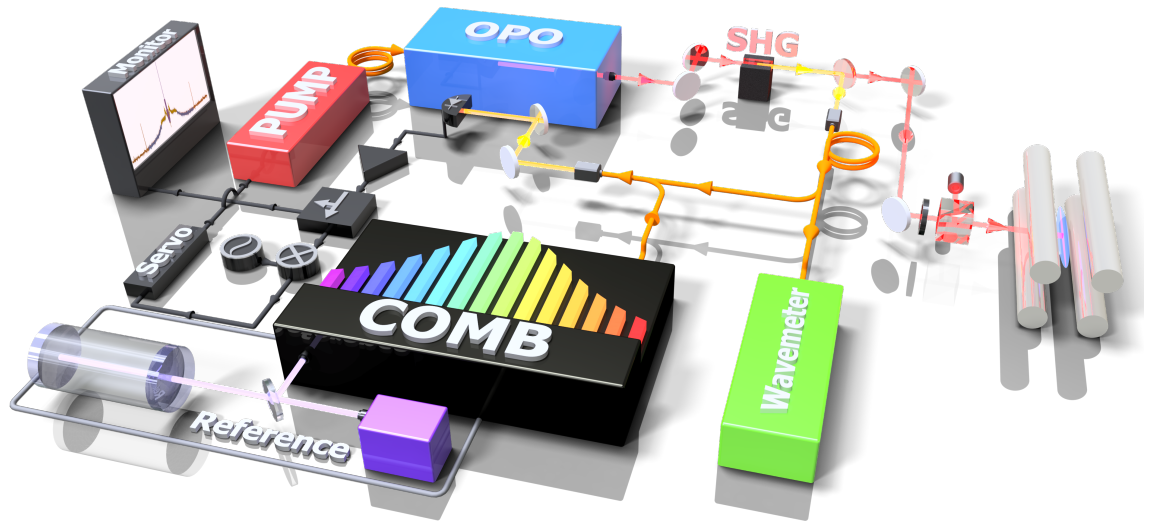
Figure 4.1.: Artistic representation of the setup of the spectroscopy laser system. The main devices of the apparatus are the OPO (blue box) and its pump laser (red box), next to a frequency comb (black box) with a reference laser (magenta box and resonator). The idler output of the OPO (red arrows) is frequency doubled in a SHG stage (top right). The remaining idler radiation is sent to the linear RF trap shown on the right, while its second-harmonic (yellow arrows and orange fibers) is split off to be measured with a wavelength meter ("wavemeter", green) and to generate a beat against the frequency comb. The beat signal is then used to stabilize the idler frequency using various electronic components and by acting on the pump laser of the OPO. The sequence of electronic components from the beat detection to the pump laser is: A photodetector, an amplifier, a splitter, a mixer with one input given by a local oscillator, and lastly, a servo acting on the pump laser's modulation input. The monitor (left) shows the RF beat signal in the locked state. Free space parts of the setup are shown as semi-transparent arrows, while fiber optics are shown in orange. Analog wires are shown in black.

fall within the mid-infrared range, where OFCs have yet to be well developed, a portion of the idler radiation is frequency doubled through the use of second-harmonic generation (SHG). The frequency-doubled radiation can then be overlapped with OFC-radiation, thereby generating a heterodyne beat, while simultaneously being measured by a wavelength meter. The combination of both realizes the aforementioned requirement of an accurate frequency measurement.

To additionally stabilize the frequency, the beat is employed further: Already from radio-frequency technology, it is well established that two frequencies can be made essentially identical by stabilizing the phase of their heterodyne beat. This procedure is referred to as the phase-locked loop (PLL) scheme and is also commonly used for the stabilization of laser frequencies. In the case of this work, the beat is employed to lock the phase of the idler radiation to the OFC, with feedback applied to the pump laser of the OPO. The modulation of ω_p is transferred to ω_i, because ω_s is fixed by the OPO's internal resonator. The OFC is itself stabilized to an ultra-stable reference laser based either on ULE or on NEXCERA resonators [84, 85]. A schematic representation of the setup is shown in Fig. 4.1. For long-term stability, the whole

setup is referenced to a hydrogen maser (not shown), which is compared to the national time standard via GNSS (Global Navigation Satellite System), thus providing SI-traceability of the idler frequency.

To summarize, the entire setup transfers the stability of the reference lasers to the idler radiation through the use of frequency conversion mechanisms, an OFC, and PLL stages, while long-term stability is provided by a SI-referenced hydrogen maser.

4.1.2.2. Performance

In order to provide an independent measurement of the stability of the idler radiation as well as its frequency value, a second beat was generated with an independently stabilized OFC. A comprehensive analysis of these measurements is presented in Chapter 5.1. The key findings of the measurements are as follows:

The upper limit for the relative stability of the laser frequency in terms of linewidth and Allan deviations was determined to be $\leq 4 \times 10^{-14}$ and $\leq 1 \times 10^{-14}$, respectively. These limits are mainly attributable to the stability of the reference laser employed, with additional minor contributions from fiber-induced noise. It is therefore anticipated that the limits could be improved by utilizing a better reference laser, which has been demonstrated by other groups [86, 87]. The absolute inaccuracy of the laser frequency relative to the SI second, i.e. the international time standard, is $\leq 1.2 \times 10^{-14}$. A major contributor to this limit is the instability of the hydrogen maser. Similar to the reference laser, alternatives with better stability exist, such as an optical fiber link to a metrology institute [88, 89, 90] or a technically more advanced hydrogen maser. If one could be obtained, an improved accuracy were expected.

The locking scheme of the OPO coupled with the aforementioned stability could be demonstrated at several output wavelengths of the OPO's idler, all corresponding to a transition in either H_2^+ or HD^+. This demonstrates the potential of the developed setup to realize an all-in-one system capable of interrogating numerous transitions within MHIs. The achieved output power available for spectroscopic applications was as large as $1\,W$, depending on the wavelength. It is anticipated that this could be increased further, given that the optical setup is not currently optimized for maximum power throughput.

To the best of our knowledge, the combination of the above attributes is unique and represents the most metrologically advanced OPO in the world.

4.2. Experimental procedures

In order to accomplish spectroscopy of a rovibrational transition in H_2^+, it is necessary to adapt the procedures established in our group for HD^+, the details of which have been published elsewhere [23, 81, 82, 91]. This is primarily due to the previously described absence of rovibrational E1 transitions in H_2^+. These types of transitions underlie both, the state preparation and spectroscopy methods employed for HD^+. Therefore, replacements for both must be found and implemented.
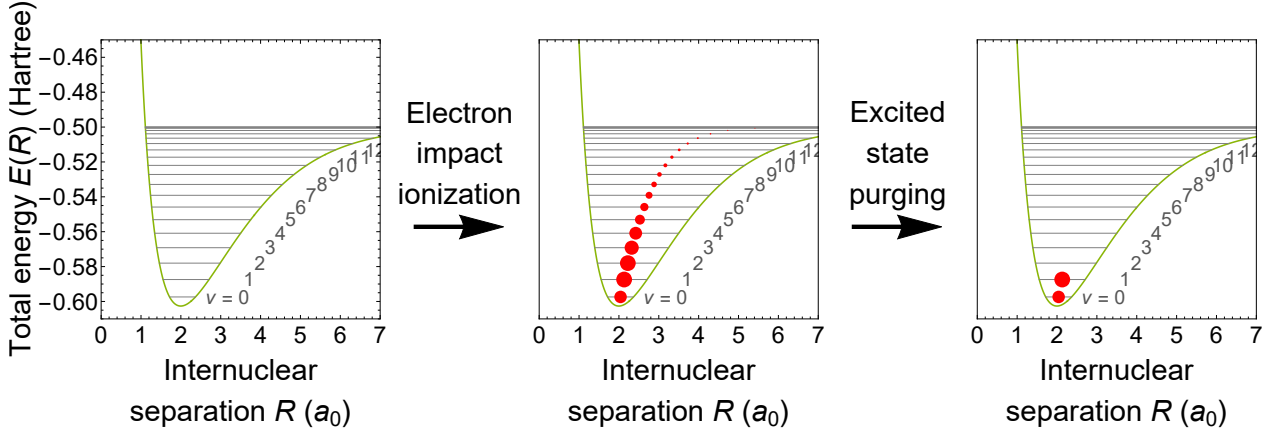
Figure 4.2.: Loading and state preparation of H_2^+. Left: the green curve depicts the molecular potential of the electronic ground state of H_2^+, obtained within the Born-Oppenheimer approximation as a function of the separation of the nuclei R. Within this curve, bound vibrational levels are indicated and labeled with their respective quantum number v. **Center:** Following electron impact ionization of neutral para-H_2 gas, the H_2^+ ions are distributed among many vibrational levels. For each level, the magnitude of population is indicated by the size of the red circle (experimental data taken from [92]). **Right:** After irradiation with 405 nm and 313 nm lasers, H_2^+ in excited vibrational levels $v > 1$ are dissociated ("excited state purging"). The levels $v = 0$ and $v = 1$ remain unaffected, since the photodissociation cross-section from both levels is negligibly small at the employed wavelengths [93].

4.2.1. State preparation of MHIs

The distribution of internal states after electron impact ionization depends on the isotopologue. The reason is the afore discussed presence or absence of strong E1 transitions (Sec. 2.1.4). If E1 transitions are allowed (e.g., for heteronuclear isotopologues), the internal state will decay to the ground rovibrational level on timescales of milliseconds [94]. This decay is counteracted by black-body radiation (BBR), which is non-negligible due to the present apparatus being operated at room temperature. At this temperature, rotational transitions of the vibrational ground state can be driven by BBR. A steady state is formed, which has been described in detail [95]. To counteract this, a sophisticated technique using lasers has been implemented by our group [91], which can prepare a significant amount of HD^+ in the rovibrational ground state ($v = 0$, $N = 0$). The method works by driving E1 transitions between suitably selected rovibrational states and awaiting the subsequent decay.

Due to the absence of E1 transitions in homonuclear isotopologues, this method is not applicable. The lifetimes of excited vibrational and rotational levels are within the range of days to weeks [52], which is considerably longer than the trapping times of our apparatus. Furthermore, the extensive distribution among vibrational levels after electron impact ionization [92] and the small magnitude of E2 transition moments render a preparation technique using lasers challenging.

As an alternative, we have developed a more straightforward method. A substantial amount of H_2^+ is loaded into the trap, after which the majority of molecules in undesired states is dissociated using lasers prior to the spectroscopy. This is made possible by the wavelength-dependent

cross-section of vibrational levels [93]. As may be anticipated intuitively, energetically lower levels will be largely unaffected by photons with an energy smaller than the level's dissociation energy. Moreover, the structure of the nuclear wavefunction gives rise to wavelength-specific vanishing cross-sections, depending on the vibrational quantum number. As a consequence, either a single or a combination of multiple dissociation lasers can be utilized to leave selected vibrational levels unaffected, while all others are dissociated and thus removed from the trap. The result is a vibrationally well-prepared ensemble of H_2^+.

This relatively simple method does not allow for a preparation of the other quantum numbers. However, it can still work particularly effective for para-H_2^+ due to the simplicity of its hyperfine structure. As has been previously discussed, the internal structure of rovibrational states in para-H_2^+ is quite simple, consisting of either one or two states. Therefore, the remaining population is with a relatively high probability in the desired hyperfine ground state, and no further preparation is required. For many other MHIs, this procedure may not be as effective, since the remaining population will distribute among all hyperfine levels, thereby decreasing the effective population in a specific state. A schematic representation of the concept is shown in Fig. 4.2.

Note that a state preparation of H_2^+ that is better suited for transitions starting from a different v as the one chosen in this work could be realized with the same method by exchanging the employed dissociation lasers. In particular, their wavelengths should be chosen in a manner that minimizes the dissociation cross-section of the target v, while maximizing all other cross-sections.

4.2.2. Spectroscopy procedures

4.2.2.1. Surpassing the Doppler-effect

As outlined before, the sympathetic cooling technique achieves ion temperatures at the level of a few millikelvin. The residual Doppler-broadening at these temperatures limits the achievable spectroscopic resolution to a few megahertz, which is insufficient for the desired level of accuracy of MHI research aims. To surpass the limitations imposed by the Doppler-effect and achieve even higher resolution, novel spectroscopy techniques were developed. Trapped Ion Cluster Transverse Excitation Spectroscopy (TICTES, [82]) managed to set new limits on the relative precision, with which MHIs can be interrogated, and multiple advances have been made since. The technique exploits the restricted transverse motion of ions, which under specific conditions can be strongly confined to the trap axis. If the degree of confinement is sufficiently tight, the motional extent of the ions is significantly reduced and the Dicke-regime is attained, in which Doppler-broadening is suppressed [96]. This enabled the observation spectroscopic linewidths that were much narrower than the Doppler-broadened limit. Other techniques, such as two-photon excitation, have also been demonstrated successfully [97], although they are more restrictive with regard to the transition that is to be interrogated.

4.2.2.2. Details of procedures

To ensure the efficacy of experimentation, it is imperative to implement a spectroscopy procedure that enables the control of particles, facilitates the spectroscopic readout, and minimizes

the influence of systematic effects. In general, all procedures adhere to the same principles, as follows: (1) MHIs are loaded and their spectroscopic ground state is prepared (see Sec. 4.2.1), (2) the amount of trapped MHIs is detected by making use of their secular frequency (see Sec. 4.1.1), (3) the spectroscopy and additional auxiliary lasers are irradiated, and (4) the population is detected once more. Within the present apparatus, the spectroscopy is done in a dissociative manner: following a successful excitation of the interrogated transition, the ion is dissociated. The dissociation is performed by an auxiliary laser during step (3). The resulting decrease in the number of trapped molecular ions between steps (2) and (4) is the spectroscopic signal.

In order to determine and mitigate potential systematic effects, and due to the dissimilar state preparation techniques for different MHIs, the details of the procedures vary. The procedures for HD^+ have been previously described in detail [23, 81]. The present discussion will focus on the adaptations implemented when transitioning to H_2^+.

Firstly, no lasers are employed for rotational cooling. Instead, following the loading of H_2^+ into the trap, excited stage purging is performed through the irradiation of 405 nm and 313 nm lasers for 30 s with respective power levels of a few tens and a few milliwatts. The wavelengths of these lasers are chosen to minimize the dissociation in the desired spectroscopic ground state ($v = 1$) while maximizing that of higher vibrational levels. It would be advantageous to additionally dissociate ions in $v = 0$ during this phase. In view of the details of the photo-dissociation cross sections [93], this requires the use of an additional laser with a wavelength of $\simeq 115$ nm. At this wavelength, the cross section of ions in $v = 1$ is vanishing due to the specific structure of the nuclear wavefunction of this state. However, the realization of a laser system at this wavelength, although feasible, is technically highly challenging. Consequently, the decision was taken to attempt spectroscopy without dissociating $v = 0$ ions. It was found that the additional statistical noise introduced by the background loss of these ions was within acceptable limits, and the experiment could proceed without having to rely on such an additional laser.

Secondly, the amount trapped H_2^+ is detected in a different manner. In contrast to the approach employed for HD^+, where the secular motion is resonantly excited, a secular excitation spectrum is recorded. In terms of the applied frequency ω (see Sec. 4.1.1) this translates to it being scanned over a large range, as opposed to remaining fixed. This is done in order to monitor the amount of co-trapped H_3^+ ions, which are generated parasitically in the system. From the measured fluorescence trace, the amount of trapped H_2^+ is determined through the strength of its corresponding peak in the spectrum. A depiction of the employed procedure is shown in Fig. 4.3. The procedure is repeated numerous times for a fixed spectroscopy laser frequency, in order to obtain sufficient statistics for signal and background data. Note, that the spectroscopy wave is blocked at all times during the background procedure. The value and uncertainty of signal and background are computed as the mean and standard error of the mean of the corresponding data sets. A spectroscopic line is obtained by repeating this for various spectroscopy laser frequencies.
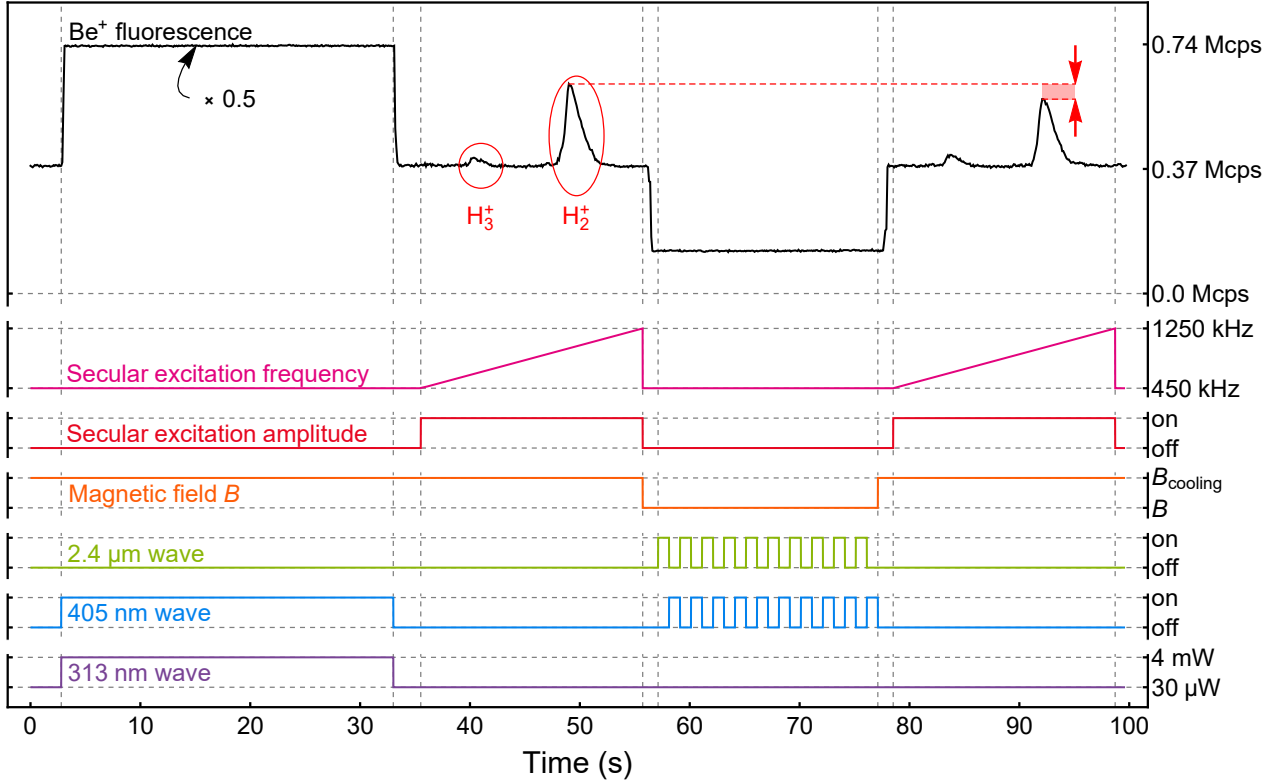
Figure 4.3.: The H_2^+ spectroscopy procedure (ED. Fig. 1 of Sec. 5.2, first published in Nature Physics). The black curve displayed at the top shows the fluorescence of beryllium ions due to the Doppler-cooling laser over the course of a single run of the spectroscopy procedure. One run of the experiment begins with the dissociation of vibrationally excited H_2^+ for a period of $\sim 30\,\mathrm{s}$. Subsequently, an excerpt of the secular excitation spectrum of the trapped ions is recorded. Peaks corresponding to H_2^+ and H_3^+ are detected. The ensuing interleaved irradiation of the spectroscopy and dissociation wave excites the rovibrational transition in H_2^+. The interleaved method is chosen to eliminate a potential influence of the dissociation laser on the spectroscopy transition. The laser excitation is followed by a second recording of the secular excitation spectrum. The decrease of the H_2^+-peak in the spectrum, indicated by the red arrows, dashed lines, and shaded area, is the spectroscopy signal for this run. For background runs, the spectroscopy wave is kept off at all times; otherwise, the procedure is identical. The colored curves in the bottom half illustrate individually labeled parameters and their adjustment during the run, each with corresponding labeling on the right-hand ordinate.

4.2.3. Laser spectroscopy of H_2^+

With the availability of a suitable laser system (Sec. 4.1.2), as well as a trap apparatus that has already demonstrated the capability of ultra-high resolution spectroscopy of HD^+, laser spectroscopy of H_2^+ is the logical next step. It is therefore necessary to identify a target transition. In light of the rovibrational levels' internal structure discussed in Sec. 2.1.3, it is evident that a transition of the type $N \to N' : 0 \to 2$ or vice versa should be selected. Furthermore, the residual population of H_2^+ remaining after state preparation (Sec. 4.2.1) indicates that the largest signal strengths should be expected when the spectroscopic ground state is chosen to be $v = 1$. Since the distribution of the population among rotational levels within $v = 1$ is unknown, the transitions $(v, N) : (1, 0) \to (3, 2)$ and $(1, 2) \to (3, 0)$ have equal weight in consideration. Both transitions are allowed under the selection rules of E2 transitions [55]. The former was selected as an interrogation target arbitrarily.

A depiction of the target transition within the previously presented curve of molecular energy is shown in Fig. 4.4 a, while its spin structure is depicted in Fig. 4.4 b. Additionally shown are the Zeeman splittings for a finite magnetic field, which is present during the spectroscopy. In order to determine the desired properties, namely the spin-averaged frequency $f_{\text{spin-avg}}$ and the spin-rotation coefficient c_e, it is necessary to measure the two spin components f_a and f_b. In the presence of the magnetic field applied during spectroscopy, f_a and f_b will split into various Zeeman sub-levels. In order to extract them from measured Zeeman components of the transition (shown as f_{a1}, f_{b1} and f_{b2}), a knowledge of the Zeeman shift coefficients or the magnetic field, either theoretical or experimental, is imperative. This extraction was performed through a fitting of the magnetic field to the observed transition with the help of the theoretical Zeeman coefficients. Further details are given in Sec. 5.3.
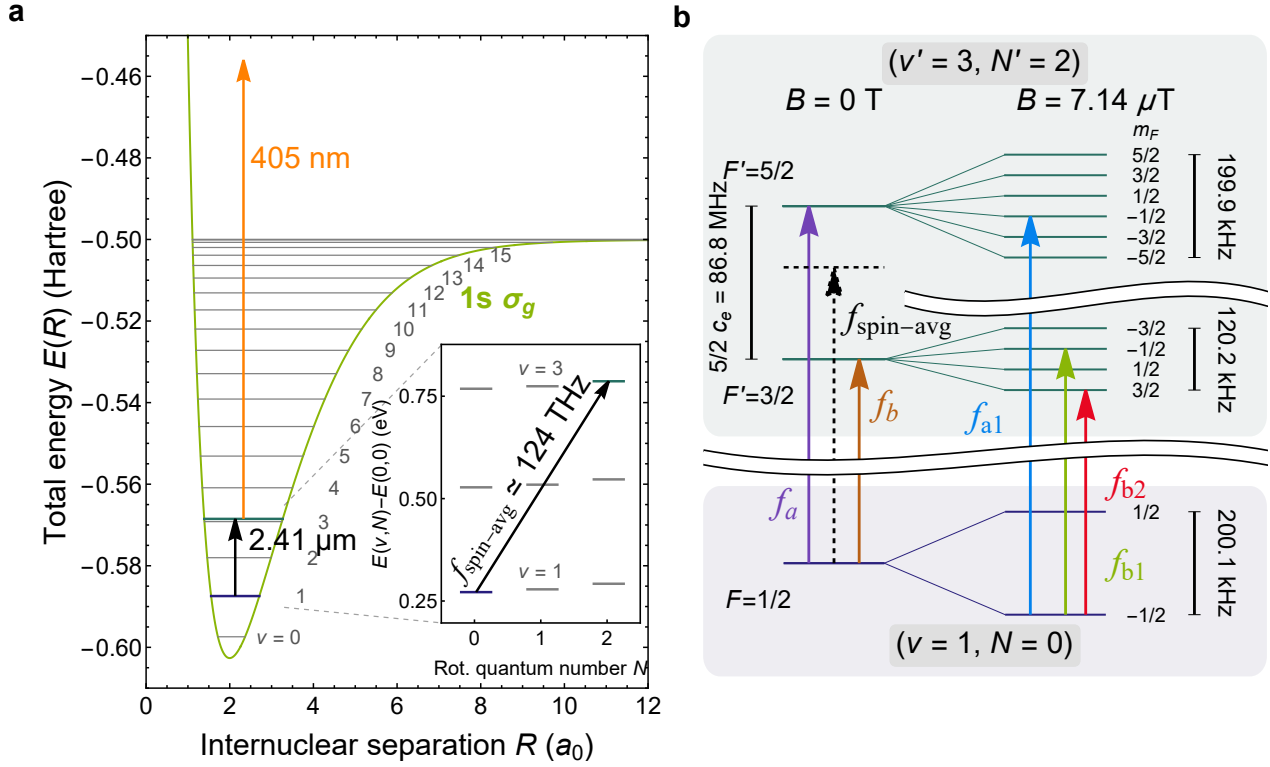
Figure 4.4.: Energy diagram of H_2^+ (Adapted from ED Fig. 1 of Sec. 5.2, first published in Nature Physics, and Fig. 1 of Sec. 5.3). **a:** Similar depiction as Fig. 2.2, showing the total energy of H_2^+ as a function of the separation of the nuclei in the electronic ground-state. The transition of interest is indicated by the black arrow. The orange arrow illustrates the laser used for the dissociation of excited ions. The inset shows the three energetically lowest rotational states of the vibrational levels $1-3$, with the abscissa representing the rotational quantum number N. Note the change in scale and unit of the ordinate. **b:** The spin structure of the target transition. Left: the structure at zero magnetic field. The two transitions f_a and f_b are shown in purple and brown, respectively. They are separated by $5/2 c_e$. The indicated $f_{\text{spin-avg}}$ is the transition frequency without consideration of the internal angular-momenta-dependent structure. It is not a directly measurable property. Right: the structure in the presence of a finite magnetic field applied during spectroscopy. The three measured Zeeman components are indicated by a blue, a green, and a red arrow and corresponding labels. F, m_F and F', $m_{F'}$ are the total angular momentum and total angular momentum projection quantum numbers of the ground and excited state, respectively. Note that the notation has been adapted in comparison to ED Fig. 1 of Sec. 5.2, in order to match the one which is used in Fig. 1 of Sec. 5.3.

5. Cumulative part of the dissertation

This chapter is comprised of three sections, each of which is a manuscript related to this thesis.

Sec. 5.1 provides a detailed description of the setup and characterization of the spectroscopy laser system developed as part of this work. The results were previously summarized in Sec. 4.1.2.2.

Sec. 5.2 comprises the first spectroscopic study of H_2^+, with the measurement of Doppler-broadened components as well as a study of systematic effects of an E2-transition performed on HD^+.

In Sec. 5.3, the second spectroscopic study of H_2^+ with the observation of Doppler-free single Zeeman components of the transition is presented.

A summary of the results of Sec. 5.2 and Sec. 5.3 is given in Chapter 6.

5.1. Metrology-grade spectroscopy source based on an optical parametric oscillator

Copyright notice:

The supplementary material of this manuscript is presented in Appendix B.

My contributions to the work:

- I contributed to the concept of the work.

- I have set up the OPO laser system, frequency-doubling stage, and locking circuit.

- I made significant contributions to the measurements underlying the work.

- The majority of the data analysis and the generation of the corresponding figures were performed by myself.

- All authors discussed the data and interpretations of the manuscript.

- The manuscript was written partially by me.

Metrology-grade spectroscopy source based on an optical parametric oscillator

M. R. SCHENKEL,[1,2] **V. A. VOGT,**[1] **AND S. SCHILLER**[1,3]

[1]*Heinrich-Heine-Universität Düsseldorf, Mathematisch-Naturwissenschaftliche Fakultät, Institut für Experimentalphysik, 40225 Düsseldorf, Germany*
[2]*magnus.schenkel@hhu.de*
[3]*step.schiller@hhu.de*

Abstract: Continuous-wave optical parametric oscillators (OPOs) are widely tunable and powerful sources of narrow-linewidth radiation. These properties make them suitable for a wide range of spectroscopic studies - but so far not at the metrological level. Indeed, although important technical OPO developments occurred more than two decades ago, and commercial devices have been available for nearly as long, the long-hoped-for the potential of these devices, providing simultaneously ultralow linewidth, ultrahigh frequency stability, ultrahigh frequency accuracy, and wide wavelength coverage has not yet become a reality. Here, we present an OPO metrology system suitable for optical spectroscopy with ultra-high resolution and accuracy in the 2.2 - 3.9 μm range. The system relies on the second-harmonic generation of the idler wave to bridge the gap to the near-infrared regime where frequency combs are readily available. By actively controlling the pump laser frequency, the idler radiation is phase-locked to an optically stabilized frequency comb, enabling a full transfer of the frequency comb's spectral properties to the idler radiation and measuring the idler frequency with ultra-high precision. We reach fractional line widths and Allan deviations of the idler radiation at the level of 4×10^{-14} and 1×10^{-14}, respectively. We also perform a thorough characterization of the stabilized OPO via a comparison with a second, independent optically stabilized frequency comb and thereby determine an overall idler frequency systematic uncertainty of less than 1.2×10^{-14}. Sources of residual frequency noise are identified. The system delivered excellent results in high-accuracy spectroscopy.

1. Introduction

High-resolution laser spectroscopy of atoms and molecules is a key branch of physics and physical chemistry. The spectroscopic study of many species can be performed with semiconductor lasers emitting in the near-infrared (NIR) spectral range and even in the visible range. But these sources do not satisfy all needs. An important area of laser spectroscopy is rovibrational spectroscopy, where one often wishes to measure a large set of transitions of a given molecular species, or of several different species, hence requiring a wide tuning range. The mid-infrared (MIR) range provides the most important window on rovibrational spectra. In this range, continuous-wave (cw) optical parametric oscillators (OPOs) are a unique type of spectroscopy source; their output can cover more than an octave in frequency, and the output power can be 1 W or higher. The combination of these properties sets them apart from other important MIR sources, such as DFB and quantum cascade lasers or difference-frequency generation.

Key developments in the design and performance of cw OPO devices and spectroscopy demonstrations, occurred more than two decades ago, with the first demonstrations of mode-hop-free oscillation [1–8]. Soon, the first commercial OPO devices became available. Since then, many groups have successfully used cw OPOs for diverse applications in molecular spectroscopy

[9–21], and in some instances atomic spectroscopy [22]. Only in the past decade has there been a greater need to achieve ultra-high resolution and corresponding frequency accuracy with OPOs. Metrology-grade OPOs would be useful, for example, in fundamental physics to probe the hyperfine transition of highly charged ions [23], the rovibrational transitions of simple (few-electron) molecules (such as the molecular hydrogen ions [24,25], the neutral hydrogen molecules [26–31], and the helium hydride ions ([32,33] and references therein)), or to search for a time-drift of molecular vibrational frequencies [34–37].

The wide tuning range of cw OPOs immediately raises the question of how to precisely determine the actual emission frequency. With the invention of the optical frequency comb (OFC) [38,39], a new tool emerged for measuring optical frequencies with an accuracy improved by many orders of magnitude compared to previous means. Already early studies explored how to combine an OPO with an OFC in order to enable OPO output frequency determination. Importantly, an OFC also offers the possibility to serve as a reference for stabilizing the OPO frequency by feedback control [40]. The latter option is superior to locking the frequency to molecular absorption lines because they do not offer a continuous wavelength coverage. An additional benefit would be a link of the visible and NIR regimes with the MIR regime [41]. These early demonstrations have been followed by further studies, and Table 1 presents a selection of those performed over the past decade and aimed at metrology. It is evident that it has not yet been possible to imbue an OPO with the four key properties of a metrology-grade spectroscopy source: ultralow linewidth, ultrahigh frequency stability, ultrahigh frequency accuracy, and wide wavelength coverage. The contrast with what has been achieved with diode lasers is striking: the first three properties are achieved in many metrological studies (mostly for atomic spectroscopy, e.g. for optical atomic clocks [42,43]). Clearly, there appears to be an unrealized potential for OPOs, i.e. the opportunity for developing methods capable of pushing both the linewidth and the long-term frequency instability down to the Hertz level.

Table 1. Comparison of some features of the present source in comparison to selected published works of other groups. The acronyms are defined in the text. τ is the integration time.

Ref.	Technique	Idler range (μm)	Frequency stability of idler radiation		Idler output power
			Short-term (linewidth)	Long-term (Allan deviation or other)	
Ricciardi et al. [14]	Frequency lock of pump and signal to NIR OFC	[2.7, 4.2]	$\leq$ 200 kHz at 100 ms	$\sigma_y \leq 3 \times 10^{-12}/\sqrt{\tau}$ for $\tau \in [1, 200]$ s	>1 W
Peltola et al. [44]	Frequency lock of idler's SH to NIR OFC	[2.7, 3.4]	$\simeq$ 1 MHz	$\sigma_y \in [10, 200]$ kHz for $\tau < 10$ s	>0.5 W
Ricciardi et al. [45]	Direct cavity stabilization	[2.7, 4.2]	920 Hz at 100 ms	not stated	$\simeq$ 0.5 W
Karhu et al. [46]	OPO locked to a MIR OFC	[2.5, 4.4]	0.5 MHz at 0.15 s, 1.5 MHz at 1 s	Standard deviation of 90 kHz over 20 min	up to 0.8 W
Zhang et al. [20]	Pump locked to NIR OFC, OPO cavity locked to ULE resonator	[2.6, 4.3]	<20 kHz at 1 – 5 s	σ_y <1 kHz for τ >1 s	$\simeq$ 0.4 W
This work	PLL of idler's SH to NIR OFC	[2.2, 3.9]	$\leq$ 5 Hz at 1 – 10^3 s	$\sigma_y \leq$ 3 Hz for τ >1 s	>1 W

Here we present a general and effective method of OPO frequency stabilization that is fairly independent of the desired output wavelength. By locking the OPO's idler frequency to an OFC, we simultaneously achieve all four of the key properties above, improving these parameters by a combined factor of more than 10^4. We thereby demonstrate a MIR spectroscopy source with a fractional frequency instability $\leq 1 \times 10^{-14}$ on timescales between 1 and 10^5 s, an idler linewidth on the order of a few Hertz, and an SI-traceable frequency. Our frequency stabilization scheme can be operated at different idler wavelengths. This demonstrates that the method is wavelength-independent.

1.1. Frequency stabilization approaches

Since the frequency conversion process in an OPO must satisfy energy conservation at the photon level, the frequencies ω_p, ω_s and ω_i of pump, signal and idler waves, respectively, are related by

$$\omega_p = \omega_s + \omega_i \,. \tag{1}$$

If the idler wave is the main interest for a spectroscopic application, two different approaches to stabilize its frequency ω_i may be distinguished.

Consider first the approach where both ω_p and ω_s are actively stabilized, so that according to Eq. (1) the idler frequency is also stabilized. To do so, both the pump and the signal wave frequencies must be stabilized separately. Both these frequencies usually fall into the NIR range (e.g. $\lambda_p = 1.06\,\mu m$ and $\lambda_s \in [1.45\,\mu m, 2.07\,\mu m]$ in this work), where narrow-linewidth and ultra-stable optical frequency combs (OFCs) can be realized with relative routine. These two properties can be achieved by phase-locking the OFC to a reference laser, which is itself frequency-locked to an ultra-stable reference cavity.

The frequency of the pump wave can be stabilized to such a comb. It is more difficult to do so for the signal wave because its frequency is determined by the resonance of the OPO cavity. One needs the ability to control the optical path length of the cavity with high bandwidth. This is challenging in view of the typical design of the OPO cavity and the cavity length actuator. The task could be eased by employing either an OPO cavity that exhibits good passive stability or an intra-cavity electro-optic modulator for fast path-length control [20]. However, both options come with technical challenges.

For the most advanced applications, not only the provision of a narrow-linewidth spectroscopy wave (idler), but also the determination of its absolute frequency ω_i is required. Therefore, a second approach to idler frequency stabilization appears better suited: *measure* the idler frequency and act *only* on the pump frequency to control the idler frequency (see Fig. 1(a)). This control works by exploiting the 1:1 transfer coefficient from pump frequency change to idler frequency change when the signal frequency is not acted upon, Eq. (1). The frequency of the signal wave is at all times determined by the optical length of the OPO cavity, following its variations due to perturbations. This is a source of frequency noise that needs to be compensated. The pump frequency will be regulated so as to keep the idler frequency precisely fixed at a desired value, compensating for both the OPO cavity length fluctuations as well as the pump laser's own fluctuations. Note that with this approach, neither the pump frequency nor the signal frequency will exhibit a particularly low frequency instability.

An example of this approach is the work of Peltola *et al.* [44]. They used second-harmonic generation (SHG) to bridge the gap between the idler frequency and the NIR, where the frequency of the second-harmonic (SH) wave $2\,\omega_i$ can be compared to mode of an OFC. In that work, the OFC was stabilized by locking the repetition rate to a hydrogen maser (H-maser) and the frequency $2\,\omega_i$ was determined using a frequency measurement of its beat with the OFC. A servo system acting on the pump frequency allowed obtaining a long-term stable idler wave frequency with Allan deviations at the sub-MHz level, but no reduction of its linewidth. The achieved frequency stability is summarized in Table 1.
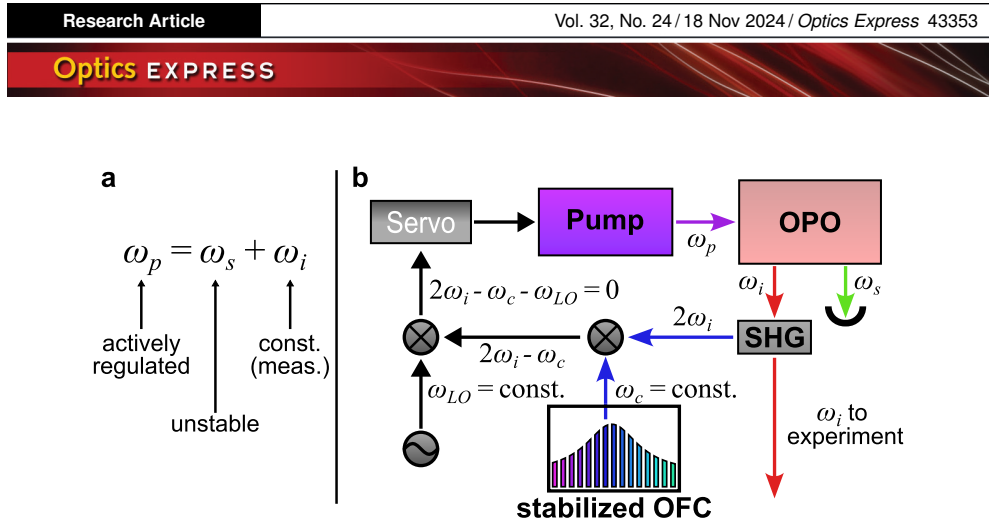
Fig. 1. Concept of the setup. a: The equation summarizes the concept. ω_p is regulated in order to keep the measured ω_i constant in time, while ω_s is left unstabilized and is affected by perturbations. **b:** An optically phase-locked OPO is implemented. The OPO is pumped at a frequency ω_p to generate the signal (ω_s) and idler (ω_i) frequencies. ω_i is then frequency-doubled in an SHG stage and mixed with an optically stabilized OFC, possessing a mode at frequency $\omega_c \approx 2\omega_i$. The generated beat is mixed with a local oscillator (LO) having a radio-frequency ω_{LO} in order to generate an error signal. It is the input to the servo that controls the pump frequency. Colored and black arrows are used for optical and analog signals, respectively. More details follow in Fig. 2.

In this work, we expand on this method, by implementing an ultrastable OFC and a phase-locked loop (PLL) of the idler frequency to this OFC, allowing to achieve not only long-term frequency stability but also excellent linewidth narrowing. The principle is shown in Fig. 1(b).

2.   Experimental setup

Our apparatus consists of three main units, shown in Fig. 2. Unit 1 (top) comprises the OPO as well as the optical and electronic components of the locking subsystem. Unit 2 (center left) contains a first OFC (OFC1) and its reference laser (L1). These are used for the stabilization of the OPO's frequency. Unit 3 (bottom) serves to characterize the OPO in the locked state, and therefore includes a second OFC (OFC2) with its own reference laser (L2). Unit 4 (center right) provides the H-maser as a reference clock in the radio-frequency (RF) domain. It delivers ultrastable RF signals to the other three units and is also required for the optical frequency measurement. The H-maser is continuously compared to the national time standard PTB (Physikalisch-Technische Bundesanstalt, Braunschweig) via a common-view Global Navigation Satellite System (GNSS) technique. This ensures SI-traceability of the absolute frequencies. All units are computer-controlled and connected via a network. We now describe the units in more detail.

Unit 1 contains the actual OPO with its pump laser, a SHG stage to convert the idler radiation, a wavelength meter (High Finesse WS-7 IR Super Precision), locking and monitoring electronics. The OPO is a commercial system (TOPTICA DLC TOPO, [47]), that generates >1 W of output power over the idler wavelength range of $2.2 - 3.9\,\mu$m. The corresponding signal range is $1.45 - 2.07\,\mu$m. The system consists of the OPO laser head and a ytterbium-doped fiber amplifier (Yb-FA) with up to 10 W output power. To seed the amplifier, we employ a separate commercial semiconductor laser (1.06 μm, TOPTICA CTL 1050) to benefit from its narrower free-running linewidth (<10 kHz at 5 μs according to the manufacturer). When unstabilized, the linewidth of the OPO's idler was previously determined to be $1 - 2$ MHz on a 25 ms timescale [47]. On similar timescales, but with the above seed laser, we observe a linewidth of $\simeq 100$ kHz, which
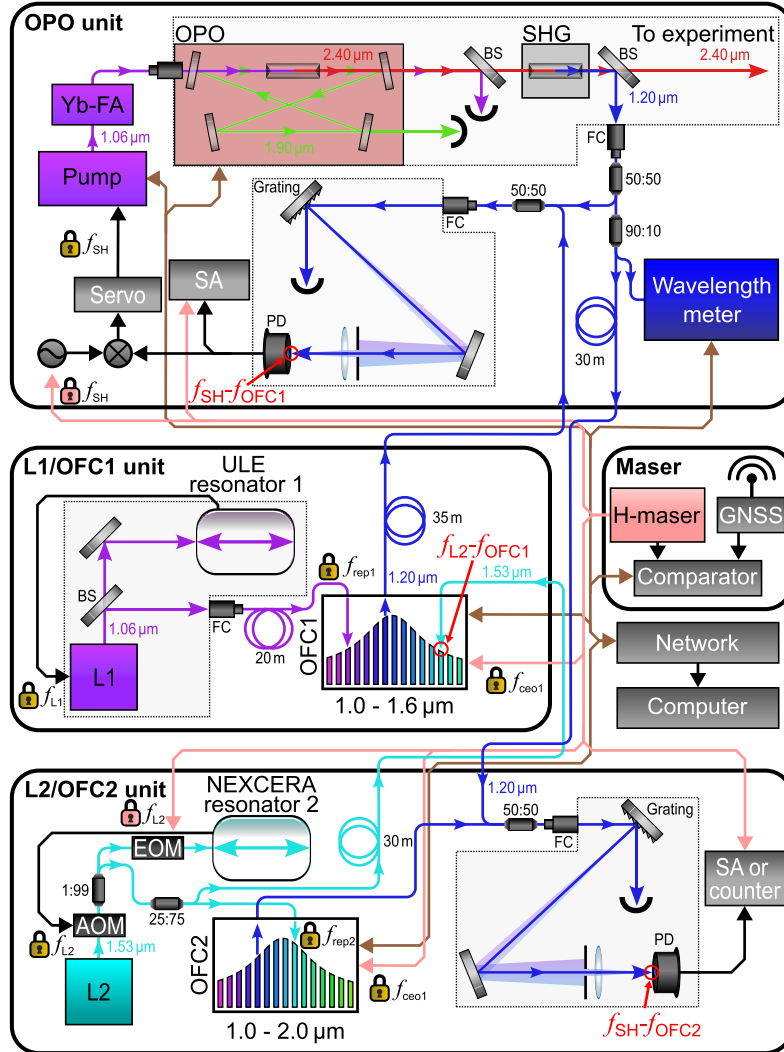
Fig. 2. Schematic of the setup. The individual black-framed boxes designate different units. **Top**: The OPO unit contains the OPO including pump and amplifier, the idler SHG unit and the wavelength meter, as well as the locking and monitoring electronics. **Center left**: The L1/OFC1 unit with the main reference laser L1, used to stabilize f_{rep1} of OFC1. A pick-off from OFC1 (shown here as an example centered at 1.2 µm) is sent to the OPO unit for idler frequency stabilization. **Bottom**: The L2/OFC2 unit, with L2 as the reference laser for f_{rep2} of OFC2. **Center right**: A hydrogen maser (H-maser) serves as the reference for all relevant RF sources. Individual wavelengths are shown in the figure by mapping the visible color spectrum to the wavelength range of the setup ([1.0 µm, 2.4 µm] → [purple, red]). Performance and measurements are monitored by computer control, connected to the individual components via network. Optical fibers are labeled for lengths >5 m. The H-maser analog signal, network connections, and other analog signals are shown in pink, brown, and black, respectively. Free-space parts of the setup are indicated as dashed-frame boxes. The padlocks symbolize active stabilization of the indicated frequency by a servo system (not shown). The padlock color gold denotes either a PLL lock or a PDH lock, while pink refers to a servo that implements a low-bandwidth frequency stabilization to the H-maser frequency. More details in the text. BS: beam splitter. FC: fiber coupler. AOM: acousto-optic modulator. EOM: electro-optic modulator. SA: spectrum analyzer.

increases to $3 - 5\,\mathrm{MHz}$ on timescales of a few seconds, due to jitter. Typical frequency variations are $200\,\mathrm{MHz}$ over several hours, with drift rates on the order of $0.6\,\mathrm{MHz/min}$.

The seed laser can be frequency-modulated with a high bandwidth (several ten MHz) via its current, which is crucial for realizing our locking scheme where the pump laser current is the actuator. Before being sent to the experiment, the full power of the OPO's idler wave is sent through a single-pass SHG setup containing a periodically poled lithium niobate crystal. In order to be able to generate the harmonic wave of the whole idler spectral range, we employ a crystal containing multiple grating periods, with periods between $33.3\,\mu\mathrm{m}$ and $36.0\,\mu\mathrm{m}$, and operating temperature in the range $20 - 200\,^\circ\mathrm{C}$. This combination of parameters allows us to find a suitable phase-matching condition for any wavelength in the idler's wavelength range. Owing to the high power of the idler radiation, a few milliwatts of the second-harmonic wave are generated in the single-pass configuration. This power is sufficiently high that the wave can be split into one part for generating a high-signal-to-noise-ratio beat with OFC1 and a second part for the wavelength meter, whose measurements are necessary for absolute frequency determination. To produce the beat, a fraction of the OFC1 output, spectrally centered around the idler's second-harmonic wavelength, is sent to the OPO unit via a $35\,\mathrm{m}$ long optical fiber, and there overlapped with the second-harmonic wave within the fiber, using a fiber combiner. The combined radiation is coupled out of the fiber, reflected off a grating, and directed onto the photodetector (PD). The signal-to-noise ratio of the beat generated in the PD is optimized by proper alignment of the grating. This beat signal is phase-locked to a RF signal of stable frequency (local oscillator, LO). To this end, the beat signal is mixed with the local oscillator (LO), and the low-frequency output of the mixer is the input to an appropriate servo that controls the pump laser's current, closing the loop. Overall, the idler frequency is phase-locked to a mode of the OFC.

Unit 2 contains the reference laser L1 ($1.06\,\mu\mathrm{m}$, Mephisto Innolight Nd:YAG) and OFC1 (Menlo Systems FC1500-250-ULN). Its repetition rate $f_{\mathrm{rep,1}}$ is stabilized by phase-locking one comb mode to L1, while the carrier envelope offset frequency $f_{\mathrm{ceo,1}}$ is stabilized to the H-maser. L1 itself is stabilized to a ULE resonator with a finesse of $\simeq 500\,000$ (resonator 1) using the Pound-Drever-Hall (PDH) technique, with the modulation applied to the laser's frequency actuator, a piezo-electric transducer.

Finally, in the lower part of Fig. 2, unit 3 contains the second OFC (OFC2) and a separate reference laser L2 at a wavelength of $1.53\,\mu\mathrm{m}$ (NKT Koheras Basik E15). Similar to above, the comb's repetition rate $f_{\mathrm{rep,2}}$ is phase-locked to L2, while $f_{\mathrm{ceo,2}}$ is stabilized to the H-maser. Except for the shared H-maser that provides f_{ceo} stabilization, the two combs are completely independent systems. L2 is also locked via the PDH technique to the resonator 2, a NEXCERA resonator [48] with a finesse of $700\,000$. NEXCERA is a novel spacer material for resonators [49], designed to be operated at room temperature. In contrast to L1, an acousto-optic modulator (AOM) is required for providing fast control of the frequency of the L2 output wave, since the laser itself does not have a high bandwidth modulation input. A sideband lock is implemented [50,51], where the laser wave is phase-modulated using an electro-optic modulator (EOM), and one of the modulation sidebands is locked to the resonator instead of the carrier. The sideband lock is used in order to be able to compensate the drift of the resonator. A detailed explanation is given in section 3.3. To characterize the performance of the two reference lasers, a portion of the radiation of L2 is sent to OFC1 and then measured against it.

3. Performance

In order to characterize the spectral properties of the OPO's idler radiation, beats between several sources were produced. In Fig. 2 these beats are indicated by red circles together with their corresponding optical frequency differences. First, a beat between OFC1 and L2, $f_{\mathrm{L2}} - f_{\mathrm{OFC1}}$, gives the combined instability level of the employed reference lasers L1, L2. Additionally, it

includes the locking performance of the PLL of OFC1 to L1 and any fiber noise originating from the 30 m long fiber used to send L2 radiation to OFC1.

In a second step, the PLL of the OPO is examined by monitoring the beat $f_{SH} - f_{OFC1}$ in the locked state. Finally, the absolute stability of the OPO's idler frequency is investigated, by measuring a beat between its SH wave and OFC2, $f_{SH} - f_{OFC2}$. This simultaneously gives the most accurate upper limit of the frequency instability for the system as a whole, including all fiber noise and other noises. The analysis for short timescales is presented in Section 3.1, and the analysis for long timescales follows in section 3.3. These analyses were performed with the OPO set to an idler wavelength of 2.81 μm, corresponding to a signal wavelength of 1.71 μm and an idler second-harmonic wavelength of 1.40 μm. In Sec. 3.5 we argue that the described performance can be achieved at all wavelengths within the output range of the OPO.

3.1. Short-term performance of the idler radiation

The beat $f_{L2} - f_{OFC1}$ shown in Fig. 3, panel 1a, is an average of many consecutive sweeps of the spectrum analyzer, each of duration 5 s and measured at a resolution bandwidth (RBW) of 1 Hz. Note that the individual traces could be averaged without any consideration of either resonator's drift, since the center frequency drifted by less than 1 Hz over the course of the entire data acquisition. This has two different reasons: in the case of resonator 1 the drift is negligible on the timescale of the measurement, and in the case of resonator 2 it is actively compensated, see sec. 3.3. From the beat we deduce a full-width half-maximum (FWHM) linewidth of 9 Hz. In the phase-noise spectrum of $f_{L2} - f_{OFC1}$, Fig. 3, panel 1b, small sidebands at frequencies of 50 Hz and 510 Hz can be observed. We believe that the origin is fiber noise occurring in both fibers that deliver the radiation from L1 and L2 to OFC1. Due to the modest strength of the sidebands, they are not significant for the current analysis and also have not impacted a recent spectroscopic study [25].

Data on the OPO's phase-locked loop performance, i.e. the frequency and phase noise of the beat $f_{SH} - f_{OFC1}$, is displayed in Fig. 3, center column. This data on the beat does not yet yield any information on the absolute stability of the idler frequency, but rather on how well it follows OFC1. The measured linewidth, 3 Hz FWHM, is caused by the RBW of the employed spectrum analyzer - as is expected for a properly working phase lock. From the phase-noise spectrum, panel 2b, we determine a signal-to-noise ratio of 70 dB in a RBW of 1 Hz. Additionally, a single significant sideband is observed, at a frequency of 810 Hz. The source for this is intrinsic to the setup: it is caused by acoustic noise originating from the Yb-FA, as was confirmed by a comparing the acoustic noise spectrum in the proximity of the OPO with the Yb-FA turned on and off.

Next, we consider the beat $f_{SH} - f_{OFC2}$. Its analysis is shown in Fig. 3, right column. Similar to panel 1a, panel 3a shows consecutive beat spectra measured over a total time of more than 30 min, averaged without any re-centering of individual traces. A Lorentzian fit finds a linewidth of 10 Hz (FWHM). This is only 1 Hz larger than the linewidth of the beat of the reference lasers (panel 1a). The spectrum (panel 1b) also exhibits several sidebands with frequencies in the range 10 - 50 Hz. These sidebands are not observed in the beats in panels 1a and 2a. The reason for this is that they are caused by fiber noise occurring in the 35 m long fiber guiding OFC1 radiation to the OPO (see Fig. 2), which only contributes to the measurements underlying panel 3, see section 3.2. In the phase-noise spectrum 3b, the sideband observed in the PLL signal at 810 Hz is again visible.

3.2. Fiber noise

To investigate the noise observed in the beat of the idler's second-harmonic and OFC2 (Fig. 3, panels 3a and 3b), the optical path between OFC1 and the OPO was investigated. To this end, a round-trip propagation path for the idler's second-harmonic was set up, by using two fibers similar
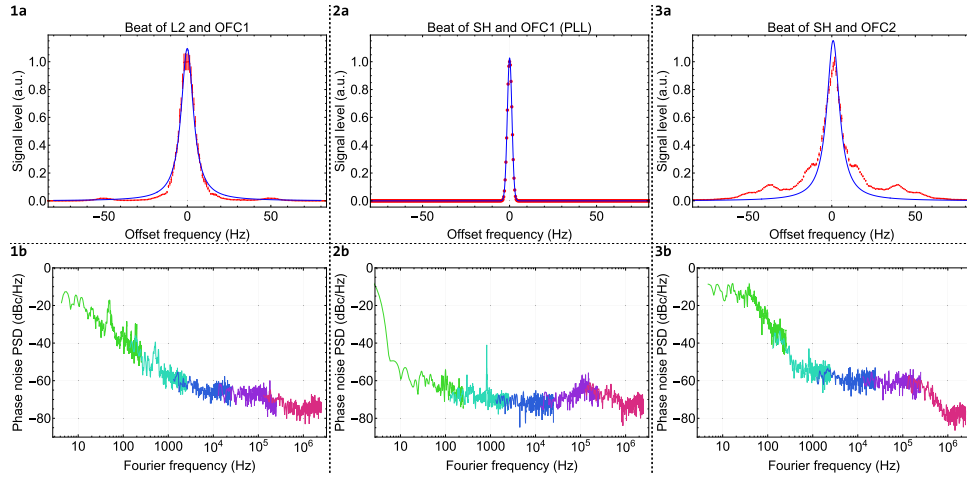
Fig. 3. Analysis of the beats between different units, marked by red circles in Fig. 2.
Left column: beat $f_{L2} - f_{OFC1}$ between L2 and OFC1 locked to L1, showing the combined instability of the two reference lasers. **Center column** is the PLL of the OPO, specifically the beat between the second-harmonic of the idler and OFC1 in the phase-locked state, here at a second-harmonic wavelength of $1.4 \, \mu m$. **Right column** shows the beat $f_{SH} - f_{OFC2}$ between the second-harmonic and OFC2, at the same wavelength $1.4 \, \mu m$. This is a direct determination of an upper bound for the instability of the OPO's idler wave frequency and includes all noise sources of the system (e.g. noise of the lasers themselves and fiber noise). Each column is split into a determination of the linewidth of the beat (top) and the phase-noise power spectral density (bottom, PSD). For the linewidth plots of the first and last columns, the data are an average of many consecutive sweeps (order 10^2) of 5 s duration each, at 1 Hz RBW. The error bars are the standard error of the mean. The data are fit by a Lorentz function, giving a FWHM linewidth of 9 Hz and 10 Hz, respectively. For the middle column, the data is from a single spectrum analyzer sweep. It is fit by a Gauss function (FWHM 3 Hz), the appropriate form considering the digital band-pass of the spectrum analyzer.

to the one shown in Fig. 2 connecting OFC1 and OPO. The pick-off of the second-harmonic, previously sent to OFC2, is now sent to OFC1 and then back to the OPO. There, a self-beat is generated with a reference wave (the part that is usually sent to the wavelength meter). Additionally, sidebands are modulated onto the OPO's pump laser at 10 MHz, allowing a beat signal to be obtained at an RF frequency rather than at DC.

The result is shown in Fig. 4. As can be seen, multiple side-peaks are observed at different frequencies ranging from a few Hz to 80 Hz. This is not surprising, since the fiber is exposed to the environment and thus transfers acoustic and mechanical perturbations onto the light passing through it. Since the offset frequencies corresponding to the spectral peaks match well with the sideband frequencies observed in the beat between the idler's second-harmonic and OFC2, we infer that the sidebands are caused by this fiber noise. Additionally, a minor broadening of the carrier's linewidth is observed, 2 Hz. This can also explain the small broadening observed in the comparison of Fig. 3, panels 1a and 3a. We thus conclude that the fiber noise due to this fiber is the main source of frequency instability of the entire OPO metrology system, apart from the instability of the reference lasers themselves.
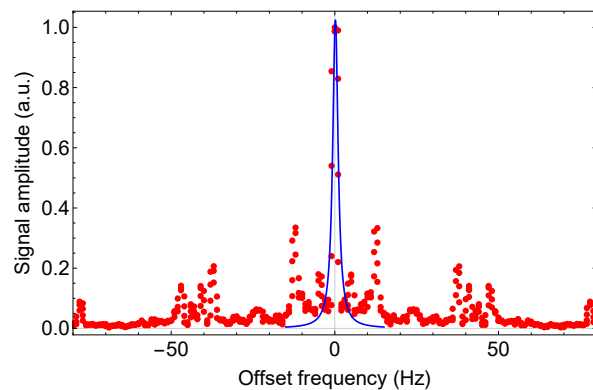
Fig. 4. Fiber noise of the longest fiber path in the system (35 m), connecting unit 1 and unit 2. The self-beat of the SH, sent on a round-trip to OFC1 and back, is shown in red. The blue curve is a Lorentzian fit to the central peak, yielding a FWHM linewidth of 2 Hz. The data was recorded using a spectrum analyzer with a sweep time of 200 s at a RBW of 1 Hz.

3.3. Compensation of the resonator drifts and frequency stability of the idler wave on long time intervals

As mentioned above, we actively compensate for both resonators' slow drifts. In the case of resonator 1, this is done in order to keep the idler frequency at a fixed absolute value, which is necessary for ultra-high precision spectroscopy. In the case of resonator 2, the OFC2 comb lines are kept at fixed values.

The drifts of resonator 1 and 2 are compensated independently and at a different stage of the optical setup. For laser L1, and consequently for OFC1, the resonator drift is not compensated. Instead, the LO frequency of the PLL of the idler to OFC1 is corrected; therefore, only the OPO's idler frequency will maintain a fixed absolute value. For resonator 2, the compensation is instead implemented via the EOM shown in the bottom unit in Fig. 2. Therefore, both the L2 output frequency (after the AOM) and the entire OFC2 are drift-compensated.

For both units, the compensation is implemented in a similar manner: the drift of each resonator is calculated from the absolute frequency value measured by each comb every 1 s relative to the H-maser. A moving average of the frequency data is computed and compared to a target frequency. The deviation of this average from the target is the error signal delivered to a digital PID loop that acts on the LO frequency or on the EOM frequency, respectively, for OPO and L2. Averaging times of 30 s for resonator 1 and 20 s for resonator 2 were found to lead to the best performance.

As a consequence of the two drift compensations, the idler frequency instability on long timescales shown in Fig. 5 (red) has to be interpreted in the following way. Since both of our combs measure the absolute frequency of the lasers relative to the H-maser frequency, the drift compensations described above effectively reference the idler's second-harmonic and the reference laser L2 (and thus also OFC2) to the H-maser. Since all RF devices used to record the shown data are also referenced to this H-maser, we are effectively measuring one maser-referenced frequency against another. Therefore, the instability averages down as the integration time increases.

Determining the absolute value of the optical frequency relative to the atomic unit of frequency (SI-traceability) requires that we continuously compare our H-maser frequency to a H-maser of PTB that is steered to the international atomic time. Our comparison occurs via common-view
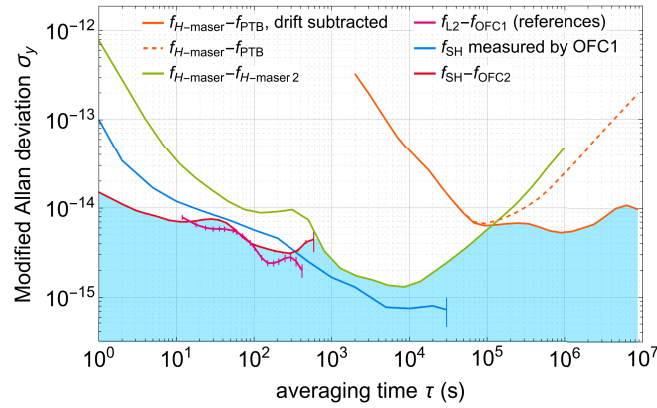
Fig. 5. Fractional Allan deviations of different signals. The magenta, blue and red traces show Allan deviations of an optical frequency. For magenta and red, the underlying data is the beat frequency between two waves, while for the blue trace it is the data calculated from Eq. (2), with f_{ceo1}, f_{rep1} and f_{beat1} measured simultaneously. All RF frequencies are either measured by a frequency counter or a spectrum analyzer, both of which are referenced to the H-maser. The green and orange traces show Allan deviations of the H-maser, evaluated by different methods. The upper limit of the blue shaded area depicts a conservative estimate of the fractional instability of the OPO's idler wave, inferred from the individual measurements. See text for explanations.

GNSS. The comparison determines the frequency offset of our H-maser's nominal 10 MHz signal and also the time drift of the offset. With this information, we can finally compute the lasers' absolute frequencies and their instabilities relative to the atomic frequency standard.

To demonstrate that our system is stabilized over long time intervals and to summarize the performance, we show in Fig. 5 six different fractional modified Allan deviations σ_y.

The dashed orange trace is the instability of the comparison of the frequency of our H-maser and the international atomic frequency standard at PTB. The upturn after approximately 1 day is due to the drift of the maser. The time-varying offset of our maser is recorded and taken into account in the OPO frequency data analysis in post-processing or in a feed-forward correction. The fractional drift rate is approximately 3×10^{-15} per day for this H-maser. The full orange line is obtained by removing the linear drift from the measured data and re-evaluating the Allan deviation. Since the GNSS receiver provides one reading every 15 min, no Allan deviation can be determined for short integration times.

The green trace is the Allan deviation of a comparison of the H-maser with a similar device, recorded at a different time. The Allan deviation reflects the combined instability of the two masers. Since both are nominally equal, the instability of the maser used in the OPO stabilization is expected to be slightly less than the values of the trace. This trace extends to integration times shorter than 15 min. The low instability verified on such shorter timescales is an important feature, since the drift compensation described above relies on locking the lasers' frequencies to the maser with time constants on the order of $10^1 - 10^2$ s.

The magenta trace shows the Allan deviation of the drift-removed beat $f_{L2} - f_{OFC1}$. This is the relative instability of the two independent reference lasers. Note that OFC1 is not drift-compensated, so that similar to the maser data, a linear function was fitted to the raw beat data and subtracted from it, before computing the Allan deviation.

Finally, the red and blue traces refer to the Allan deviation of f_{SH}, and are obtained by two different methods. The first trace (blue) is the absolute frequency value f_{SH} determined by OFC1. This is achieved through the classic frequency comb equation for a to-be-determined optical

frequency f_o

$$f_o = f_{ceo1} + n f_{rep1} + f_{beat1}, \qquad (2)$$

where $f_{ceo1} = 35.600\,000\,00(1)$ MHz for OFC1, n is the index of the comb mode used for locking and determined using the wavelength meter, and $f_{beat1} = f_{SH} - f_{OFC1}$ is the beat frequency between the SH of the idler and the closest mode of OFC1. Under phase-lock, f_{beat1} is equal to the local oscillator's frequency, typically in the range of $40 - 100$ MHz. The repetition rate $f_{rep1} \simeq 250$ MHz is here measured once per second by a high-resolution frequency counter (Microsemi 3120A) referenced to the H-maser. The blue trace for f_{SH} averages down with increasing integration time. These Allan deviation values do not reflect the actual (absolute) instability of the idler frequency, but indicate that it is locked well to the OFC1 on the short time scale and to the H-maser on the long time scale.

The second trace for f_{SH} (red) is the normalized Allan deviation $\sigma_y(f_{SH} - f_{OFC2})$. Here, the data was recorded with another frequency counter, also with 1 s integration time. In this measurement, and for short averaging times, the Allan deviation results from the independent frequency fluctuations of the idler SH wave and the OFC2 comb mode. Thus, the plotted red values represent an upper bound for the instability of the idler SH wave. This bound is $\sigma_y(f_{SH}) \leq 1 \times 10^{-14}$ and applies also to the idler frequency itself. The red trace is not extended to longer integration times because it then no longer reflects the actual instability of the idler frequency. As explained, f_{SH} and f_{OFC2} are not independent on long timescales.

3.4. Absolute frequency comparison

The two employed combs OFC1, OFC2 may be used not only to characterize the instability of the system, but also to compare and verify that the same absolute frequency is measured by both combs and associated equipment. The task is accomplished by measurements similar to those presented in sections 3.1 and 3.3. Equation (2) is now applied to the two independent combs, and (f_{ceo}, f_{rep}) are measured by independent frequency counters, n is calibrated using a common wavelength meter, and the two beat frequencies f_{beat1}, f_{beat2} are measured with a spectrum analyzer and a frequency counter for OFC1 and OFC2, respectively. All counters and the spectrum analyzer are referenced to the common H-maser. Thus, in this characterization we focus on the optical metrology, and not on the performance of the RF reference. In a variation to the previous sections, the data in this context was taken for an idler SH wavelength of $1.20\,\mu$m. Additionally, a different reference laser L3 and ULE resonator, at $1.53\,\mu$m, were used to stabilize OFC1. We confirmed that the stabilized laser L3 had a similar level of frequency instability as the laser L1 used in the above sections, by characterizing it in a similar manner as is described for the comparison of L1 and L2 in sections 3.1 and 3.3.

The result is shown in Fig. 6. The data underlying the figure was taken simultaneously with the two combs and spans a duration of 2330 s. The raw f_{SH} data were averaged with different averaging times, and the mean of the averaged values is displayed in the figure. The statistical error associated with the points is the standard error of the means. The frequency counter used to count f_{rep} with OFC2 has a lower precision than the counter for OFC1, causing the larger statistical uncertainty, particularly apparent for small averaging times. The systematic uncertainty is given by the combined inaccuracy of the RF devices used in both measurements. The dominant contribution is from the spectrum analyzer used in the OFC1 measurement, which contributes 1.2 Hz uncertainty. All other contributions are on the order of a few millihertz or smaller. We found that for all averaging times, the two frequency values obtained with the two measurement systems based on OFC1 and OFC2 agree within the combined uncertainty. For the longest averaging time $\tau = 500$ s, the difference between the two measured values is $\langle (f_{SH,OFC1})_\tau \rangle - \langle (f_{SH,OFC2})_\tau \rangle = (0.2 \pm 1.4)$ Hz, or $(0 \pm 6) \times 10^{-15}$ fractionally. Thus, 6×10^{-15} is a conservative estimate for the total fractional uncertainty of the idler frequency measurement

procedure by a single comb, excluding the uncertainty of the RF reference. (The latter is estimated to be at a similar level.)
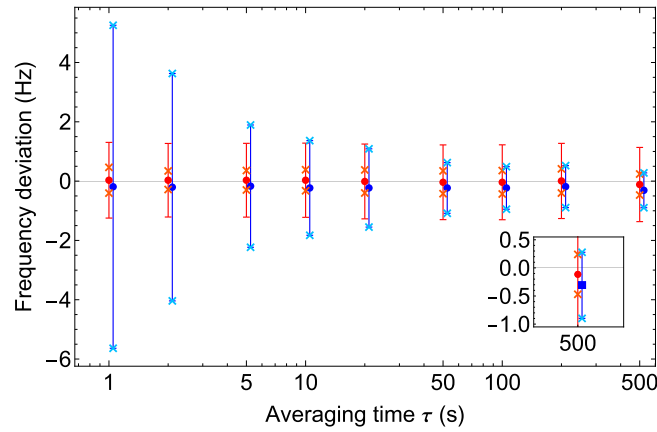

Fig. 6. The optical frequencies f_{SH} measured with OFC1 (red) and with OFC2 (blue), for different averaging times. The data are shown relative to an (arbitrary) offset frequency (approximately 249 THz). Two error bars are shown for each data set. The crosses represent the statistical standard error of the measurement, while the error bars denote the combination of statistical errors and systematic uncertainties. For clarity, the blue data points and errors are shown with a horizontal offset.

3.5. Stabilization of different idler wavelengths

As mentioned, the idler SHG sub-unit has been implemented in a way that it is capable of generating the second-harmonic wave over the entire tuning range of the idler. When changing the idler wavelength, it is necessary to change either the SHG crystal temperature, the grating period through which the laser wave propagates, or a combination of both. The crystal temperature is controlled by a commercial oven and an oven controller unit, obtained together with the crystal. We mounted the oven on a translation stage to allow for a fine adjustment of the crystal position perpendicular to the laser propagation direction. With this setup, a temperature change is possible within a few minutes, while a change of the grating period takes approximately thirty minutes due to the need for minor alignment optimization.

Therefore, the actual limiting factor of our method is the output range of the comb. For our OFC1, it is $1.0 - 1.6\,\mu$m, thus limiting the overall system's operation to the range $2.2 - 3.2\,\mu$m. Note that this could be extended by using OFC2 instead as the reference for the OPO, since it has a larger wavelength range than OFC1, reaching up to $2.0\,\mu$m. This potential exchange should not have a significant effect on the stability of the OPO, since both combs possess similar performance. For this reason, we believe that the full idler range of our OPO is lockable using our method.

We have phase-locked the OPO when tuned to the wavelengths 2.40, 2.60, 2.70, 2.81 μm, corresponding to 1.20, 1.30, 1.35, 1.40 μm for the SH. In all cases, we observed phase noise spectra and linewidths of the PLL similar to those shown in Fig. 3. These are provided as a supplemental document (see Supplement 1). We thus infer a similar level of idler frequency instability for these cases. For the specific cases of 2.40 μm and 2.60 μm, we have verified the performance by a beat with OFC2/L2, in the same way as was done for 2.80 μm, see sections 3.1 and 3.3. Therefore, we believe that our scheme will work well at any idler wavelength (even untested ones) and will provide similar frequency stability as the one presented above.

3.6. Long-term operation of the system

For providing long-term stability of the idler, we rely on the following procedure. After a thermalization of the setup, the range of the OPO's fast lock is sufficient to maintain the lock for a few hours. During operation, the SH frequency is measured by the wavelength meter, denoted f_{WM}. Due to an imperfect calibration of the wavelength meter, the value f_{WM} is offset from the correct value measured by the comb, by an amount $\Delta f_{WM} = f_{WM} - f_{SH,OFC1}$, typically $10 - 30\,\mathrm{MHz}$. Therefore, while the OPO is in the locked state, Δf_{WM} is calibrated. When the OPO falls out of lock, f_{WM} will change. A digital control loop then pushes the frequency back to the calibrated offset, with feedback applied to the pump laser's piezo actuator. When the frequency is close to the lock point, the fast lock automatically re-engages, restoring the locked state. This procedure effectively re-centers the fast lock output and typically takes a few seconds.

We show in Fig. 7 f_{WM} over the course of a day. In the locked state, the idler accurately maintained the same target frequency, as confirmed by the continuous measurement with OFC1. Occasionally, wavelength jumps were detected by the wavelength meter. These are situations, where the OPO fell out of phase-lock and was quickly re-locked by the digital loop described above. The jumps are a result of the thermal drift of the OPO, which in our current setup is not compensated for by a slow lock, e.g. by controlling the piezo actuator of the pump laser.
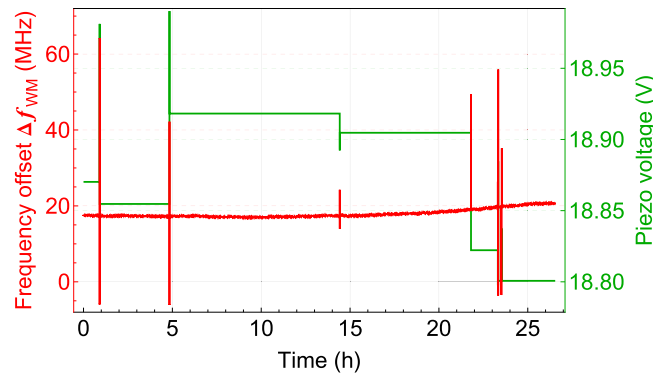
Fig. 7. Long-term stability of the system during of a typical measurement day. The red trace shows the wavelength of the idler's second harmonic measured by the wavelength meter (converted to frequency) relative to the value measured by OFC1. The nearly constant trace shows that the OPO was operating in the locked state nearly all the time. The offset ($\Delta f_{WM} \simeq 18\,\mathrm{MHz}$) and its drift (3 MHz over 1 day) are systematic errors of the wavelength meter, consistent with its specifications. The green trace shows the voltage applied to the piezo actuator of the pump laser, which is used to re-lock the OPO. Jumps in the recorded wavelength meter reading correspond to instants when the OPO fell out of phase-lock and was subsequently automatically re-locked by changing the piezo actuator voltage. Typically, the out-of-lock periods lasted a few seconds.

The total unlocked time in Fig. 7 (67 s) relative to the measurement interval of 26 h corresponds to a duty cycle of 99.93 %. Importantly, we have operated the system in this configuration at multiple wavelengths daily over the course of more than two years, proving the stability and robustness of the setup. No major flaws or issues arose during this time.

4. Conclusion, application, and perspectives

We have developed an optical frequency metrology system based on an optical-parametric-oscillator. It exhibits a fractional frequency instability at the 1×10^{-14} level or smaller for integration times between 1 and 10^5 s and a linewidth of similar magnitude. Both of these

properties represent more than a hundredfold improvement over the previous state-of-the-art [20,45]. Our scheme was employed at several wavelengths within the idler range, proving the flexibility of the method. Additionally, the system has been operated long-term with a duty cycle above 99.9 %. The idler frequency is SI-traceable through a hydrogen-maser-referenced optical frequency comb that is continuously calibrated to the national standard via common-view GNSS. The total uncertainty of the idler frequency measurement relative to the RF reference is less than 6×10^{-15} and the RF frequency accuracy is approximately 1×10^{-14}, resulting in a total uncertainty of less than 1.2×10^{-14}. The system has been thoroughly analyzed and sources of noise have been identified. We find that the performance of the system is limited by the instability of the reference lasers and of the H-maser, as well as by fiber noise. In principle, these limits could be overcome by implementing a more stable reference laser [52,53], an optical fiber link to a national metrology laboratory [54–56], and active fiber noise cancellation [57], all of which have been demonstrated elsewhere.

In separate work, this system enabled the first Doppler-free spectroscopy of electric quadrupole vibrational transitions in a molecular ion, and furthermore permitted a SI-referenced measurement of their frequencies. Owing to the exceptional stability of the idler frequency, frequency scan step sizes as small as 5 Hz could be taken. This enabled measurements of spectroscopic lines with linewidths as small as $\simeq 6$ Hz, corresponding to line quality factors of up to 2.2×10^{13} [25,58]. This application example provides a separate confirmation of the results presented here. We have thus realized a powerful tool for mid-infrared precision spectroscopy, in particular when high power is required.

Based on the present work, we expect that the system can be expanded to alternatively stabilize the OPO's signal wave frequency (1.45 - 2.07 μm) to a similar stability level as shown here for the idler wave. Most of the wavelength range of the signal can be beaten directly with OFC2. A SHG unit is thus not required to bridge to the NIR regime, which simplifies the setup. However, the locking scheme employed here does not work for the signal wave, due to the OPO's cavity being resonant for the latter. Instead, we propose to implement a feedback control scheme using an AOM in the output path of the signal wave, which will act as a fast frequency shifter. A down-stream beat with the OFC would enable both the generation of an error signal for a PLL with feedback applied to the AOM as well as an absolute frequency measurement. Note that long-term stability requires the absence of mode-hops. The mode-hop free tuning range of the signal radiation is on the order of 10^2 MHz, which is similar in magnitude to its drift over a few hours (inferred from the observation of the idler drift, see Sec. 2). Therefore, we expect that long-term stability can be achieved by incorporating a slow servo that controls the OPO cavity length. Note that in this case, the idler locking scheme does not need to be operated and that the pump and idler radiations remain unaffected since the AOM frequency shift is applied once the signal radiation has left the OPO. With such a scheme, it should be possible to extend the output spectral range of the metrology system to include 1.45 - 2.07 μm.

Longer wavelengths than those presented in this work should also be realizable as an extension of our setup, as follows. With the use of an additional laser source in the NIR range, e.g. an amplified fiber laser at 1.5 μm, phase-locked to the same OFC, and a suitable crystal that allows for difference-frequency generation (DFG), the generation of cw radiation up to $\simeq 8$ μm is straightforward [59,60]. The 1.5 μm radiation can be mixed with either the frequency-stable idler wave or the frequency-stable signal wave, resulting in far-IR radiation with frequency stability expected to be similar to that presented here for the idler.

Supplemental document. See Supplement 1 for supporting content.

References

1. S. T. Yang, R. C. Eckardt, and R. L. Byer, "Continuous-wave singly resonant optical parametric oscillator pumped by a single-frequency resonantly doubled Nd:YAG laser," Opt. Lett. **18**(12), 971–973 (1993).
2. W. R. Bosenberg, A. Drobshoff, J. I. Alexander, *et al.*, "93% pump depletion, 3.5-W continuous-wave, singly resonant optical parametric oscillator," Opt. Lett. **21**(17), 1336–1338 (1996).
3. K. Schneider, P. Kramper, S. Schiller, *et al.*, "Toward an optical synthesizer: a single-frequency parametric oscillator using periodically poled LiNbO$_3$," Opt. Lett. **22**(17), 1293–1295 (1997).
4. S. Schiller and J. Mlynek, "Continuous-wave optical parametric oscillators," Appl. Phys. B **66**(6), 661–764 (1998). Special Issue, Editors: S. Schiller, J. Mlynek.
5. D. J. M. Stothard, M. Ebrahimzadeh, and M. H. Dunn, "Low-pump-threshold continuous-wave singly resonant optical parametric oscillator," Opt. Lett. **23**(24), 1895–1897 (1998).
6. M. H. Dunn and M. Ebrahimzadeh, "Parametric Generation of Tunable Light from Continuous-Wave to Femtosecond Pulses," Science **286**(5444), 1513–1517 (1999).
7. D. Weise, U. Strößner, A. Peters, *et al.*, "Continuous-wave 532-nm-pumped singly resonant optical parametric oscillator with periodically poled KTiOPO$_4$," Opt. Commun. **184**(1-4), 329–333 (2000).
8. T. Petelski, R. S. Conroy, K. Bencheikh, *et al.*, "All-solid-state, tunable, single-frequency source of yellow light for high-resolution spectroscopy," Opt. Lett. **26**(13), 1013–1015 (2001).
9. E. V. Kovalchuk, D. Dekorsy, A. I. Lvovsky, *et al.*, "High-resolution Doppler-free molecular spectroscopy with a continuous-wave optical parametric oscillator," Opt. Lett. **26**(18), 1430–1432 (2001).
10. A. Hecker, M. Havenith, C. Braxmaier, *et al.*, "High resolution Doppler-free spectroscopy of molecular iodine using a continuous wave optical parametric oscillator," Opt. Commun. **218**(1-3), 131–134 (2003).
11. D. D. Arslanov, S. M. Cristescu, and F. J. M. Harren, "Optical parametric oscillator based off-axis integrated cavity output spectroscopy for rapid chemical sensing," Opt. Lett. **35**(19), 3300–3302 (2010).
12. M. Vainio, M. Merimaa, and L. Halonen, "Frequency-comb-referenced molecular spectroscopy in the mid-infrared region," Opt. Lett. **36**(21), 4122–4124 (2011).
13. S. Thorwirth, J. Krieg, V. Lutter, *et al.*, "High-resolution OPO spectroscopy of Si$_2$C$_3$ at 5μm: Observation of hot band transitions associated with ν_3," J. Mol. Spectrosc. **270**(1), 75–78 (2011).
14. I. Ricciardi, E. D. Tommasi, P. Maddaloni, *et al.*, "Frequency-comb-referenced singly-resonant OPO for sub-Doppler spectroscopy," Opt. Express **20**(8), 9178–9186 (2012).
15. D. Zhao, K. D. Doney, and H. Linnartz, "High-resolution infrared spectra of vibrationally excited HC$_4$H in a supersonic hydrocarbon plasma jet," J. Mol. Spectrosc. **296**, 1–8 (2014).
16. H. Chadwick, P. M. Hundt, M. van Reijzen, *et al.*, "Quantum state specific reactant preparation in a molecular beam by rapid adiabatic passage," J. Chem. Phys. **140**(3), 034321 (2014).
17. M. Vainio and L. Halonen, "Mid-infrared optical parametric oscillators and frequency combs for molecular spectroscopy," Phys. Chem. Chem. Phys. **18**(6), 4266–4294 (2016).
18. C. R. Markus, S. Thorwirth, O. Asvany, *et al.*, "High-resolution double resonance action spectroscopy in ion traps: vibrational and rotational fingerprints of CH$_2$NH$_2^+$," Phys. Chem. Chem. Phys. **21**(48), 26406–26412 (2019).
19. C. R. Markus and B. J. McCall, "Highly accurate experimentally determined energy levels of H$_3^+$," J. Chemical Phys. **150**(21), 214303 (2019).
20. Z.-T. Zhang, C.-F. Cheng, Y. R. Sun, *et al.*, "Cavity ring-down spectroscopy based on a comb-locked optical parametric oscillator source," Opt. Express **28**(19), 27600–27607 (2020).
21. D. Gupta, W. G. D. P. Silva, J. L. Doménech, *et al.*, "High-resolution rovibrational and rotational spectroscopy of the singly deuterated cyclopropenyl cation, c-C$_3$H$_2$D$^+$," Faraday Discuss. **245**, 298–308 (2023).
22. C. Wunderlich and C. Balzer, "Quantum measurements and new concepts for experiments with trapped ions," in *Advances in Atomic, Molecular, and Optical Physics* Vol. 49, (Academic Press, 2003), pp. 295–376.
23. S. Schiller, "Hydrogenlike Highly Charged Ions for Tests of the Time Independence of Fundamental Constants," Phys. Rev. Lett. **98**(18), 180801 (2007).
24. E. G. Myers, "CPT tests with the antihydrogen molecular ion," Phys. Rev. A **98**(1), 010101 (2018).
25. M. R. Schenkel, S. Alighanbari, and S. Schiller, "Laser spectroscopy of a rovibrational transition in the molecular hydrogen ion H$_2^+$," Nat. Phys. **20**(3), 383–388 (2024).
26. M. Niu, E. Salumbides, G. Dickenson, *et al.*, "Precision spectroscopy of the X$^1\Sigma_g^+$, $v = 0 \rightarrow 1(J = 0 - 2)$ rovibrational splittings in H$_2$, HD and D$_2$," J. Mol. Spectrosc. **300**, 44–54 (2014).
27. A. Fast and S. A. Meek, "Sub-ppb Measurement of a Fundamental Band Rovibrational Transition in HD," Phys. Rev. Lett. **125**(2), 023001 (2020).

28. A. Fast and S. A. Meek, "Precise measurement of the D_2 $S_1(0)$ vibrational transition frequency," Mol. Phys. **120**(19-20), e1999520 (2022).

29. H. Fleurbaey, A. O. Koroleva, S. Kassi, *et al.*, "The high-accuracy spectroscopy of H_2 rovibrational transitions in the (2-0) band near 1.2 μm," Phys. Chem. Chem. Phys. **25**(21), 14749–14756 (2023).

30. J. Komasa, "Energy levels of the hydrogen molecule from relativistic nonadiabatic calculations," in *International Conference on Precision Physics and Fundamental Physical Constants (FFK)*, (Vienna, Austria, 2023).

31. Q.-H. Liu, Y. Tan, C.-F. Cheng, *et al.*, "Precision spectroscopy of molecular hydrogen," Phys. Chem. Chem. Phys. **25**(41), 27914–27925 (2023).

32. K. Pachucki and J. Komasa, "Rovibrational levels of helium hydride ion," J. Chemical Phys. **137**(20), 204314 (2012).

33. M. Kajita and N. Kimura, "Prospect for Vibrational Transition Frequency Measurement of Rare-gas Hydride Ions," J. Phys. Soc. Jpn. **89**(11), 114301 (2020).

34. S. Schiller, D. Bakalov, and V. I. Korobov, "Simplest molecules as candidates for precise optical clocks," Phys. Rev. Lett. **113**(2), 023004 (2014).

35. J.-P. Karr, "H_2^+ and HD^+: candidates for a molecular clock," J. Mol. Spectrosc. **300**, 37–43 (2014).

36. M. Kajita, G. Gopakumar, M. Abe, *et al.*, "Test of m_p/m_e changes using vibrational transitions in N_2^+," Phys. Rev. A **89**(3), 032509 (2014).

37. F. Wolf, J. C. Heip, M. J. Zawierucha, *et al.*, "Prospect for precision quantum logic spectroscopy of vibrational overtone transitions in molecular oxygen ions," New J. Phys. **26**(1), 013028 (2024).

38. S. A. Diddams, D. J. Jones, L.-S. Ma, *et al.*, "Optical frequency measurement across a 104-THz gap with a femtosecond laser frequency comb," Opt. Lett. **25**(3), 186–188 (2000).

39. R. Holzwarth, T. Udem, T. W. Hänsch, *et al.*, "Optical Frequency Synthesizer for Precision Spectroscopy," Phys. Rev. Lett. **85**(11), 2264–2267 (2000).

40. H. Inaba, T. Ikegami, F.-L. Hong, *et al.*, "Phase locking of a continuous-wave optical parametric oscillator to an optical frequency comb for optical frequency synthesis," IEEE J. Quantum Electron. **40**(7), 929–936 (2004).

41. E. V. Kovalchuk, T. Schuldt, and A. Peters, "Combination of a continuous-wave optical parametric oscillator and a femtosecond frequency comb for optical frequency metrology," Opt. Lett. **30**(23), 3141–3143 (2005).

42. N. Poli, C. W. Oates, P. Gill, *et al.*, "Optical atomic clocks," Rivista del Nuovo Cimento **36**, 555 (2013).

43. A. D. Ludlow, M. M. Boyd, J. Ye, *et al.*, "Optical atomic clocks," Rev. Mod. Phys. **87**(2), 637–701 (2015).

44. J. Peltola, M. Vainio, T. Fordell, *et al.*, "Frequency-comb-referenced mid-infrared source for high-precision spectroscopy," Opt. Express **22**(26), 32429–32439 (2014).

45. I. Ricciardi, S. Mosca, M. Parisi, *et al.*, "Sub-kilohertz linewidth narrowing of a mid-infrared optical parametric oscillator idler frequency by direct cavity stabilization," Opt. Lett. **40**(20), 4743–4746 (2015).

46. J. Karhu, M. Vainio, M. Metsälä, *et al.*, "Frequency comb assisted two-photon vibrational spectroscopy," Opt. Express **25**(5), 4688–4699 (2017).

47. D. B. Foote, M. J. Cich, W. C. Hurlbut, *et al.*, "High-resolution, broadly-tunable mid-IR spectroscopy using a continuous wave optical parametric oscillator," Opt. Express **29**(4), 5295–5303 (2021).

48. C. J. Kwong, M. G. Hansen, J. Sugawara, *et al.*, "Characterization of the long-term dimensional stability of a NEXCERA block using the optical resonator technique," Meas. Sci. Technol. **29**(7), 075011 (2018).

49. I. Ito, A. Silva, T. Nakamura, *et al.*, "Stable CW laser based on low thermal expansion ceramic cavity with 4.9 mHz/s frequency drift," Opt. Express **25**(21), 26020–26028 (2017).

50. J. I. Thorpe, K. Numata, and J. Livas, "Laser frequency stabilization and control through offset sideband locking to optical cavities," Opt. Express **16**(20), 15980–15990 (2008).

51. A. Y. Nevsky, S. Alighanbari, Q. Chen, *et al.*, "Robust frequency stabilization of multiple spectroscopy lasers with large and tunable offset frequencies," Opt. Lett. **38**(22), 4903 (2013).

52. S. Häfner, S. Falke, C. Grebing, *et al.*, "8×10^{-17} fractional laser frequency instability with a long room-temperature cavity," Opt. Lett. **40**(9), 2112–2115 (2015).

53. A. Didier, S. Ignatovich, E. Benkler, *et al.*, "946-nm Nd:YAG digital-locked laser at 1.1×10^{-16} in 1 s and transfer-locked to a cryogenic silicon cavity," Opt. Lett. **44**(7), 1781–1784 (2019).

54. K. Predehl, G. Grosche, S. M. F. Raupach, *et al.*, "A 920-kilometer optical fiber link for frequency metrology at the 19th decimal place," Science **336**(6080), 441–444 (2012).

55. D. Husmann, L.-G. Bernier, M. Bertrand, *et al.*, "SI-traceable frequency dissemination at 1572.06 nm in a stabilized fiber network with ring topology," Opt. Express **29**(16), 24592–24605 (2021).

56. C. Clivati, M. Pizzocaro, E. Bertacco, *et al.*, "Coherent Optical-Fiber Link Across Italy and France," Phys. Rev. Appl. **18**(5), 054009 (2022).

57. L.-S. Ma, P. Jungner, J. Ye, *et al.*, "Delivering the same optical frequency at two places: accurate cancellation of phase noise introduced by an optical fiber or other time-varying path," Opt. Lett. **19**(21), 1777–1779 (1994).

58. S. Alighanbari, M. R. Schenkel, S. Schiller, *et al.*, subm.

59. S. Vasilyev, S. Schiller, A. Nevsky, *et al.*, "Broadly tunable single-frequency cw mid-infrared source with milliwatt-level output based on difference-frequency generation in orientation-patterned GaAs," Opt. Lett. **33**(13), 1413–1415 (2008).

60. K. Devi, P. G. Schunemann, and M. Ebrahim-Zadeh, "Continuous-wave, multimilliwatt, mid-infrared source tunable across 6.4-7.5μm based on orientation-patterned GaAs," Opt. Lett. **39**(23), 6751–6754 (2014).

5.2. Laser spectroscopy of a rovibrational transition in the molecular hydrogen ion H$_2^+$

Copyright notice:

The contributions of the author of this thesis are detailed in the corresponding section of the manuscript on page 67.

Article

Laser spectroscopy of a rovibrational transition in the molecular hydrogen ion H_2^+

M. R. Schenkel ⓘ , S. Alighanbari ⓘ & S. Schiller ⓘ ✉

Comparison of precise predictions of the energy levels of the molecular hydrogen ion H_2^+—the simplest molecule—with measured vibrational transition frequencies would allow a direct determination of the proton-to-electron mass ratio and of the proton's charge radius. Here we report vibrational laser spectroscopy of trapped and sympathetically laser-cooled H_2^+, which represents a step towards this goal. We studied a first-overtone electric-quadrupole transition and measured its two hyperfine components. The determined spin-averaged vibrational transition frequency has a fractional uncertainty of 1.2×10^{-8} and is in agreement with the theoretically predicted value. We measured an analogous electric-quadrupole transition in HD^+ to estimate systematic uncertainties. Here, we observed a vastly improved line quality factor compared to previous electric-quadrupole spectroscopy of molecular ions. Our work demonstrates that first-overtone electric-quadrupole transitions are suitable for precision spectroscopy of molecular ions, including H_2^+, and that determining the proton-to-electron mass ratio with laser spectroscopy could become competitive with mass spectrometry using Penning traps. Furthermore, achieving precision spectroscopy of H_2^+ is an essential prerequisite for a future test of combined charge, parity and time reversal symmetry based on a comparison with its antimatter counterpart.

In recent years, it has been shown that the accurate determination of transition frequencies between rovibrational levels of molecular ions can contribute to current endeavours in fundamental physics. In particular, precision rotational and vibrational spectroscopy of the molecular hydrogen ion (MHI) HD^+ has allowed testing some predictions of quantum electrodynamics theory[1], determining a fundamental constant and searching for physics beyond the standard model[2–5]. For a discussion, see refs. [5–7]. The heteronuclear HD^+ system is advantageous from an experimental point of view because it allows for electric-dipole (E1) transitions. Such transitions can be driven by moderate laser power. Also, any vibrational excitation decays on a timescale of tens of milliseconds to the ground vibrational level $v = 0$ by spontaneous emission (v is the vibrational quantum number). After thermalization with black-body radiation, an ensemble of HD^+ contains a sufficiently large fraction of molecules in any of a small set of rovibrational levels ($v = 0$, $N = 0, 1, 2, 3, 4$, where N is the rotational quantum number), a

favourable situation. However, HD^+ also has shortcomings. First, it has a complex hyperfine structure (HFS), complicating experimentation and extraction of the spin-averaged (HFS-free) frequency, and second, the key properties of its two dissimilar nuclei, namely the mass and charge radius, cannot be independently deduced from spectroscopic data.

To overcome the latter, intrinsic limitation, there is a need to investigate at least one of the homonuclear MHIs, H_2^+ and D_2^+. Due to the smaller spin of the proton (1/2) compared to the deuteron (1), the HFS of H_2^+ is simpler and this molecule may be preferred. In homonuclear diatomics, E1 transitions between rovibrational levels in the same electronic state are forbidden. As a consequence, the natural lifetimes of excited vibrational levels are extremely long, of the order of 1 week for H_2^+ (ref. [8]). Thus, homonuclear MHIs lack a natural vibrational state preparation: they do not readily decay to the vibrational ground state. Conversely, the natural linewidths of transitions between these levels are extremely small. This leads to the exciting perspective of

Institut für Experimentalphysik, Heinrich-Heine-Universität Düsseldorf, Düsseldorf, Germany. ✉e-mail: step.schiller@hhu.de
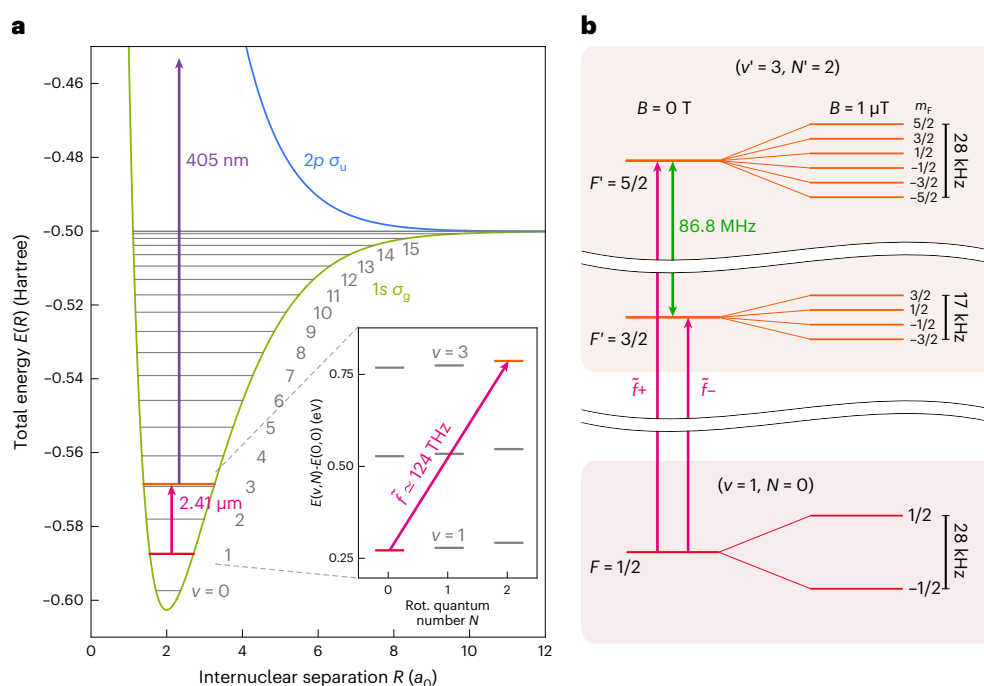
Fig. 1 | Energy levels of H_2^+ and transitions relevant to this work. a, H_2^+ molecular energy as a function of proton separation R in units of the Bohr radius a_0 for the two energetically lowest electronic states $1s\,\sigma_g$ and $2p\,\sigma_u$. The indicated vibrational energy levels (grey) are those for $N = 0$. The inset shows the first three rotational (Rot.) levels of the vibrational states $v = 1$–3. The studied transition $(v = 1, N = 0) \rightarrow (v' = 3, N' = 2)$ is shown by the magenta arrows. The dissociation laser's photon energy is indicated by the purple arrow. **b**, Hyperfine and Zeeman structure of the two rovibrational levels pertinent to the present study. The electron-spin-rotation coupling splits the upper vibrational level into two states $F' = 3/2$ and $5/2$, separated by 86.8 MHz (green arrow). The magenta arrows indicate the measured hyperfine components $\tilde{f}_+$ and $\tilde{f}_-$. The Zeeman splittings in a finite magnetic field $B = 1\,\mu T$ are shown for illustration. During the exposure of the molecules to the spectroscopy wave, the magnetic field was substantially smaller. To show the Zeeman splittings, the vertical axis is broken at two positions. F is the total angular momentum of the molecule and m_F is the total angular momentum projection quantum number.

spectroscopy with extremely high line resolution, limited only by the spectral purity of the laser. Such performance would be important for implementing fundamental tests of physics, for which the highest frequency accuracy is desirable[9].

Furthermore, rovibrational transitions must be induced by two-photon[10] or electric-quadrupole (E2) excitation[11,12]. The squared Rabi frequency for E2 excitation in a homonuclear MHI is substantially smaller than for the E1 excitation of a comparable transition in a heteronuclear MHI (Methods), posing a challenge due to the requirement for high laser intensities. Note that E1 transitions in homonuclear MHI do exist because of the presence of spin interactions, but the transition strengths between low-lying vibrational levels are predicted to be orders of magnitude weaker than for E2 transitions[13].

Although H_2^+ has been investigated theoretically for almost a century[14,15], no direct measurements of the vibrational structure of H_2^+ near the bottom of the internuclear potential curve have ever been performed. A few spectroscopic studies of H_2^+ have addressed rovibrational states close to the dissociation limit of the electronic ground state. Two studies determined electronic transition frequencies, including rovibrational contributions, with 10^{-6}-level uncertainty[16,17]. A third study measured a pure rotational transition with 4×10^{-5} uncertainty[18]. An alternative approach of studying transitions in highly excited Rydberg states of neutral H_2 (refs. 19,20) yielded two rotational transitions with uncertainties $(3, 5) \times 10^{-7}$. There has been no improvement in accuracy or resolution since 1990.

E2 transitions in H_2^+, first discussed theoretically 70 years ago, have never been observed in absorption and have been observed only in spontaneous emission under extreme conditions[21]. In fact, there has so far been only a single study of E2 vibrational (laser) spectroscopy of molecular ions, on N_2^+ at 4.6 μm (ref. 22). Note that E2 spectroscopy of neutral H_2 is well developed[23–25], because these molecules are readily

available at high density and absorption spectroscopy can be performed at easily available near-infrared laser wavelengths.

In this work, we perform vibrational laser spectroscopy of H_2^+, achieving a tenfold higher fractional accuracy than any other hitherto measured transition frequency of this molecule. We also present a precision study of E2 spectroscopy in a molecular-ion system to determine systematic shifts and explore its potential.

HFS of H_2^+

The rovibrational H_2^+ transition addressed in this work is illustrated in Fig. 1a. H_2^+ exhibits a HFS in all rovibrational levels, except when $N = 0$ (N is the rotational quantum number). In homonuclear diatomics, the HFS is simplified because of the anti-symmetrization principle for fermions. The total nuclear spin I takes on even or zero values in levels of even or zero N, the so-called para-levels. Thus, para-H_2^+ (that is, $N = 0, 2, 4, ...$) has $I = 0$. This leads to a very simple hyperfine Hamiltonian, containing only the interaction between electron spin and molecular rotation, $c_e(v, N)\,\mathbf{S}_e \cdot \mathbf{N}$. Here, c_e is the coupling coefficient, $\mathbf{S}_e$ is the electron spin operator and $\mathbf{N}$ is the rotational angular momentum operator. In contrast to the vibrational structure, the HFS of H_2^+ was measured a long time ago and accurately in levels $v = 4$–8, with uncertainties at the 1.5 kHz level, using radio-frequency (RF) spectroscopy[26]. After a half-century-long development, ab initio theory was able to match the experimental uncertainty[27–32].

The E2 transition with the simplest HFS is between levels with $N = 0$ and $N' = 2$ (or vice versa). We, therefore, chose to study this case, selecting $v = 1$ and $v' = 3$, as shown in Fig. 1b. The total angular momentum of the lower spectroscopy level ($v = 1, N = 0$) is $F = 1/2$, and there is no hyperfine splitting. For the upper spectroscopy level ($v' = 3, N' = 2$), angular momentum coupling yields $F' = 3/2$ or $5/2$, and the level is split by the electron-spin-rotation interaction into two
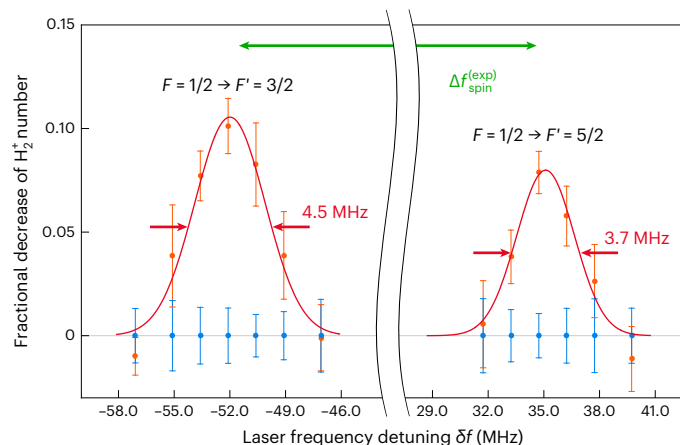
Fig. 2 | The two electron-spin-rotation components of the E2 rovibrational transition ($v = 1$, $N = 0$) → ($v' = 3$, $N' = 2$) in H_2^+. The laser frequency detuning δf is relative to the spin-averaged frequency $f_{\text{spin-avg}}^{(\text{theor})} \approx 124$ THz. The red curves are guides for the eye. The horizontal axis is broken. The error bars are estimated standard errors of the means. The frequency errors are not shown because they are at a level of 10 Hz. F and F' are the total angular momentum quantum numbers of the initial and final states, respectively. The green arrow indicates the splitting of the two hyperfine components $\Delta f_{\text{spin}}^{(\text{exp})}$. The measured linewidths (full-width at half-maximum) are shown as red arrows and labelled by their respective values.

non-degenerate states in absence of a magnetic field. One, therefore, expects two separate transitions: $\tilde{f}_-$: ($F = 1/2 \rightarrow F' = 3/2$) and $\tilde{f}_+$: ($F = 1/2 \rightarrow F' = 5/2$), since both satisfy the selection rules for E2 transitions.

Vibrational transition in H_2^+

To accomplish vibrational spectroscopy of H_2^+ and also obtain competitive accuracy, we trapped ensembles of molecules in a linear ion trap and sympathetically cooled them to millikelvin temperature using co-trapped laser-cooled beryllium ions[33]. An ensemble of H_2^+ was prepared from neutral para-H_2 gas leaked into the vacuum chamber and ionized by electron impact. This resulted in H_2^+ molecules being in a wide distribution of rovibrational levels[34]. Therefore, laser irradiation was applied to deplete the population in the upper spectroscopic level ($v' = 3$, $N' = 2$) and in rovibrational levels with equal or larger v. A spectroscopy beam with a wavelength of 2.4 µm was aligned to the trap's symmetry axis. Repeated cycles of H_2^+ loading, preparation and spectroscopic excitation followed by dissociation were required to accumulate sufficient data to give spectroscopic lines (Methods and Extended Data Fig. 1). Our spectroscopy protocol gave Doppler-limited resolution. The spectroscopy wave was produced by a continuous-wave optical parametric oscillator (OPO) that provides sufficient power to drive the E2 transition. To permit accurate frequency measurements at 2.4 µm, we developed an optical frequency metrology system (Methods).

Figure 2 shows the measured hyperfine components of the vibrational transition. The full linewidths of ~4 MHz are due to Doppler broadening (see below). The transition frequencies are

$$\tilde{f}_-^{(\text{exp})} = 124{,}486{,}979.9(2.3) \text{ MHz,}$$

$$\tilde{f}_+^{(\text{exp})} = 124{,}487{,}066.7(1.9) \text{ MHz.}$$

The lines exhibit low signal-to-noise ratios. We, therefore, assigned the line half-width at half-maxima as the statistical uncertainties of the frequencies.

Study of systematic effects

The systematic shifts of the H_2^+ transition could not be determined because the corresponding studies would have taken a prohibitively long time. The reason is the small fraction of molecules in the lower

spectroscopy state obtained in each loading and purification cycle, leading to a low data acquisition rate. This also precluded attempting to search for Doppler-free transitions. To circumvent this difficulty, we instead studied in detail an E2 transition of the related heteronuclear HD$^+$, for which a sufficient data acquisition rate can be realized. We took advantage of the above-mentioned spontaneous decay of the molecular ion to $v = 0$ levels after ionization of the HD precursor and additionally applied laser rotational cooling[35] to transfer approximately 75% of the ions into the single rovibrational level ($v = 0$, $N = 0$). We, therefore, chose to study the ($v = 0$, $N = 0$) → ($v' = 2$, $N' = 2$) first-overtone E2 transition at $\lambda_2 = 2.6$ µm using the same OPO system. The quadrupole transition matrix element is a factor 2 smaller than for the studied transition in H_2^+ (Methods). The spectroscopy beam was aligned perpendicular to the trap axis.

As Fig. 3 shows, we observed ultra-narrow, Doppler-free resonances, as we observed for the fundamental transition $v = 0 \rightarrow v' = 1$ (ref. 4) and for the fourth-overtone transition $v = 0 \rightarrow v' = 5$ (ref. 5). Linewidths as low as ~40 Hz, that is line resolutions of 2.7×10^{12}, were achieved. This is a fourfold improvement compared to the best MHI E1 transition result (6×10^{11}; ref. 5) and is comparable to a recent molecular E2 transition measurement of the neutral diatomic Sr$_2$, which had a line resolution of 2.9×10^{12} (ref. 36). Moreover, it is an improvement by a factor of ~10^6 compared to the only previous study of a molecular-ion E2 transition[22]. The observed linewidths are due to a combination of the natural linewidth (5 Hz; ref. 37), power-broadening, short exposure, as well as the linewidth and frequency instability of the spectroscopy laser.

Table 1 summarizes the characterized shifts. The transition frequencies measured under nominal conditions must be corrected by approximately −1.2 kHz or −1×10^{-11} fractionally. The uncertainty of the corrections is 1×10^{-12} fractionally for one component and twice as large for the other because of its larger linewidth. Light shifts might occur due to off-resonant E1 coupling of the two spectroscopy levels by the intense spectroscopy wave, but we did not observe such an effect and a theoretical estimate gives a shift consistent with the non-observation. The two studied stretched-state Zeeman components have equal and opposite, purely linear Zeeman shifts. Therefore, the $B = 0$ extrapolated frequency of the HFS component is the mean of the two corrected frequencies. It has an uncertainty of 0.12 kHz or 1×10^{-12} fractionally.

Turning to H_2^+, notice that the Zeeman shifts of individual Zeeman components of a rovibrational transition are different from those in HD$^+$ (ref. 38). In the absence of a direct measurement, we rely on a theoretical prediction[39]. The H_2^+ Zeeman shifts of the various components $|\Delta m_F| \leq 2$ of $\tilde{f}_+$ and $\tilde{f}_-$ are less than $|g_e \mu_B| \approx 28$ kHz µT^{-1} in magnitude (Methods and Extended Data Tables 1–3). During the H_2^+ spectroscopy intervals, we lowered the magnetic field to $|B| \leq 0.2$ µT, so that the shifts were negligible compared to the linewidths. Any light shift due to off-resonant coupling by the spectroscopy wave should be negligible in H_2^+ due to the vanishing E1 transition moments between rovibrational states (Methods).

In view of these considerations, we deduced that in the H_2^+ experiment, systematic shifts were not relevant compared to the measurement resolution of 2 MHz. We estimated that power-broadening is not relevant (Methods), so that we associated the observed linewidths with an H_2^+ ensemble temperature $T \approx 3.4$ mK. In separate experiments on strings of HD$^+$ ions, we found temperatures of ≈1.5 mK. The higher value observed here could be due to the larger number of trapped H_2^+, resulting in a three-dimensional rather than string-like arrangement and less efficient sympathetic cooling.

Comparison of experimental and theoretical results and the proton-to-electron mass ratio

The spin-rotation coefficient was deduced to be $c_e(v' = 3, N' = 2) = 2(\tilde{f}_+ - \tilde{f}_-)/5 = 34.8(1.2)$ MHz, which is consistent with the most accurate theoretical prediction $c_e^{(\text{theor})}(v' = 3, N' = 2) = 34.73025(12)$ MHz (ref. 32).
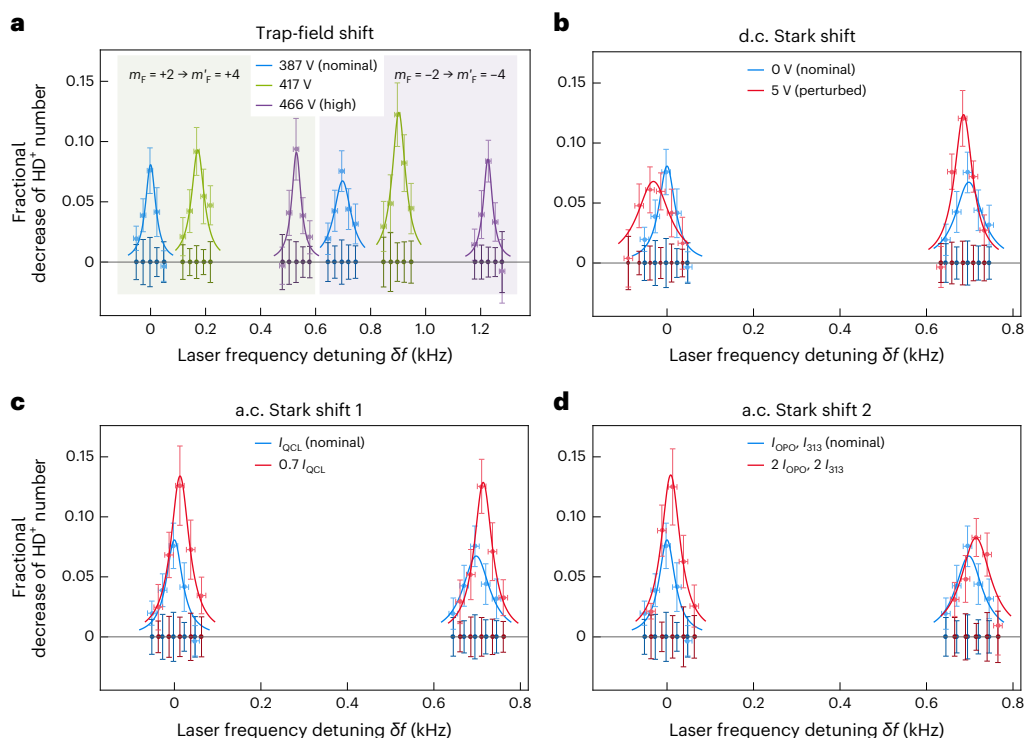
Fig. 3 | Two Zeeman components measured under different operating conditions. The two Zeeman components ($m_F = +2 \rightarrow m'_F = +4$) and ($m_F = -2 \rightarrow m'_F = -4$) of the hyperfine transition ($v = 0, N = 0, G_1 = 1, G_2 = 2, F = 2$) $\rightarrow$ ($v' = 2, N' = 2, G'_1 = 1, G'_2 = 2, F' = 4$) in HD$^+$, measured for a magnetic field strength of $B = 30$ μT. These are transitions between stretched spin states, that is states of maximum F and $|m_F|$. G_1 is the total spin of the proton–electron pair, and G_2 is the total particle spin, including also the deuteron. **a**, Each Zeeman component measured at trap-field amplitudes of 387, 417 and 466 V. The shaded regions group the same Zeeman component. **b**, Each Zeeman component measured at 0 and 5 V d.c. electric field. **c**, The a.c. Stark shift due to the quantum cascade laser (QCL) used for rotational cooling (Methods, 'HD$^+$ spectroscopy procedures') is studied by measuring the transitions at full (I_{QCL}) and 70%

intensity. **d**, The a.c. Stark shift induced by the spectroscopy source and the cooling laser together, measured at nominal intensities (I_{OPO} and I_{313}, respectively) and doubled intensities. The lines measured under nominal conditions (blue points and blue curves) were measured once and are reproduced in each panel for illustration. The other points and corresponding curves in different colours are the lines measured under various conditions. The laser frequency detuning δf is relative to the optical frequency of the $m_F = +2 \rightarrow m'_F = +4$ component measured under nominal conditions. The coloured curves are guides for the eye. For display purposes, the data are divided into 25-Hz-wide bins and the average value of each bin is shown. The vertical error bars are standard error of the mean in the bin. The horizontal error bars are the frequency uncertainty of the spectroscopy laser stemming from its linewidth (Methods).

Our spin-averaged frequency is $f^{(exp)}_{spin-avg} = (3\tilde{f}_+ + 2\tilde{f}_-)/5 = 124,487,032.7(1.5)$ MHz. This is a directly measured vibrational frequency in H$_2^+$. Remarkably, our value improves on the previous measurements of such a frequency by several orders of magnitude. The most accurate (indirect) measurement was performed by G. Herzberg and his team over half a century ago[40], using Rydberg series spectroscopy of neutral H$_2$ to obtain the first-overtone vibrational frequency with 7×10^{-5} uncertainty. With a fractional uncertainty of 1.2×10^{-8}, our value $f^{(exp)}_{spin-avg}$ is now the most accurately measured property of H$_2^+$, including the HFS[26,41]. Note that the experimental uncertainty was too large to allow us to identify the presence or absence of a recoil shift (17.1 kHz).

The ab initio value for the frequency is $f^{(theor)}_{spin-avg} = 124,487,032.45(6)$ MHz (Methods). The experimental and theoretical values agree.

The ab initio value requires as input the proton-to-electron mass ratio. This was taken from CODATA 2018. Instead, we can treat the mass ratio as an adjustable parameter in order to match the experiment with ab initio prediction, and obtain (Methods)

$$m_p/m_e = 1,836.152665(53).$$

The fractional uncertainty of this spectroscopically determined value (2.9×10^{-8}) is comparable to that which might be obtained from a comparison of experimental and theoretical results for the analogous transition in neutral H$_2$ (refs. 23,24). Note that the theoretical

uncertainty of that transition[25] is twice as large as that quoted in refs. 23,24.

Outlook

A near-term goal of H$_2^+$ spectroscopy is to achieve a transition frequency uncertainty $u_{goal} = u_r(f^{(exp)}_{spin-avg}) \approx 2 \times 10^{-12}$, four times smaller than today's uncertainty for the quantum electrodynamics calculations (8×10^{-12}; ref. 1). This would lead to a theory-limited mass ratio uncertainty $u_r(m_p/m_e) \approx 1.8 \times 10^{-11}$. The present result obtained for an E2 transition of HD$^+$ indicates that the goal is realistic, provided that the Zeeman shifts can be controlled sufficiently well. For the present (or analogous) rovibrational transition, we have identified a suitable scheme (Extended Data Table 3). Four Zeeman components whose frequencies have pairwise opposite linear Zeeman shifts and tiny quadratic shifts can be combined to yield the spin-averaged frequency. The goal uncertainty u_{goal} is reached if each Zeeman component is measured with $u_r(f) \le 4 \times 10^{-12}$ (0.5 kHz) total uncertainty. This requires a magnetic field stability $\delta B \approx 5 \times 10^{-2}$ μT (Methods), which is fulfilled with our apparatus. In the future, to achieve ultrahigh accuracy (10^{-16}-level uncertainty) in an RF trap, it appears more favourable to use a ($v, N = 2$) $\rightarrow$ ($v', N' = 2$) transition[42–45].

We briefly turn to the implications of this work for future vibrational spectroscopy of anti-H$_2^+$, which consists of two antiprotons bound by a positron and has never been observed. The spectroscopy would probe the charge and mass of the antiproton and of the positron as well as the antiproton–antiproton interaction and

Table 1 | Error budget of an E2 transition of HD⁺

Effect	$f^{(\text{exp})} - f^{(\text{exp,nom})}$ (kHz)	
	$m_F = +2 \rightarrow m_F' = +4$	$m_F = -2 \rightarrow m_F' = -4$
Statistics	0.00(2)	0.00(6)
Trap field	−1.18(10)	−1.18(16)
a.c. Stark (OPO and 313 nm laser)	0.01(3)	0.00(8)
a.c. Stark (5.5 μm laser)	0.03(4)	0.00(7)
d.c. Stark	0.00(3)	0.00(9)
Total	−1.14(12)	−1.19(22)

Measured systematic shifts and their uncertainties are given for two Zeeman components of one HFS component of the first-overtone transition ($v = 0, N = 0) \rightarrow (v' = 2, N' = 2)$ at 115 THz. $f^{(\text{exp})}$ is the extrapolated, unperturbed frequency. $f^{(\text{exp,nom})}$ is the frequency under standard operating conditions. Here, m_F (m_F') is the projection of the total angular momentum F (F') of the initial (final) state onto the direction of the static magnetic field. See Methods, 'Systematics of the HD⁺ E2 transition', for a detailed discussion of these effects.

positron–antiproton interaction. A charge, parity and time reversal symmetry (CPT) test would compare the vibrational frequency of anti-H_2^+ with its matter counterpart. Such a test is attractive because (1) a potential ultrahigh accuracy (10^{-17} fractional uncertainty) may be reached, presumably exceeding the potential future performance of antiprotonic helium spectroscopy[46] and of antiproton mass spectrometry[47], (2) it also involves the antiproton–antiproton interaction, which does not occur in other accessible antiparticle-containing systems, and (3) it has a much higher sensitivity to the antiproton mass compared to anti-hydrogen, for which it is only a reduced-mass effect. Both anti-H_2^+ spectroscopy proposals[48,49] have considered E2 transitions and the non-destructive read-out of the internal molecular state in a cryogenic trap. Future anti-H_2^+ production methods[50] and established non-destructive interrogation methods may favour the use of Penning traps, which are already used for studying antiprotons. Note that vibrational transitions have Zeeman components that have particularly small and opposite linear Zeeman shifts in the strong magnetic field of a Penning trap (Methods), so that the corresponding uncertainties would be negligible, even during long-term measurements.

A CPT test can be extended to a local position invariance test by performing the anti-H_2^+ versus H_2^+ comparison over the course of a year, as the Earth moves around the Sun and probes a varying solar gravitational potential. Such a test would be similar to a local position invariance test that compares the mass-to-charge ratios of an antiproton and a negatively charged hydrogen ion H⁻ (ref. 47) but would be more accurate and more encompassing, given the presence of the antiproton–antiproton interaction in anti-H_2^+.

The present results are an important step towards turning H_2^+ into a second member of the MHI family accessible to the metrology of fundamental constants and, eventually, also D_2^+. The simplicity of removing the HFS effects to obtain the spin-averaged frequency will be an important advantage. Since the studied E2 transitions in both H_2^+ and HD⁺ are not special cases, we believe that accurate E2 spectroscopy should be achievable with many homonuclear molecular-ion species. This underlines the potential of E2 spectroscopy of molecular ions aimed at testing for a possible time-variation of the electron-nuclear mass ratio[9,51,52].

Progress in H_2^+ and D_2^+ spectroscopy would be greatly facilitated if non-destructive internal state detection methods[53,54] and efficient state preparation that have been demonstrated for other species could be applied to these molecules. This will require measurements of single ions, which also promises higher accuracy. Concerning state preparation, spontaneous decay in a cryogenic Penning trap[21] and state-selective photoionization of H_2 (ref. 55) are demonstrated solutions. Recently, non-destructive, high-resolution electron-spin

resonance spectroscopy of a single HD⁺ molecule trapped for weeks in a Penning trap has been achieved[56], demonstrating both quantum-state identification and transition detection without molecule destruction. In an RF trap, the preparation of a single H_2^+ ion cooled by a single laser-cooled Be⁺ ion to the motional ground state was demonstrated[57]. Together with the present result for the feasibility of high-accuracy E2 spectroscopy, these milestones give support to proposals for developing a CPT/local position invariance test based on comparing the vibrational transition frequencies of H_2^+ and anti-H_2^+.

Online content

Any methods, additional references, Nature Portfolio reporting summaries, source data, extended data, supplementary information, acknowledgements, peer review information; details of author contributions and competing interests; and statements of data and code availability are available at https://doi.org/10.1038/s41567-023-02320-z.

References

1. Korobov, V. I. & Karr, J.-P. Rovibrational spin-averaged transitions in the hydrogen molecular ions. *Phys. Rev. A* **104**, 032806 (2021).
2. Alighanbari, S., Giri, G. S., Constantin, F. L., Korobov, V. I. & Schiller, S. Precise test of quantum electrodynamics and determination of fundamental constants with HD⁺ ions. *Nature* **581**, 152–158 (2020).
3. Patra, S. et al. Proton-electron mass ratio from laser spectroscopy of HD⁺ at the part-per-trillion level. *Science* **369**, 1238–1241 (2020).
4. Kortunov, I. V. et al. Proton-electron mass ratio by high-resolution optical spectroscopy of ion ensembles in the resolved-carrier regime. *Nat. Phys.* **17**, 569–573 (2021).
5. Alighanbari, S., Kortunov, I. V., Giri, G. S. & Schiller, S. Test of charged baryon interaction with high-resolution vibrational spectroscopy of molecular hydrogen ions. *Nat. Phys.* **19**, 1263–1269 (2023).
6. Schiller, S. Precision spectroscopy of molecular hydrogen ions: an introduction. *Contemp. Phys.* **63**, 247–279 (2022).
7. Karr, J.-P. & Koelemeij, J. C. J. Extraction of spin-averaged rovibrational transition frequencies in HD⁺ for the determination of fundamental constants. *Mol. Phys.* **121**, e2216081 (2023).
8. Bates, D. R. & Poots, G. Properties of the hydrogen molecular ion I: quadrupole transitions in the ground electronic state and dipole transitions of the isotopic ions. *Proc. Phys. Soc. Sect. A* **66**, 784–792 (1953).
9. Schiller, S. & Korobov, V. Test of time-dependence of the electron and nuclear masses with ultracold molecules. *Phys. Rev. A* **71**, 032505 (2005).
10. Karr, J.-P. et al. Vibrational spectroscopy of H_2^+: hyperfine structure of two-photon transitions. *Phys. Rev. A* **77**, 063410 (2008).
11. Korobov, V. I., Danev, P., Bakalov, D. & Schiller, S. Laser-stimulated electric quadrupole transitions in the molecular hydrogen ion H_2^+. *Phys. Rev. A* **97**, 032505 (2018).
12. Danev, P., Bakalov, D., Korobov, V. I. & Schiller, S. Hyperfine structure and electric quadrupole transitions in the deuterium molecular ion. *Phys. Rev. A* **103**, 012805 (2021).
13. Korobov, V. I. & Bakalov, D. Forbidden ortho–para electric dipole transitions in the H_2^+ ion. *Phys. Rev. A* **107**, 022812 (2023).
14. Burrau, Ø. Berechnung des Energiewertes des Wasserstoffmolekel-Ions (H_2^+) im Normalzustand. *Die Naturwiss.* **I.**, 16–17 (1927).
15. Teller, E. Über das Wasserstoffmolekülion. *Z. Phys.* **61**, 458–480 (1930).
16. Carrington, A. et al. Microwave electronic spectroscopy, electric field dissociation and photofragmentation of the H_2^+ ion. *J. Chem. Soc. Faraday Trans.* **89**, 603–614 (1993).

Article

17. Carrington, A., Leach, C. A. & Viant, M. R. Nuclear hyperfine structure in the electronic millimetre wave spectrum of H_2^+. *Chem. Phys. Lett.* **206**, 77–82 (1993).

18. Critchley, A. D. J., Hughes, A. N. & McNab, I. R. Direct measurement of a pure rotation transition in H_2^+. *Phys. Rev. Lett.* **86**, 1725–1728 (2001).

19. Arcuni, P. W., Fu, Z. W. & Lundeen, S. R. Energy difference between the (v=0, R=1) and the (v=0, R=3) states of H_2^+, measured with interseries microwave spectroscopy of H_2 Rydberg states. *Phys. Rev. A* **42**, 6950–6953 (1990).

20. Haase, C., Beyer, M., Jungen, C. & Merkt, F. The fundamental rotational interval of para-H_2^+ by MQDT-assisted Rydberg spectroscopy of H_2. *J. Chem. Phys.* **142**, 064310 (2015).

21. Fink, D. J. & Myers, E. G. Deuteron-to-proton mass ratio from simultaneous measurement of the cyclotron frequencies of H_2^+ and D^+. *Phys. Rev. Lett.* **127**, 243001 (2021).

22. Germann, M., Tong, X. & Willitsch, S. Observation of dipole-forbidden transitions in sympathetically cooled, state-selected, homonuclear diatomic molecular ions. *Nat. Phys.* **10**, 820–824 (2014).

23. Fleurbaey, H., Koroleva, A. O., Kassi, S. & Campargue, A. The high-accuracy spectroscopy of H_2 rovibrational transitions in the (2-0) band near 1.2 μm. *Phys. Chem. Chem. Phys.* **25**, 14749–14756 (2023).

24. Cozijn, F. M. J., Diouf, M. L. & Ubachs, W. Lamb dip of a quadrupole transition in H_2. *Phys. Rev. Lett.* **131**, 073001 (2023).

25. Komasa, J. Energy levels of the hydrogen molecule from relativistic nonadiabatic calculations. In *Proc. International Conference on Precision Physics and Fundamental Physical Constants (FFK)* (eds Widmann, E. & Karshenboim, S.) Tu-4 (Stefan Meyer Institute for Subatomic Physics, 2023); indico.cern.ch/event/1164804/

26. Jefferts, K. B. Hyperfine structure in the molecular ion H_2^+. *Phys. Rev. Lett.* **23**, 1476–1478 (1969).

27. Somerville, W. B. A revised radio-frequency spectrum for H_2^+. *Mon. Not. R. Astron. Soc.* **147**, 201–205 (1970).

28. Kalaghan, P. & Dalgarno, A. Hyperfine structure of the molecular ion H_2^+. *Phys. Lett. A* **38**, 485–486 (1972).

29. McEachran, R., Veenstra, C. & Cohen, M. Hyperfine structure in the hydrogen molecular ion. *Chem. Phys. Lett.* **59**, 275–280 (1978).

30. Babb, J. F. & Dalgarno, A. Electron-nuclear coupling in the hyperfine structure of the hydrogen molecular ion. *Phys. Rev. Lett.* **66**, 880–882 (1991).

31. Babb, J. F. & Dalgarno, A. Spin coupling constants and hyperfine transition frequencies for the hydrogen molecular ion. *Phys. Rev. A* **46**, R5317–R5319 (1992).

32. Haidar, M., Korobov, V. I., Hilico, L. & Karr, J.-P. Higher-order corrections to spin–orbit and spin–spin tensor interactions in hydrogen molecular ions: theory and application to H_2^+. *Phys. Rev. A* **106**, 022816 (2022).

33. Blythe, P., Roth, B., Fröhlich, U., Wenz, H. & Schiller, S. Production of ultracold trapped molecular hydrogen ions. *Phys. Rev. Lett.* **95**, 183002 (2005).

34. Yang, W., Alheit, R. & Werth, G. Vibrational population of H_2^+ after electroionization of thermal H_2. *Z. Phys. D: At. Mol. Clusters* **28**, 87–88 (1993).

35. Schneider, T., Roth, B., Duncker, H., Ernsting, I. & Schiller, S. All-optical preparation of molecular ions in the rovibrational ground state. *Nat. Phys.* **6**, 275–278 (2010).

36. Leung, K. H. et al. Terahertz vibrational molecular clock with systematic uncertainty at the 10^{-14} level. *Phys. Rev. X* **13**, 011047 (2023).

37. Amitay, Z., Zajfman, D. & Forck, P. Rotational and vibrational lifetime of isotopically asymmetrized homonuclear diatomic molecular ions. *Phys. Rev. A* **50**, 2304–2308 (1994).

38. Bakalov, D., Korobov, V. & Schiller, S. Magnetic field effects in the transitions of the HD^+ molecular ion and precision spectroscopy. *J. Phys. B: At. Mol. Opt. Phys.* **44**, 025003 (2011).

39. Karr, J.-P., Korobov, V. I. & Hilico, L. Vibrational spectroscopy of H_2^+: Precise evaluation of the Zeeman effect. *Phys. Rev. A* **77**, 062507 (2008).

40. Herzberg, G. & Jungen, C. Rydberg series and ionization potential of the H_2 molecule. *J. Mol. Spectrosc.* **41**, 425–486 (1972).

41. Menasian, S. C. *High Resolution Study of the (F, F_2)=(3/2, 1/2)→(1/2, 1/2) HFS Transitions in Stored H_2^+ Molecular Ions*. PhD thesis, Univ. of Washington (1973).

42. Schiller, S., Bakalov, D. & Korobov, V. I. Simplest molecules as candidates for precise optical clocks. *Phys. Rev. Lett.* **113**, 023004 (2014).

43. Karr, J.-P. H_2^+ and HD^+: candidates for a molecular clock. *J. Mol. Spectrosc.* **300**, 37–43 (2014).

44. Karr, J.-P. et al. Hydrogen molecular ions: new schemes for metrology and fundamental physics tests. *J. Phys.: Conf. Ser.* **723**, 012048 (2016).

45. Schiller, S. & Korobov, V. I. Canceling spin-dependent contributions and systematic shifts in precision spectroscopy of molecular hydrogen ions. *Phys. Rev. A* **98**, 022511 (2018).

46. Hori, M. et al. Buffer-gas cooling of antiprotonic helium to 1.5 to 1.7 K, and antiproton-to-electron mass ratio. *Science* **354**, 610–614 (2016).

47. Borchert, M. J. et al. A 16-parts-per-trillion measurement of the antiproton-to-proton charge-mass ratio. *Nature* **601**, 53–57 (2022).

48. Dehmelt, H. Economic synthesis and precision spectroscopy of anti-molecular hydrogen ions in Paul trap. *Phys. Scr.* **T59**, 423 (1995).

49. Myers, E. G. CPT tests with the antihydrogen molecular ion. *Phys. Rev. A* **98**, 010101 (2018).

50. Zammit, M. C. et al. Laser-driven production of the antihydrogen molecular ion. *Phys. Rev. A* **100**, 042709 (2019).

51. Kajita, M., Gopakumar, G., Abe, M., Hada, M. & Keller, M. Test of m_p/m_e changes using vibrational transitions in N_2^+. *Phys. Rev. A* **89**, 032509 (2014).

52. Hanneke, D., Carollo, R. A. & Lane, D. A. High sensitivity to variation in the proton-to-electron mass ratio in O_2^+. *Phys. Rev. A* **94**, 050101 (2016).

53. Wolf, F. et al. Non-destructive state detection for quantum logic spectroscopy of molecular ions. *Nature* **530**, 457–460 (2016).

54. Egl, A. et al. Application of the continuous Stern–Gerlach effect for laser spectroscopy of the $^{40}Ar^{13+}$ fine structure in a Penning trap. *Phys. Rev. Lett.* **123**, 123001 (2019).

55. Schmidt, J. et al. Trapping, cooling, and photodissociation analysis of state-selected H_2^+ ions produced by (3+1) multiphoton ionization. *Phys. Rev. Appl.* **14**, 024053 (2020).

56. König, C. M. et al. Hyperfine spectroscopy of single molecular hydrogen ions in a Penning trap at ALPHATRAP. In *Proc. International Conference on Precision Physics of Simple Atomic Systems* (eds Pachucki, K., Karshenboim, S. & Tong, X.) 14 (PSAS, 2022); psas.fuw.edu.pl/program/

57. Schwegler, N. et al. Trapping and ground-state cooling of a single H_2^+. *Phys. Rev. Lett.* **131**, 133003 (2023).

Methods

Details of the experiment

H_2^+ spectroscopy procedures. The experimental apparatus is the same we have used in our previous experiments[4,5]. We employ a modified spectroscopy scheme that allows us to perform spectroscopy of H_2^+ without requiring rotational state preparation.

First, the spectroscopy laser frequency is set to a desired value. One cycle (Extended Data Fig. 1) then starts by loading an ensemble of H_2^+ ions by electron impact ionization from a reservoir of para-H_2 admitted into the vacuum chamber by a leak valve. This is followed by depleting the population in levels with $v \geq 2$, including the upper spectroscopy level $(v' = 3, N' = 2)$, by performing photodissociation with two continuous-wave lasers at wavelengths of 313 and 405 nm. Since for both wavelengths the photodissociation cross section decreases strongly with decreasing v (ref. 58), the dissociation of molecules in $v = 1$ is negligible. After a subsequent determination of the number of trapped H_2^+ (see below), the vibrational transition $(v = 1, N = 0) \rightarrow (v' = 3, N' = 2)$ is excited and detected using resonance-enhanced multi-photon dissociation (REMPD), which has two steps: (1) excitation of the spectroscopy transition with the OPO radiation and (2) dissociation of the molecule from the upper spectroscopy level with the 405 nm laser (50 mW and intensity 25 W cm^{-2}). To avoid a light shift induced by the dissociation laser, an interleaved shuttering scheme was employed to prevent the simultaneous exposure of the ions to both lasers. Completing the cycle, the number of still trapped H_2^+ is determined.

In the following cycle, the background is measured (blue data points in Fig. 2). All settings are unchanged except that the OPO beam remains blocked. These alternating spectroscopy and background cycles are repeated many times until satisfactory statistics is accumulated. After completing each cycle, the ion cluster is purged from any ions other than Be$^+$ and a new H_2^+ ensemble is loaded so that there is a sufficient population in the lower spectroscopy level. During the REMPD intervals of both signal cycles and background cycles, we applied a magnetic field of $B = 0.0(2)$ μT, whereas at all other times the magnetic field was set to $B_{cooling} \approx 45$ μT. To acquire a spectroscopic line, we set the OPO frequency to a range of values.

The spectroscopy signal was obtained by comparing the number of trapped H_2^+ ions before and after the REMPD. The signal was computed as the normalized decrease of the number of trapped ions $(N_i - N_f)/(N_i - N_b)$, where N_i and N_f are the initial and final fluorescence peak strengths of the secular excitation signal of H_2^+, respectively, and N_b is the background level of fluorescence without any secular excitation. To determine the number of trapped H_2^+ ions, the transverse secular motion excitation spectrum was recorded over the range 450–1,250 kHz. The resonance frequency of H_2^+ under nominal conditions was approximately 1,000 kHz. The spectrum was fitted by two Gaussian functions. The peak strength of the H_2^+ signal, which is proportional to the number of trapped H_2^+ ions, was then determined. This approach differs from our previous ones for which we usually resonantly excited the secular motion at fixed frequency and did not record a spectrum. Here, the different approach is necessary because chemical reactions generate H_3^+ ions in the trap, and their presence modifies the Coulomb interactions within the cluster and, thus, also modifies the secular frequency of the H_2^+ ensemble.

HD$^+$ spectroscopy procedures. HD$^+$ ions are prepared in a string arrangement. The spectroscopy wave was aligned perpendicular to the string, allowing us to obtain Doppler-free resonances. The $v = 0$ rotational state preparation was implemented by a quantum cascade laser tuned to the $(v = 0, N = 2) \rightarrow (v' = 1, N' = 1)$ transition (5.5 μm). The REMPD scheme comprises three excitations: the spectroscopy transition $(v = 0, N = 0) \rightarrow (v' = 2, N' = 2)$, a subsequent vibrational excitation $(v' = 2, N' = 2) \rightarrow (v'' = 6, N'' = 3)$ (1.56 μm) and finally photodissociation by a 266 nm wave. The second excitation enhances the dissociation rate because the photodissociation cross section of the level $(v' = 2, N' = 2)$ is small at 266 nm.

The spectroscopy cycle sequence is the same as in refs. 4,5, except that the REMPD duration was increased to 30 s. We mention only the main aspects here. The spectroscopy wave was interleaved with the other two waves to avoid systematic shifts. Before and after REMPD the secular motion of HD$^+$ was resonantly excited to determine their number. Signal and background data were taken during alternating cycles. The cycles differ only in that the spectroscopy wave was kept blocked during the background cycle. On average, five signal and background cycle pairs can be executed before the HD$^+$ population has declined substantially. Once this has occurred, the Be$^+$ ion cluster is cleaned. That is, any ions other than beryllium are removed, and a fresh string of HD$^+$ ions is prepared. The quantum cascade laser was kept on during REMPD.

Spectroscopy laser system. The spectroscopy laser system is a continuous-wave OPO with an output power of >2 W at the H_2^+ and HD$^+$ transition wavelengths of 2.4 and 2.6 μm, respectively. The OPO wave was frequency-doubled to a second-harmonic wave that is suitable for generating a heterodyne beat with an erbium-fibre frequency comb. The second-harmonic wave was phase-locked to a comb line using this beat and feedback control to the OPO pump laser frequency. This effectively also locked the frequency of the spectroscopy wave to the comb.

To ensure the ultra-narrow linewidth of the spectroscopy radiation, the comb was optically stabilized by phase-locking to a near-infrared laser that is frequency-locked to a high-finesse resonator. Through a second beat with an independently optically stabilized frequency comb, we determined that the fractional frequency instability (Allan deviation) of the OPO spectroscopy wave frequency is below 1×10^{-13} for integration times longer than 1 s. An upper bound for the linewidth of the OPO radiation was obtained from an analysis of the beat. On the 5 s timescale, it was 10 Hz (full-width at half-maximum of a Lorentzian fit). This is also the main contribution to the OPO frequency uncertainty and as such determines the horizontal error bars shown in Fig. 3. Both combs were referenced to an active hydrogen maser, whose properties were characterized (Methods, 'Maser shift').

E2 transitions of H_2^+ and HD$^+$

E2 in H_2^+. The E2 reduced transition matrix element of the studied first-overtone transition is $Q_0 = Q_{H_2^+}(v = 1, N = 0 \rightarrow v' = 3, N' = 2) = -0.053268$ atomic units[11]. Note that Q_0 is larger by almost a factor of 2 compared to the first overtone starting from $v = 0$: $Q_{H_2^+}(v = 0, N = 0 \rightarrow v' = 2, N' = 2) = -0.028919$ atomic units[11]. However, Q_0 is smaller by a factor of 9 compared to the fundamental vibrational transition starting from the same lower level $(v = 1, N = 0 \rightarrow v' = 2, N' = 2)$. Our spectroscopy source has adequate power to compensate for this difference.

For the upper rovibrational level, the Einstein coefficient for spontaneous emission was computed as $A_{H_2^+}(v' = 3, N' = 2 \rightarrow v = 1, N = 0) \approx 7.8 \times 10^{-8}$ s^{-1} (refs. 11,59).

E2 in HD$^+$. E2 transitions in this heteronuclear molecule have been discussed in refs. 45,60. The E2 reduced transition matrix element is $Q_{HD^+}(v = 0, N = 0 \rightarrow v' = 2, N' = 2) = 0.025976$ atomic units. The reduced electric-dipole (E1) transition matrix elements for near-by transitions are 0.00436 for the $(v = 0, N = 0) \rightarrow (2, 1)$ transition and −0.00609 for the $(v = 0, N = 1) \rightarrow (2, 2)$ transition, in atomic units[61]. Thus, the Rabi frequencies for these E1 transitions are approximately one order larger than for the studied E2 transition of HD$^+$.

Power-broadening. The Rabi frequency for an E2 transition in H_2^+ can be estimated using equation (15) of ref. 11. Using the E2 transition matrix element Q_0 and considering the peak intensity of the spectroscopy wave (3.6 MW m^{-2}), we estimated an upper limit for the Rabi frequency to be $\Omega/(2\pi) \approx 0.5$ kHz. Therefore, power-broadening is negligible compared to the observed linewidth.

The Rabi frequency for an E2 transition in HD$^+$ between stretched states can be obtained from the same equation. The peak intensity in the E2 spectroscopy of HD$^+$ was 2.6 MW m^{-2}. Taking into account the angle between the magnetic field and the wavevector and its uncertainty, we estimated the Rabi frequency to be $\Omega/(2\pi) \leq 15$ Hz, consistent with the observed linewidths.

Systematics of the HD$^+$ E2 transition

Zeeman shift. See Fig. 3, all panels. The magnetic field in our trap was characterized by stimulated Raman spectroscopy to precisely measure the Zeeman splitting of beryllium ions[62] and, by comparison, of the observed and calculated Zeeman splittings of the fundamental rotational transition[2]. Comparing the measured Zeeman splitting of the two components, 0.72(7) kHz, with the theoretical prediction, equation (6) in ref. 38, we deduced a magnetic field strength of 30 μT, consistent with the previous determinations for the same coil current settings.

Trap-field-induced shift. The RF electric field in the trap induces a shift, which was determined for both Zeeman components at nominal magnetic field (Fig. 3a). Measurements at three different RF amplitudes and extrapolation to zero amplitude indicate that there was a systematic shift of approximately +1.2 kHz for both components under the nominal operating conditions. This type of shift was observed by us earlier[2]; for a recent investigation of a different molecular ion, see ref. 63.

a.c. and d.c. Stark shifts. The beryllium ion cooling laser, the spectroscopy wave and the rotational cooling laser potentially cause a.c. Stark shifts (Fig. 3c–d). We measured the transition frequencies at different laser wave powers but did not resolve any light shift induced by these waves.

Also, we could not resolve any d.c. Stark shift upon comparing the transition frequencies measured under the nominal conditions and for an additional d.c. voltage of 5 V applied to two trap electrodes (Fig. 3b).

Maser shift. All frequencies used for the HD$^+$ measurements were corrected for the hydrogen maser frequency offset. The offset was determined by continuously comparing the maser frequency to an atomic time signal provided by a global navigation satellite system at 1 pulse per second. The fractional offset from the atomic frequency and the fractional drift were found to be $\approx 8 \times 10^{-12}$ and $\approx 1 \times 10^{-13}$ per month, respectively. Since the spectroscopy measurements were taken over 2 months, the laser frequencies obtained on a particular measurement day were corrected for the offset on that day.

Systematics of the H$_2^+$ E2 transitions

Theory of Zeeman shifts. The Zeeman shifts in a weak field are discussed in refs. 44,45 for $N = 0 \rightarrow N' = 2$ transitions, and in refs. 42,43,45 for $N = 2 \rightarrow N' = 2$ transitions. For a strong field, ref. 49 gives a partial discussion of a $N = 2 \rightarrow N' = 2$ transition.

For completeness, we present in Extended Data Table 1 the Hamiltonians $H_{spin}(N) + H_{Zeeman}(N)$ for $N = 2$ and for the trivial case $N = 0$. The $N = 2$ case uses the approximation of isotropic electronic g factor; for the calculation of the anisotropy, see refs. 64,65.

Note that the electronic g factor $g_e(v, N)$ (refs. 64,65), the rotational g factor $g_i(v, N)$[39] and the spin-rotation coupling constant $c_e(v, N)$ (ref. 32) depend on the rovibrational level. Because the dependencies are weak, there are rovibrational transitions with low magnetic sensitivity. In addition, by measuring two or more Zeeman components and suitably averaging them, the net Zeeman shift can be made to cancel.

From the Hamiltonians, one can compute the Zeeman shifts for transitions of the type $(v, N = 0) \rightarrow (v', N' = 2)$, $(v, N = 2) \rightarrow (v', N' = 0)$ and $(v, N = 2) \rightarrow (v', N' = 2)$ for arbitrary field strength and perform series expansions in the low-field limit (for RF traps) and in the high-field limit (for Penning traps). These lead to the expressions in Extended Data Table 2.

The predicted frequencies of a few selected HFS components of the transition studied in the present work are displayed in Extended Data Table 3. The magnitude of the linear Zeeman shift of the components $f_b^{(\pm)}$, ± 5.6 kHz $\times B/\mu$T, determines an upper limit for the allowable instability of the magnetic field, δB, for a desired total uncertainty.

Next, we mention some examples of interesting transitions in a Penning trap. The two Zeeman components $(v = 0, N = 2, m_s = \pm 1/2, m_F = \pm 1/2) \rightarrow (v' = 1, N' = 2, m_s = \pm 1/2, m_F = \pm 1/2)$ have sensitivities of ± 8.2 kHz T^{-1} at $B = 4$ T. The two Zeeman components $(v = 0, N = 0, m_s = \pm 1/2, m_F = \pm 1/2) \rightarrow (v' = 1, N' = 2, m_s = \pm 1/2, m_F = \pm 1/2)$ have sensitivities of ± 3.6 kHz T^{-1} at $B = 4$ T. These values are even lower than for the Zeeman component discussed in ref. 49, namely 150 kHz T^{-1}. The values of v and v' were chosen for comparison with that reference, but similar results hold also for other transitions.

Light shifts. A potential light shift from the 405 nm photodissociation laser is prevented by using appropriate interleaved shuttering.

The light shift due to the beryllium cooling wave (313 nm) and the OPO radiation can be estimated using a comparison with HD$^+$, for which it was determined to be less than 0.1 kHz.

Our analysis is based on ref. 66. For the transition in HD$^+$, the frequency-dependent polarizabilities should be considered. At 2.6 μm, the differential scalar polarizability is $\alpha_s(v' = 2, N' = 2) - \alpha_s(v = 0, N = 0) \approx 1.5$ atomic units. The tensor polarizability is estimated as $\alpha_t(v' = 2, N' = 2) = -0.1$ atomic units (it is zero when $N = 0$). This is to be multiplied by a Zeeman-state-dependent factor, which for the two addressed (pure) Zeeman states is 12.3. The maximum polarizability of the transition is, therefore, approximately 2.3 atomic units.

For the 2.4 μm radiation interrogating H$_2^+$, the light shift is essentially determined by the static polarizabilities, because the E1 transition dipole moments between rovibrational levels of the electronic ground state are effectively zero and because the spectroscopy wave photon energy is small compared to the excitation energy to higher electronic states. For the scalar polarizability, $\alpha_s(v' = 3, N' = 2) - \alpha_s(v = 1, N = 0) = 2.1$ atomic units. The tensor polarizability is $\alpha_t(v' = 3, N' = 2) = -0.53$ atomic units. This is again to be multiplied by a Zeeman-state-dependent factor. The largest factors for the two studied transitions (which contain all m_F' values) are 21/5 for the $F' = 3/2$ multiplet and 6 for the $F' = 5/2$ multiplet. The maximum polarizability of any Zeeman component of the transition is, therefore, approximately 3.2 atomic units. This value is close to that for the HD$^+$ case, and therefore, we may infer that the light shift from the OPO radiation is negligible in the present H$_2^+$ measurement and that it should be controllable at the 1×10^{-12} level in a next-generation experiment.

For the wavelength 313 nm, the differential polarizabilities are close to those at the spectroscopy wavelengths. Because of the much lower intensity of the 313 nm radiation, the corresponding light shift is negligible in comparison.

Other shifts. We have not measured the black-body shift of either HD$^+$ or H$_2^+$, but theory[66] predicts it to be at the 1×10^{-17} level for the present H$_2^+$ transition at room temperature.

We hypothesize that the trap shift that we observed for HD$^+$ for various transitions[2,4,5], including for the present one, may in part be due to off-resonant electric-dipole coupling to close rovibrational levels (a quasi-static Stark shift). Since E1 couplings between rovibrational levels in the ground electronic state are negligible in H$_2^+$, the trap shift could be smaller than in HD$^+$. Relevant static Stark shift coefficients for H$_2^+$ are discussed above.

Ab initio theory of $f_{spin\text{-}avg}$

The computation of the spin-averaged frequency follows ref. 67. CODATA 2018 recommended values for fundamental constants are used. The transition frequency is computed as a power series in the

fine-structure constant α. Considering the present experimental accuracy, only the major contributions need to be included:

$$
\begin{aligned}
f_{\text{spin-avg}} = \ & 124{,}485{,}554.55\,\text{MHz} && (\text{nonrelativistic}) \\
+ \ & 2{,}002.70\,\text{MHz} && (\alpha^2\,\text{order}) \\
- \ & 521.35\,\text{MHz} && (\alpha^3\,\text{order}) \\
- \ & 3.69\,\text{MHz} && (\alpha^4\,\text{order}) \\
+ \ & 0.24(6)\,\text{MHz} && (\alpha^5\,\text{order}) \\
= \ & 124{,}487{,}032.45(6)\,\text{MHz}. && (\text{total})
\end{aligned}
$$

The orders are relative to the non-relativistic contribution. The α^5 contribution is a simple estimate based on ref. 67. Once the need arises, this contribution can be computed accurately and so can contributions of higher order. The sensitivity of the spin-averaged frequency to m_p/m_e is computed by solving the non-relativistic Schrödinger equation for two different values of m_p/m_e. We find $\partial f_{\text{spin-avg}}/\partial(m_\text{p}/m_\text{e}) = -0.43976 \times f_{\text{spin-avg}}/(m_\text{p}/m_\text{e})$.

Data availability
Source data are provided with this paper. All other data that support the plots within this paper and other findings of this study are available from the corresponding author upon reasonable request.

Code availability
No custom code or software was used for analysing or presenting the data associated with this paper.

References
58. Dunn, G. H. Photodissociation of H_2^+ and D_2^+: Theory. *Phys. Rev.* **172**, 1-7 (1968).
59. Olivares Pilón, H. & Baye, D. Quadrupole transitions in the bound rotational-vibrational spectrum of the hydrogen molecular ion. *J. Phys. B: At. Mol. Opt. Phys.* **45**, 065101 (2012).
60. Bekbaev, A. K., Aznabayev, D. T. & Korobov, I. V. Quadrupole transitions of the hydrogen molecular ion HD⁺. In *Proc. International Conference on Precision Physics and Fundamental Physical Constants* Vol. 9 (eds Horváth, D., Karshenboim, S. & Siklér, F.) 058 (2019).
61. Bakalov, D. & Schiller, S. Static Stark effect in the molecular ion HD⁺. *Hyperfine Interact.* **210**, 25–31 (2012).
62. Shen, J., Borodin, A. & Schiller, S. A simple method for characterization of the magnetic field in an ion trap using Be⁺ ions. *Eur. Phys. J. D* **68**, 359 (2014).
63. Collopy, A. L., Schmidt, J., Leibfried, D., Leibrandt, D. R. & Chou, C.-W. Effects of an oscillating electric field on and dipole moment measurement of a single molecular ion. *Phys. Rev. Lett.* **130**, 223201 (2023).
64. Hegstrom, R. A. *g* factors and related magnetic properties of molecules. Formulation of theory and calculations for H_2^+, HD⁺, and D_2^+. *Phys. Rev. A* **19**, 17–30 (1979).
65. Karr, J.-P. Leading-order relativistic corrections to the *g* factor of H_2^+. *Phys. Rev. A* **104**, 032822 (2021).
66. Schiller, S., Bakalov, D., Bekbaev, A. K. & Korobov, V. I. Static and dynamic polarizability and the Stark and blackbody-radiation frequency shifts of the molecular hydrogen ions H_2^+, HD⁺, and H_2^+. *Phys. Rev. A* **89**, 052521 (2014).
67. Korobov, V. I., Hilico, L. & Karr, J.-P. Fundamental transitions and ionization energies of the hydrogen molecular ions with few ppt uncertainty. *Phys. Rev. Lett.* **118**, 233001 (2017).

Acknowledgements

Author contributions
M.R.S. and S.A. performed the experiments and analysed the data. M.R.S. developed and characterized the spectroscopy laser system. S.A. maintained the apparatus. S.S. conceived the experiment, supervised the project and performed analyses. All authors contributed to writing the manuscript and reviewing the data.

Competing interests
The authors declare no competing interests.

Additional information
Extended data is available for this paper at https://doi.org/10.1038/s41567-023-02320-z.

Supplementary information The online version contains supplementary material available at https://doi.org/10.1038/s41567-023-02320-z.

Correspondence and requests for materials should be addressed to S. Schiller.

Peer review information *Nature Physics* thanks Shui-Ming Hu, Krzysztof Pachucki and Xin Tong for their contribution to the peer review of this work.

Reprints and permissions information is available at www.nature.com/reprints.
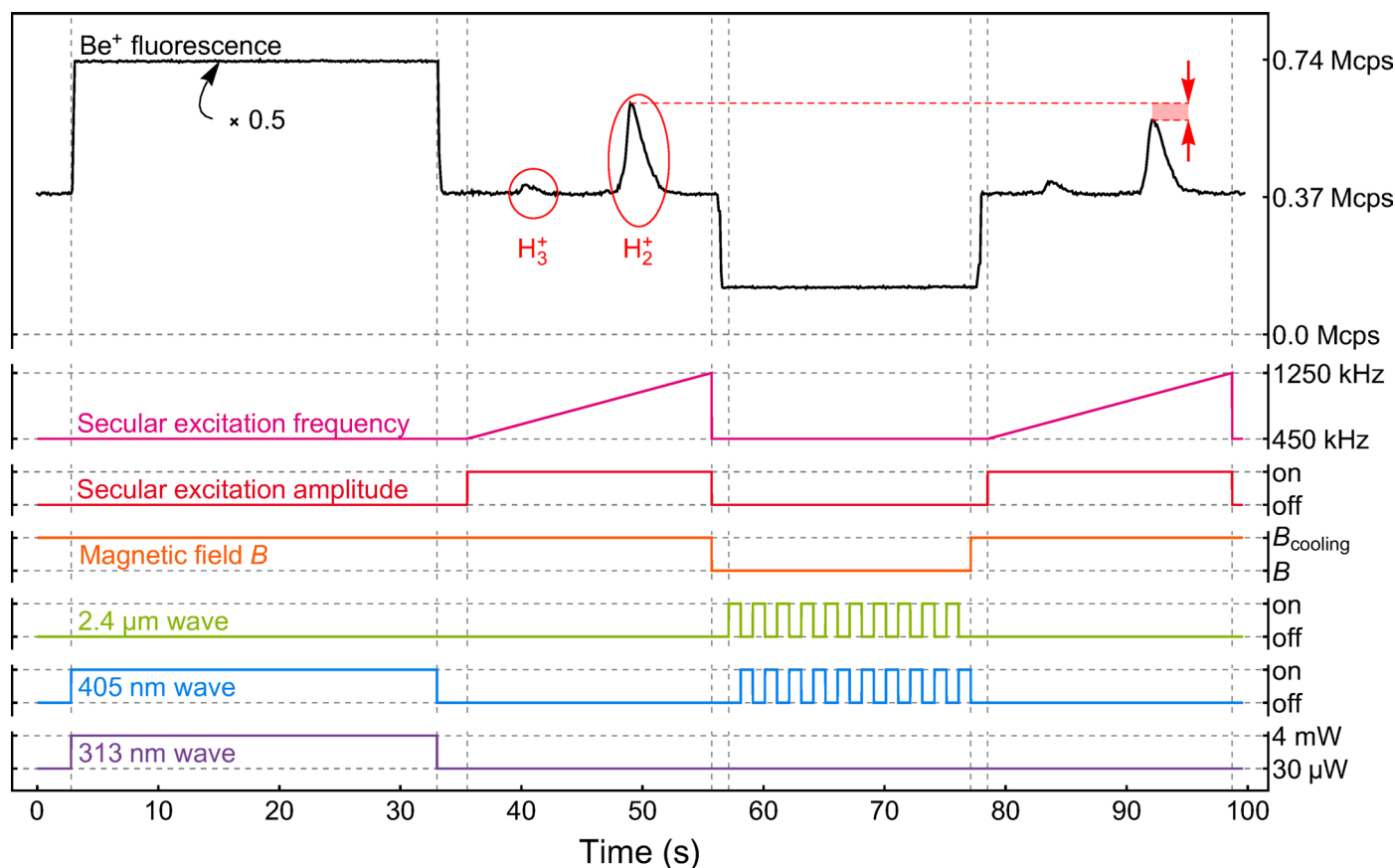
Extended Data Fig. 1 | The H_2^+ spectroscopy cycle. The black trace is the Be$^+$ fluorescence detected by a photomultiplier tube in mega counts per second (Mcps). During the depletion of the excited state population (see Methods, section 1.a), the fluorescence is multiplied by 0.5 for illustration purposes. The red ovals indicate the radial secular excitation resonance of the trapped H_2^+ and H_3^+ ions. The actual spectroscopy signal, that is the reduction of the number of trapped H_2^+ ions by the REMPD process, is highlighted in the top (black) signal by the red dashed lines and red arrows. The interleaved shuttering during the REMPD is shown simplified with only 10 repetitions. In actuality, there are 310 repetitions of duration $\simeq 62$ ms each. Each consists of two 30 ms and two 1 ms intervals. During the 30 ms intervals, either the 2.4 μm wave or the 405 nm wave is sent to the ions. The 1 ms intervals act as a buffers in-between. The cycle for measuring the background is analogous, except that the 2.4 μm wave is off during the whole cycle. During the exposure to the REMPD lasers, the magnetic field was $|B| \leq 0.2$ μT, while at all other times a magnetic field $B_{cooling}$ for the purpose of Doppler-cooling was applied. The values and status of each parameter are displayed on the right-hand vertical axis.

Extended Data Table 1 | Hamiltonians for rovibrational levels (v, $N=0, 2$) in H_2^+

m_F	$H_{\text{spin}}(N=0)/c_e$	$H_{\text{Zeeman}}(N=0, m_F)/b$
$-\frac{1}{2}$	(0)	$\frac{1}{2}(g_e)$
$\frac{1}{2}$	(0)	$\frac{1}{2}(-g_e)$

m_F	$H_{\text{spin}}(N=2)/c_e$	$H_{\text{Zeeman}}(N=2, m_F)/b$
$-\frac{5}{2}$	1	$\frac{1}{2}(g_e + 4g_1)$
$-\frac{3}{2}$	$\begin{pmatrix} -\frac{3}{2} & 0 \\ 0 & 1 \end{pmatrix}$	$\frac{1}{10}\begin{pmatrix} -3(g_e - 6g_1) & 4(g_e - g_1) \\ 4(g_e - g_1) & 3(g_e + 4g_1) \end{pmatrix}$
$-\frac{1}{2}$	$\begin{pmatrix} -\frac{3}{2} & 0 \\ 0 & 1 \end{pmatrix}$	$\frac{1}{10}\begin{pmatrix} -g_e + 6g_1 & 2\sqrt{6}(g_e - g_1) \\ 2\sqrt{6}(g_e - g_1) & g_e + 4g_1 \end{pmatrix}$
$\frac{1}{2}$	$\begin{pmatrix} -\frac{3}{2} & 0 \\ 0 & 1 \end{pmatrix}$	$\frac{1}{10}\begin{pmatrix} g_e - 6g_1 & 2\sqrt{6}(g_e - g_1) \\ 2\sqrt{6}(g_e - g_1) & -g_e - 4g_1 \end{pmatrix}$
$\frac{3}{2}$	$\begin{pmatrix} -\frac{3}{2} & 0 \\ 0 & 1 \end{pmatrix}$	$\frac{1}{10}\begin{pmatrix} 3(g_e - 6g_1) & 4(g_e - g_1) \\ 4(g_e - g_1) & -3(g_e + 4g_1) \end{pmatrix}$
$\frac{5}{2}$	1	$\frac{1}{2}(-g_e - 4g_1)$

H_{spin} is the hyperfine structure hamiltonian. The Zeeman hamiltonian H_{Zeeman} for $N=2$ levels is approximate. Here, $c_e(v, N)$ is the spin-rotation coefficient, m_F is the projection of the total angular momentum F onto the static magnetic field direction, $g_e(v, N)$ and $g_1(v, N)$ are the electron and rotational g factors, respectively, and $b = \mu_B B = e\hbar B/2m_e$ is the product of Bohr magneton μ_B and magnetic field B, expressed in Hz, with the electron charge e, the reduced Planck constant $\hbar$, and the electron mass m_e. Note that $g_e \simeq -2$ is negative.

Extended Data Table 2 | Approximate expressions for the energies of the states of H_2^+ in rotational levels $N=2$

m_F	Small–B expansion	
	lower energy group, $F=3/2$	higher energy group, $F=5/2$
$-\frac{5}{2}$		$c_e + \frac{1}{2} b \, (g_e + 4\,g_1)$
$-\frac{3}{2}$	$-\frac{3\,c_e}{2} - \frac{3}{10}\, b\,(g_e - 6\,g_1) - \frac{8\,b^2\,(g_e-g_1)^2}{125\,c_e}$	$c_e + \frac{8\,b^2\,(g_e-g_1)^2}{125\,c_e} + \frac{3}{10}\,b\,(g_e + 4\,g_1)$
$-\frac{1}{2}$	$-\frac{3\,c_e}{2} - \frac{1}{10}\, b\,(g_e - 6\,g_1) - \frac{12\,b^2\,(g_e-g_1)^2}{125\,c_e}$	$c_e + \frac{12\,b^2\,(g_e-g_1)^2}{125\,c_e} + \frac{1}{10}\,b\,(g_e + 4\,g_1)$
$\frac{1}{2}$	$-\frac{3\,c_e}{2} + \frac{1}{10}\, b\,(g_e - 6\,g_1) - \frac{12\,b^2\,(g_e-g_1)^2}{125\,c_e}$	$c_e + \frac{12\,b^2\,(g_e-g_1)^2}{125\,c_e} - \frac{1}{10}\,b\,(g_e + 4\,g_1)$
$\frac{3}{2}$	$-\frac{3\,c_e}{2} + \frac{3}{10}\, b\,(g_e - 6\,g_1) - \frac{8\,b^2\,(g_e-g_1)^2}{125\,c_e}$	$c_e + \frac{8\,b^2\,(g_e-g_1)^2}{125\,c_e} - \frac{3}{10}\,b\,(g_e + 4\,g_1)$
$\frac{5}{2}$		$c_e - \frac{1}{2} b \, (g_e + 4\,g_1)$

m_F	Large–B expansion	
	lower energy group, $m_s=-1/2$	higher energy group, $m_s=1/2$
$-\frac{5}{2}$	$c_e + \frac{1}{2} b \, (g_e + 4\,g_1)$	
$-\frac{3}{2}$	$\frac{c_e}{2} + \frac{c_e^2}{b\,(g_e-g_1)} + \frac{1}{2}\, b\,\left(g_e + 2\,g_1\right)$	$-c_e - \frac{c_e^2}{b\,(g_e-g_1)} + \frac{1}{2}\, b\,\left(-g_e + 4\,g_1\right)$
$-\frac{1}{2}$	$\frac{b\,g_e}{2} + \frac{3\,c_e^2}{2\,b\,(g_e-g_1)}$	$-\frac{c_e}{2} - \frac{3\,c_e^2}{2\,b\,(g_e-g_1)} + \frac{1}{2}\, b\,\left(-g_e + 2\,g_1\right)$
$\frac{1}{2}$	$-\frac{c_e}{2} + \frac{1}{2}\, b\,\left(g_e - 2\,g_1\right) + \frac{3\,c_e^2}{2\,b\,(g_e-g_1)}$	$-\frac{b\,g_e}{2} - \frac{3\,c_e^2}{2\,b\,(g_e-g_1)}$
$\frac{3}{2}$	$-c_e + \frac{1}{2}\, b\,\left(g_e - 4\,g_1\right) + \frac{c_e^2}{b\,(g_e-g_1)}$	$\frac{c_e}{2} + \frac{1}{2}\, b\,\left(-g_e - 2\,g_1\right) - \frac{c_e^2}{b\,(g_e-g_1)}$
$\frac{5}{2}$		$c_e - \frac{1}{2} b \, (g_e + 4\,g_1)$

Here, $c_e(v,N)$ is the spin-rotation coefficient, m_F is the projection of the total angular momentum F onto the static magnetic field direction, $g_e(v,N)$ and $g_I(v,N)$ are the electron and rotational g factors, respectively, m_s is the electron spin projection quantum number and $b=\mu_B B=e\hbar B/2m_e$ is the product of Bohr magneton μ_B and magnetic field B, expressed in Hz, with the electron charge e, the reduced Planck constant $\hbar$, and the electron mass m_e. Note that $g_e \simeq -2$ is negative.

Extended Data Table 3 | Theoretical values of the spin and Zeeman contributions of some Zeeman components of the studied transition ($v=1, N=0$)→($v'=3, N'=2$), in weak magnetic field B in units of μT

	HFS component				contributions	
	F	m_F	F'	$m_{F'}$	spin frequency (kHz)	Zeeman shift
$f_a^{(-)}$	$\frac{1}{2}$	$-\frac{1}{2}$	$\frac{5}{2}$	$-\frac{5}{2}$	34 730.3	$+14\,\text{Hz} \times B$
$f_a^{(+)}$	$\frac{1}{2}$	$+\frac{1}{2}$	$\frac{5}{2}$	$+\frac{5}{2}$	34 730.3	$-14\,\text{Hz} \times B$
$f_b^{(-)}$	$\frac{1}{2}$	$+\frac{1}{2}$	$\frac{3}{2}$	$-\frac{3}{2}$	$-52\,095.4$	$-5.6\,\text{kHz} \times B - 1.4\,\text{Hz} \times B^2$
$f_b^{(+)}$	$\frac{1}{2}$	$-\frac{1}{2}$	$\frac{3}{2}$	$+\frac{3}{2}$	$-52\,095.4$	$+5.6\,\text{kHz} \times B - 1.4\,\text{Hz} \times B^2$
$f_{\text{spin−avg}}$	$\frac{3}{10}(f_a^{(-)} + f_a^{(+)}) + \frac{2}{10}(f_b^{(-)} + f_b^{(+)})$				0	$-0.6\,\text{Hz} \times B^2$
c_e	$\frac{1}{5}(f_a^{(-)} + f_a^{(+)}) - \frac{1}{5}(f_b^{(-)} + f_b^{(+)})$				34 730.3	$+0.6\,\text{Hz} \times B^2$

Values are rounded. In future spectroscopy with Doppler-free resolution, the four frequencies $f_{a,b}^{(+,-)}$ should be measured in order to obtain $f_{\text{spin−avg}}$ as shown in row 7. The linear Zeeman shifts cancel in the computed $f_{\text{spin−avg}}$ and also in the computed spin-rotation interaction strength c_e, leaving small nonzero quadratic shifts. Here, $m_F(m'_F)$ is the projection of the total angular momentum $F(F')$ of the lower (upper) state onto the static magnetic field direction.

5.3. Determination of the proton-electron mass ratio by high-accuracy laser spectroscopy of H$_2^+$

Copyright notice:

This manuscript has been accepted for publication in *Nature* [42]. All copyright remains with the authors.

The supplementary material of this manuscript is presented in Appendix C.

The contributions of the author of this thesis are detailed in the corresponding section of the manuscript on page 90.

Determination of the proton-electron mass ratio by high-accuracy laser spectroscopy of H_2^+

S. Alighanbari, M. R. Schenkel, and S. Schiller*

Institut für Experimentalphysik, Heinrich-Heine-Universität Düsseldorf, 40225 Düsseldorf, Germany

V. I. Korobov

Bogoliubov Laboratory of Theoretical Physics,

Joint Institute for Nuclear Research, 141980 Dubna, Russia

(All Authors contributed equally.)

(Dated: October 15, 2024)

Abstract

The molecular hydrogen ions (MHI) are three-body systems suitable for advancing our knowledge in several domains: determination of fundamental constants, test of quantum physics, search for new interparticle forces, tests of the weak equivalence principle [1], and, once the anti-molecule $\bar{p}\bar{p}e^+$ becomes available, novel tests of charge-parity-time-reversal (CPT) symmetry and local position invariance [1–3]. In order to achieve these goals, high-accuracy experimental - and in part also theoretical - data on the vibrational and rotational transition frequencies in the ground electronic state is necessary. So far, research has focused on the heteronuclear HD^+ molecule [4–7]. Fully exploiting the potential of MHI requires studying the other isotopologues [8]. The homonuclear species H_2^+ is both complementary and simpler than HD^+, but also presents greater experimental challenges. Here, we achieve the first Doppler-free laser spectroscopy of a H_2^+ rovibrational transition and accurately determine its frequency with 8×10^{-12} fractional uncertainty, 10^3 times smaller than any previous experimental determination of a H_2^+ property [9–11]. We also determine the spin-rotation coupling coefficient with 0.1 kHz uncertainty, a 15 -fold improvement over the previous result [12]. Our value is consistent with the state-of-the-art theory prediction [13]. The combination of our theoretical and experimental H_2^+ data allows us to deduce a new value for m_p/m_e. It is in agreement with the essentially independent CODATA 2018 value, and has 2.5 times lower uncertainty. From combined MHI, H/D, and muonic H/D data we determine the baryon mass ratio m_d/m_p with 1.1×10^{-10} uncertainty. The value agrees with the directly measured mass ratio [14], Finally, we present one of the best matches between a theory prediction and an experimental result, with a fractional uncertainty of 8.1×10^{-12} . Both results imply a notable confirmation of the predictive power of quantum theory and indicate absence of beyond-the-standard-model-effects at these levels.

INTRODUCTION

The relative simplicity of the MHI allows for the impressively accurate computation of their properties. Currently, the fractional uncertainty of the predictions of rovibrational transition frequencies is 8×10^{-12} [15], only a factor approximately 10 larger than for the well-known 1s - 2s transition of the theoretically more easily tractable hydrogen atom [16]. The calculations can be performed with equal accuracy for any member of the MHI family.

Crucially, the calculations require several fundamental constants as input: the Rydberg constant R_∞, the ratio m_e/m_n of electron mass to the mass of any present nucleus n, the charge radius r_n of any such nucleus, and the fine structure constant α. These constants enter for fundamental reasons: R_∞ defines the energy or frequency scale of all atomic and molecular energy differences; the mass ratios affect the rotational and vibrational energies through the inertia of the nuclei. The nuclear charge radii subtly affect the electron's potential energy. Finally, α quantifies the strength of quantum electrodynamics (QED) contributions to the electron's energy. The latter two effects depend on internuclear distance, and therefore are also discernible in transition frequencies. With the exception of α, the uncertainties u of the constants are not negligible when considering comparisons between computed and measured frequencies. Therefore, a high-accuracy measurement of any transition, rotational or rovibrational, of any MHI species can contribute to reducing the uncertainty of those constants. Importantly, from MHI spectroscopy data and theory, combined with spectroscopy data and theory on atomic hydrogen/deuterium, muonic hydrogen/deuterium (μH, μD), it is possible to determine the proton-electron and deuteron-proton mass ratios m_p/m_e, m_d/m_p [8, 17]. This approach is independent and complementary to the more established one based on mass spectrometry [14] and electron spin resonance (ESR) in Penning traps [18]. Such a situation is highly beneficial to the field of fundamental constants, as measurements of the same quantities are made by different teams and moreover involve different theoretical calculations. However, the same theoretical framework is employed, QED, specifically, its nonrelativistic limit [19]. Until now, measurements of rotational and rovibrational transitions of MHI with competitive accuracy have only been accomplished in the heteronuclear HD$^+$ [4–7].

Table I presents an overview of selected approaches for determining mass ratios of electron, proton and deuteron, and r_p, r_d. While these constants can be determined with well-known approaches (rows 2, 7), MHI results can in principle provide independent values of the constants, or contribute data for a potentially more precise determination based on the complete data set. For example (row 3) HD$^+$ rovibrational data and its theory, combined with r_p from μH spectroscopy, the R_∞ from atomic hydrogen spectroscopy, and r_d from the H/D isotope shift (and corresponding theory), yield the ratio of reduced nuclear mass, $\mu_{pd} = 1/(m_p^{-1} + m_d^{-1})$, to electron mass m_e [7]. This ratio result has furthermore been combined with a very accurate measurement of m_p/m_d, obtained using a Penning trap storing alternately a deuteron and a H$_2^+$ ion [14], to provide the proton-electron mass ratio

$[m_p/m_e]_{\text{HD}^+}$. It can be compared with an independent determination from ESR on a single hydrogen-like ion [18] (row 2). The two values are in agreement.

New possibilities arise if high-accuracy data for H_2^+ become available (Tab. I, rows 4, 6, 8, 9). However, H_2^+ experiments are challenging. In the past, determinations of rotational or vibrational transition frequencies have been limited to uncertainties above 1×10^{-6} [20–22], much larger than current theoretical uncertainty, 8×10^{-12}. An experimental breakthrough was recently reported by us, laser spectroscopy of sympathetically cooled H_2^+ via an electric quadrupole (E2) transition [10], reaching 1.2×10^{-8} uncertainty. Studies of Rydberg states of neutral H_2 [23, 24] can also provide data on H_2^+, and a recent experiment determined a vibrational frequency with 8×10^{-9} uncertainty [11].

In the present work, we improve direct H_2^+ spectroscopy by three orders of magnitude in accuracy, and for the first time succeed in matching the theory prediction uncertainty for a H_2^+ vibrational transition. As we show, our measurement and the corresponding theoretical calculation jointly provide a milestone in the field of fundamental constants: we obtain a new, purely laser spectroscopic value of m_p/m_e and, together with our previous HD$^+$ data, a purely spectroscopic value of m_d/m_p. In both cases atomic laser spectroscopy data contributes. These two values can be compared with those obtained from respective Penning trap experiments [14, 25]. Further combinations of measurement results are also considered.

LASER SPECTROSCOPY OF A VIBRATIONAL TRANSITION IN H_2^+

In order to accomplish vibrational spectroscopy of H_2^+, a suitable method is E2 spectroscopy [26]. As this is a particular type of one-photon spectroscopy, strong confinement of the molecules in the direction along the propagation of the spectroscopy laser is necessary in order to observe Doppler-free lines [6, 7, 10]. For this purpose, our experiment utilises a linear radiofrequency (RF) ion trap to confine a small number of MHI, which are then sympathetically cooled to millikelvin temperature via interactions with a cluster of laser-cooled beryllium ions [27]. This results in the MHI being confined close to the symmetry axis of the trap. The spectroscopy beam is aligned perpendicular to the trap axis. Previously, we demonstrated the feasibility of Doppler-free E2 spectroscopy, using the heteronuclear HD$^+$ for ease of experimentation [10]. A suitable continuous-wave laser system, with sufficient power and narrow linewidth, is a key instrument for the spectroscopy [28]. Further details
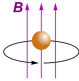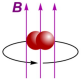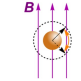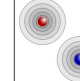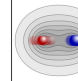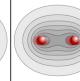
Main constants to be determined	Method and System							Reference	Row
	Classical		Quantum						
	Cyclotron motion		Electron spin resonance, QED theory	Laser spectroscopy, QED theory					
	p, ion	H_2^+, D^+	hydrogen-like ion	H, D	μH, μD	HD⁺	H_2^+		1
$\dfrac{m_p}{m_e}$	✓		✓					CODATA 2018	2
		✓		✓	✓	✓		[Alighanbari 23] & CODATA 2018	3
				✓	✓		✓	LSA 1: This work & CODATA 2018	4
$\dfrac{m_d}{m_p}$		✓						[Fink & Myers 21]	5
				✓	✓	✓	✓	LSA 2: This work & CODATA 2018	6
r_p, r_d				✓	✓			CODATA 2018	7
		✓		✓		✓	✓	LSA 3: This work & CODATA 2018	8
$r_p, r_d, \dfrac{m_p}{m_e}$		✓		✓	✓	✓	✓	LSA 4: This work & CODATA 2018	9
									10

TABLE I. **Overview of some approaches suitable for the determination of fundamental constants with high accuracy.** Check marks indicate a measurement required to obtain the constant in column 1 of the same row. The column highlighted in red indicates the contributions of the present work. (See text for details.) Note that the table is not comprehensive; for example, the charge radii r_p and r_d can also be determined by electron scattering. Row 10: schematic depictions of the systems used for the determinations. Orange ball: atomic ion, red ball: proton, blue ball: deuteron.

on the experimental technique are provided in the Methods section.

It is advantageous to select a transition whose spin structure is simple, as this allows the spin-averaged transition frequency to be obtained by effectively canceling the spin structure [29]. The transition should also yield a sufficient signal to enable the measurement of systematic effects to a desired level of accuracy. We found that these conditions are met for the $(v = 1, N = 0) \rightarrow (v' = 3, N' = 2)$ vibrational transition at a wavelength of 2.4 μm (124 THz), which we have previously studied in the Doppler-broadened regime. Here, v and N denote vibrational and rotational quantum numbers, respectively. Figure 1 b shows the spin structure of the energy levels. It is simple thanks to the fact that for zero or even rotational quantum numbers (so-called para-H_2^+), the two proton spins must be in a singlet total spin state, $I = 0$. This leaves as the only remaining spin interaction the electron-spin-rotation interaction, $h\, c_e(v, N)\, \mathbf{S_e} \cdot \mathbf{N}$. Here, c_e is the coupling coefficient, $\mathbf{S_e}$ is the electron spin operator and $\mathbf{N}$ is the rotational angular momentum operator. The possible spin en-
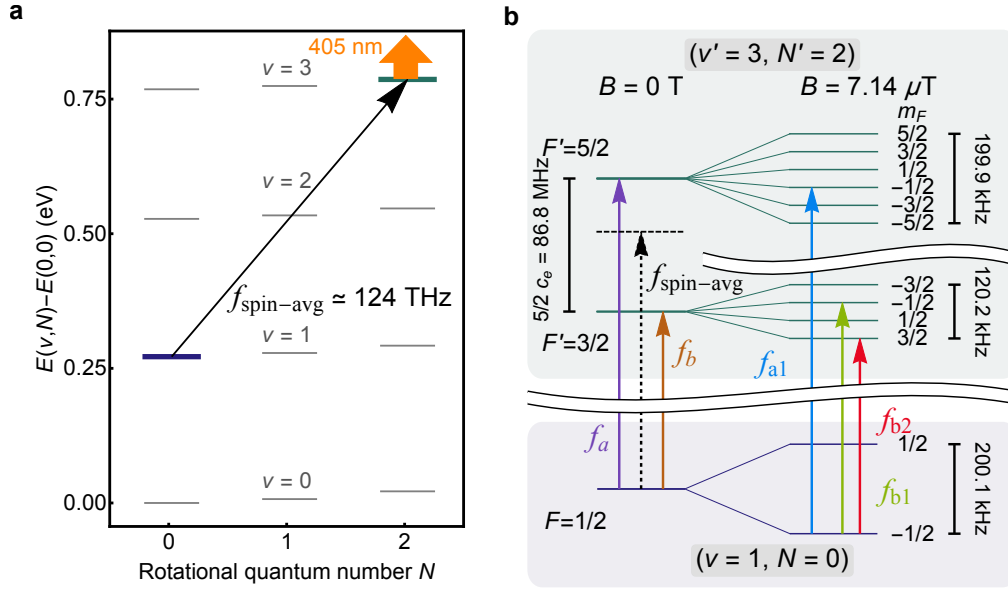
a

b

FIG. 1. **Energy levels of H_2^+ and transitions relevant to this work. a**: the lowest three rotational levels of the vibrational states $v = 0 - 3$. The studied transition $(v = 1, N = 0) \rightarrow (v' = 3, N' = 2)$ is shown by the black arrow, while the dissociation radiation is indicated by the orange arrow. **b**: spin (left) and Zeeman structure (right) of the two rovibrational levels addressed in the present study. The upper vibrational level $v' = 3$ comprises two states $F' = 3/2, 5/2$ that are split by 86.8 MHz by the interaction between rotation and the electron's magnetic moment. The two unperturbed spin components f_a and f_b of the transition are shown in purple and brown, respectively. The spin-averaged transition frequency $f_{\text{spin-avg}}$ is not directly measured, but is indicated schematically as a black-dashed arrow. On the right side, the Zeeman splittings are shown for the nominal field applied during spectroscopy, $B_{\text{REMPD}} = 7.14\,\mu\text{T}$. In order to show the Zeeman splitting, the vertical axis is broken at two positions. On the far right, the three colored arrows (blue, green and red) indicate the measured Zeeman components f_{a1}, f_{b1} and f_{b2}. F and F' are the total angular momentum of the molecule, m_F is the total angular momentum projection quantum number.

ergies are $h\,c_e(v, N)(F(F + 1) - N(N + 1) - 3/4)/2$, where the total angular momentum may take on the values $F = |N - 1/2|$ or $N + 1/2$. By virtue of the selection rules, the vibrational transition exhibits two spin components, namely f_a: $(F = 1/2 \rightarrow F' = 5/2)$ and f_b: $(F = 1/2 \rightarrow F' = 3/2)$. The frequencies of the two components are separated by $f_a - f_b = 5\,c_e(v, N)/2$. The spin-averaged transition frequency is $f_{\text{spin-avg}} = (3f_a + 2f_b)/5$.
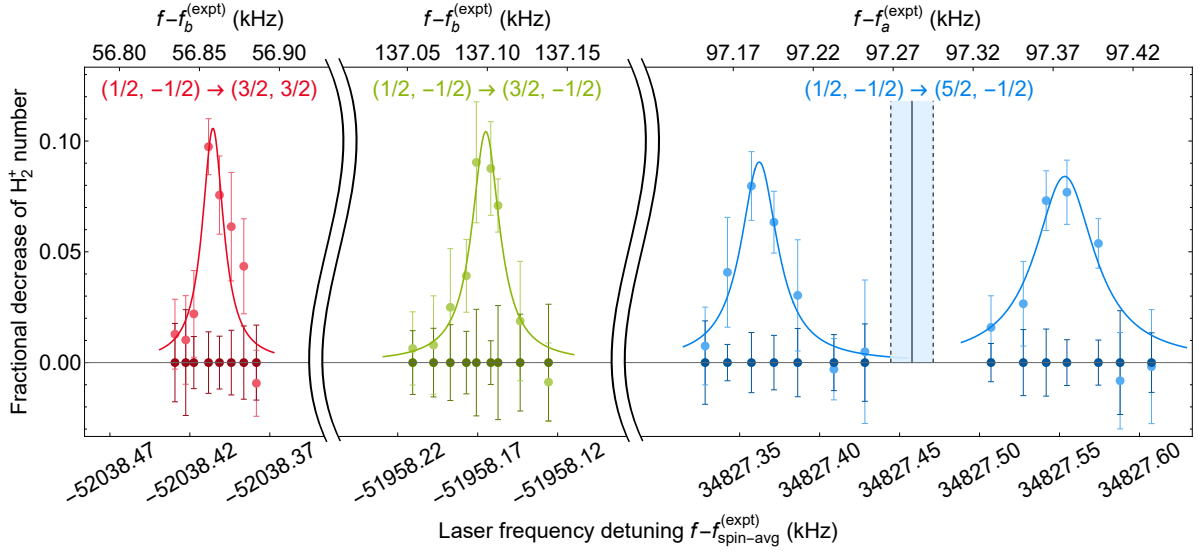
FIG. 2. **Zeeman components of the rovibrational transition measured under nominal operating conditions.** The three Zeeman components f_{b2}, f_{b1}, and f_{a1} (from left to right) of Fig. 1 b are shown with the same colours. The component f_{a1} (light blue) is split into a doublet by the Autler-Townes (AT) effect (see Methods). The deperturbed frequency and uncertainty range of this component are indicated by black full and dashed lines, respectively. We assume that also the Zeeman components of the other spin component (red and green) are AT-split, but did not measure the full AT doublets. The laser frequency detuning is given relative to different reference values in the top and the bottom abscissae. Top: reference values are the deperturbed transition frequencies of the respective spin component $f_a^{(\text{expt})}$ and $f_b^{(\text{expt})}$. Bottom: reference value is the adjusted spin-averaged transition frequency $f_{\text{spin-avg}}^{(\text{expt})}$. The colored curves are guides to the eye. For display purposes, the data is divided into bins and the average value of each bin is shown. For an individual component, the bin size is kept constant, but it may vary between different components. The vertical error bars are the standard error of the mean in the bin. The horizontal error bars are due to the uncertainty of the spectroscopy wave's frequency, and are smaller than the size of a data point (see Methods).

EXPERIMENT

In order to observe Doppler-free lines in H$_2^+$, we followed the protocol of our previous work on HD$^+$. We achieve Doppler-free spectroscopy at the expense of substantially more

effort than for HD^+, because the preparation of a large fraction of molecules in the lower spectroscopy level was not feasible. One data point in H_2^+ spectroscopy took ~ 5 hours of experimentation, while it took approximately 40 minutes in our study of the fourth overtone transition of HD^+ [7]. The successful data collection leading to complete lines was only possible thanks to the excellent long-term stability of our laser metrology system and trap apparatus.

An excerpt of the recorded spectra is displayed in Fig. 2. The narrowest linewidths observed were as low as $\simeq 6$ Hz (see Supplemental Material, Fig. A 4), corresponding to a line resolution of 2.2×10^{13}. This represents the highest published resolution in molecular spectroscopy to date, to the best of our knowledge. It is higher by a factor 7 compared to a cold-trapped-Sr_2 spectroscopy experiment, where a line resolution of 2.9×10^{12} was reported [30]. It is furthermore a factor of $\sim 10^6$ higher than the only previous two studies of rovibrational spectroscopy of a homonuclear molecular ion transition [10, 31]. The observed linewidths are due to a combination of power broadening, short exposure duration, finite laser linewidth and laser frequency instability.

In order to achieve low uncertainty, it is important to understand the Zeeman shifts. The theoretical Zeeman shifts have been discussed in ref. [10], ED Tab. 1-3. We performed the spectroscopy at a finite, but small magnetic field so that it was possible to interrogate specific Zeeman components while maintaining their shifts small.

Further shifts were also studied (see Methods, Sec. A 2). We present in Tab. II a summary of the determined shifts. Note that this is the first characterization of the systematic shifts of a rovibrational transition of a homonuclear molecular ion. The deperturbed transition frequencies are

$$f_a^{(\text{expt})} = 124\,487\,067\,172.9(6)_{\text{expt}} \text{ kHz },$$
$$f_b^{(\text{expt})} = 124\,486\,980\,347.5(8)_{\text{expt}} \text{ kHz }.$$

EXPERIMENT - THEORY COMPARISON

Spin structure. From our analysis, we obtain the spin-rotation coefficient $c_e^{(\text{expt})}(v' = 3, N' = 2) = 34\,730.18(10)_{\text{expt}}$ kHz . The most recent theoretical prediction is $c_e^{(\text{theor})}(v' = 3, N' = 2) = 34\,730.25(12)$ kHz [13]. The values are consistent. We may compare this agreement with previous results. An over-50-year-old measurement of five spin-rotation

5.3 Determination of the proton-electron mass ratio by high-accuracy laser spectroscopy of H_2^+

Effect	Component a1		Component b1		Component b2	
	$f_{a1,nom}^{(-)} - f_a^{(expt)}$ (kHz)	Uncertainty (kHz)	$f_{b1,nom} - f_b^{(expt)}$ (kHz)	Uncertainty (kHz)	$f_{b2,nom} - f_b^{(expt)}$ (kHz)	Uncertainty (kHz)
Zeeman shift	80.2	0.46	120.02	0.68	39.87	0.23
a.c. Stark (2.4 μm)	-0.33	0.38	-0.35	0.41	-0.72	0.84
a.c. Stark (313 nm)	0.29	0.08	0.31	0.08	0.52	0.13
RF trap shift	0.05	0.06	0.05	0.07	0.11	0.14
AT splitting	-0.1	0.01	0.	0.1	0.	0.1
Recoil	17.07	0.	17.07	0.	17.07	0.
Total	97.19	0.6	137.1	0.81	56.86	0.89

TABLE II. **Error budget of the overtone transition** $(v = 1, N = 0) \rightarrow (v' = 3, N' = 2)$ **frequency of H_2^+.** $f_a^{(expt)}$ and $f_b^{(expt)}$ are the two deperturbed spin component frequencies given in the text and $f_{a1,nom}^{(-)}$, $f_{b1,nom}$ and $f_{b2,nom}$ are the Zeeman components measured under nominal conditions shown in Figures 1 and 2. $f_{a1,nom}^{(-)}$ denotes the lower frequency component of the AT doublet. See Methods, Sec. A 2, for a detailed discussion of these effects.

coefficients in $(v = 4 \ldots 8, N = 2)$ levels [12] is also in agreement with the theory, but had substantially larger experimental uncertainties ($\simeq 1.5$ kHz). Very precisely measured hyperfine splittings in levels $(v = 4, 5, 6, N = 1)$ [9] agree with theoretical predictions within the 0.05 kHz theoretical uncertainties [13], but do not allow extracting c_e. Our measurement thus provides the most accurate determination of a spin structure coefficient of any MHI so far.

Spin-averaged frequency. The adjusted, deperturbed experimental spin-averaged

frequency is $f_{\text{spin-avg}}^{(\text{expt})} = 124\,487\,032\,442.69(0.95)_{\text{expt}}$ kHz . We included a correction for the recoil shift (17.1 kHz), as in our previous work [7]. The theoretical transition frequency is computed as described in Methods. In order to obtain a numerical value, a value for m_p/m_e must be assumed. CODATA 2018 provides such a value stemming only from Penning trap measurements (ESR and mass spectrometry), and it leads to

$$f_{\text{spin-avg}}^{(\text{theor})} = 124\,487\,032\,442.3(0.9)_{\text{QED}}(3.3)_{\text{CODATA18}} \text{ kHz .}$$

Very recently, CODATA 2022 provided a more accurate new value $[m_p/m_e]_{22}$, obtained by including also some previous data of HD^+ spectroscopy. Using this value yields

$$f_{\text{spin-avg}}^{(\text{theor})} = 124\,487\,032\,442.5(0.9)_{\text{QED}}(0.96)_{\text{CODATA22}} \text{ kHz .}$$ We point out that the two uncertainties in this number may be correlated. Both CODATA uncertainties are dominated by the uncertainty of the proton-electron mass ratio. Our experimental and theoretical values for $f_{\text{spin-avg}}$ are in agreement.

DISCUSSION

Frequency ratios. Ratios of transition frequencies of the same MHI species X, $f_i(X)/f_j(X)$ have been introduced in ref. [7], and for different species X and X' in ref. [8]. They are illustrative quantities for comparison between experiment and theory, benefitting from the independence of the theoretical ratios from the Rydberg constant and its uncertainty. Ratios of suitably selected pairs i and j additionally have a reduced sensitivity to the mass ratios and charge radii. Taking into account the present rovibrational frequency of H_2^+, $f_{\text{spin-avg}}(H_2^+) \equiv f_2(H_2^+)$ and our previously reported HD^+ vibrational frequencies $f_1(HD^+)$, $f_5(HD^+)$ [7], we find that a favourable choice is $\mathcal{R}_{5,2'} = f_5(HD^+)/f_2(H_2^+)$, where transition f_5 is the fourth vibrational overtone of HD^+ We compare the experimental and theoretical ratio by considering their fractional deviation. The result is

$$\left(\mathcal{R}_{5,2'}^{(\text{expt})} - \mathcal{R}_{5,2'}^{(\text{theor})} \right) / \mathcal{R}_{5,2'} = -2.4(8.0)_{\text{expt}}(0.9)_{\text{theor}}(1.)_{\text{CODATA18*}} \times 10^{-12}.$$

The combined uncertainty is 8.1×10^{-12}. For the frequency ratio $f_1(HD^+)/f_2(H_2^+)$ we obtain a similar good match,

$$\left(\mathcal{R}_{1,2'}^{(\text{expt})} - \mathcal{R}_{1,2'}^{(\text{theor})} \right) / \mathcal{R}_{1,2'} = 1.3(8.0)_{\text{expt}}(1.)_{\text{theor}}(3.)_{\text{CODATA18*}} \times 10^{-12}.$$

(The asterics indicate that the recent accurate value $[m_d/m_p]_{\text{FM21}}$ [14] was employed.) At an operational level, assuming the correctness of the theoretical predictions, the match indicates that our measurements performed on different species, at different epoch, and with in part differing equipment, are consistent.

Determination of fundamental constants. We may now determine some fundamental constants using least-squares adjustments (see SM for details). We do not perform a global analysis of all world data, a task that is the mandate of CODATA, but limit ourselves to more restricted analyses that already provide important insights. An overview of our analyses LSA 1 - 4 is presented in Tab. III. We focus on the CODATA 2018 adjustment since it does not include results from MHI spectroscopy, thus allowing a clearer comparison with the present results.

(1) The simplest analysis (LSA 1) consists in determining the proton-electron mass ratio. The CODATA 2018 Rydberg constant $R_{\infty,18}$ and the proton charge radius $r_{p,18}$ are input

						LSA with MHI data (CODATA 2018)					
Type	n	M	MHI input	mass ratio input	other input	$\triangle(m_p/m_e)$ $u(m_p/m_e)$	$\triangle(m_d/m_p)$ $u(m_d/m_p)$	$\triangle(cR_\infty)$,kHz $u(cR_\infty)$,kHz	$\triangle(r_p)$,fm $u(r_p)$,fm	$\triangle(r_d)$,fm $u(r_d)$,fm	Comment
1	4	4	$f_{2'}$	–	$R_{\infty,18}$, $r_{p,18}$	-1.4×10^{-8} 4.4×10^{-8}					Adjusted m_p/m_e to be compared with CODATA18 and with HD$^+$ & CODATA18
2	9	8	$f_{2'},f_1,f_5$	–	$R_{\infty,18}$, $r_{p,18}$, $r_{d,18}$	-2.0×10^{-8} 4.4×10^{-8}	1.2×10^{-10} 1.1×10^{-10}	-0.1 6.4	0.00000 0.0019	0.00000 0.00074	Adjusted m_d/m_p to be compared with $[m_d/m_p]_{FM21}$
3	12	10	$f_{2'},f_1,f_5$	$[m_d/m_p]_{FM21}$	H, H–D	-2.1×10^{-7} 1.0×10^{-6}	1.2×10^{-10} 4.4×10^{-9}	3.4×10^2 1.8×10^3	0.11 0.58	0.04 0.23	Adjusted m_p/m_e, R_∞, r_p to be compared with CODATA18
4	10	8	$f_{2'},f_1,f_5$	$[m_d/m_p]_{FM21}$	$R_{\infty,18}$, $r_{p,18}$, $r_{d,18}$	-1.8×10^{-8} 3.3×10^{-8}	1.2×10^{-10} 9.0×10^{-12}	-0.1 6.4	0.00000 0.0019	0.00000 0.00074	Adjusted m_p/m_e to be compared with CODATA18
			Reference values								
			CODATA 2022			$-4.\times10^{-9}$ 3.2×10^{-8}	-2.10×10^{-12} 8.4×10^{-12}	$-1.$ 3.6	0 0.00064	0 0.00027	
			CODATA 2018			0 1.1×10^{-7}	0 9.0×10^{-12}	$0.$ 6.4	0.0000 0.0019	0.00000 0.00074	
			Fink & Myers 2021, $[m_d/m_p]_{FM21}$				0 $9.\times10^{-12}$				
HD$^+$	7	7	f_1,f_5	–	$R_{\infty,18}$, $r_{p,18}$, $r_{d,18}$	-4.6×10^{-9} 3.7×10^{-8}		$0.$ 6.4	0.00000 0.0019	0.00000 0.00074	m_p/m_e is computed from adjusted μ_{pd}/m_e and $[m_d/m_p]_{FM21}$

TABLE III. **Least-squares adjustments (LSA) of fundamental constants.** See text for a discussion and SM for details. n is the number of input data, M is the number of adjusted constants. $f_{2'}$ is short-hand for the frequency measured in the present work. Columns 7-11 refer to the adjusted fundamental constants. An exception is LSA HD$^+$(bottom row), where μ_{pd}/m_e is adjusted (but not shown) and from it and $[m_d/m_p]_{FM21}$ the value $[m_p/m_e]_{HD+}$ is then computed. (LSA HD$^+$ concerns the molecule HD$^+$, and is given for reference.) For the other LSAs m_d/m_p is derived from the adjusted m_p/m_e and μ_{pd}/m_e. Also adjusted, but not shown, are the unknown theoretical corrections $\delta f^{(\text{theor})}$ to the currently available theoretical predictions $f^{(\text{theor})}$ of transition frequencies in MHI, of the 1s - 2s transition in hydrogen (H), and of the 1s - 2s hydrogen-deuterium isotope shift (H - D). $R_{\infty,18}$, $r_{p,18}$, $r_{d,18}$ denote the CODATA 2018 values. $\Delta(x)$ is the difference between the adjusted constant x and its CODATA 2018 value. $u(x)$ is the uncertainty of the adjusted x, obtained from the LSA. The row "CODATA 2022" displays as $\Delta(x)$ the values of the 2022 adjustment minus the 2018 adjustment values.

data of the adjustment, although they are not effectively adjusted. We recall that both values are derived by combining the results of H and μH spectroscopy. The spectroscopically determined value is

$$[m_p/m_e]_{\text{LSA1}} = 1836.152673416(44)\,.$$

It is consistent with three other values: (i) the CODATA 2018 value that relies mostly on an electron-g-factor measurement of hydrogen-like carbon, $[m_p/m_e]_{18} = 1836.15267343(11)$ [25], whose uncertainty is 2.5 times the present one. (ii) the CODATA 2022 value $[m_p/m_e]_{22} = 1836.152673426(32)$, which is based also on data from HD$^+$ spectroscopy;

(iii) the value $[m_p/m_e]_{HD^+} = 1836.152673425(37)$ (LSA HD$^+$ in Tab. III), determined from our HD$^+$ vibrational data, and $R_{\infty,18}$, $r_{p,18}$, $r_{d,18}$, and $[m_d/m_p]_{FM21}$. It should be emphasized that the two CODATA determinations, too, rely on high-accuracy QED calculations.

The two values $[m_p/m_e]_{LSA1}$ and $[m_p/m_e]_{HD^+}$ from MHI spectroscopy are not independent in a fundamental sense, since they originate from the same apparatus, researchers, theoretical formalism and numerical routines (and are based on the same H/D, μH data/theory). The two corresponding uncertainties are partially correlated. Nevertheless, the agreement represents a powerful consistency test of our theoretical and experimental techniques.

(2) LSA 2 combines the present H$_2^+$ data with our previous HD$^+$ rovibrational data, CODATA values $R_{\infty,18}$, $r_{p,18}$, and $r_{d,18}$, but does not include mass data. Spectroscopic values both for m_p/m_e and m_d/m_p are obtained. The value of the latter is

$$[m_d/m_p]_{LSA2} = 1.99900750139(11).$$

It is in agreement with the independent value $[m_d/m_p]_{FM21} = 1.999007501272(9)$ from mass spectrometry [14].

(3) With LSA 3 we check whether R_∞, r_p, r_d, m_p/m_e can be obtained with a useful level of uncertainty without relying on input data derived from muonic hydrogen experiments. Therefore, instead of CODATA 2018 fundamental constants, we use specific data from H and D spectroscopy, i.e. on the 1s - 2s transition [32–34], as supplementary input, in addition to the accurate $[m_d/m_p]_{FM21}$. Note that the H - D isotope shift data furnishes, by itself, a highly accurate value of $r_d^2 - r_p^2$ [32]. As a result of LSA 3, the proton radius is determined to be $[r_p]_{LSA3} = 0.95(58)$ fm. Its uncertainty is not competitive. The weakness of LSA 3 can be traced to the current experimental uncertainties and the similar fractional sensitivities of the MHI frequencies on the fundamental constants (see [8] for details).

(4) In LSA 4, an extension of LSA 2, we combine our MHI data with $[m_d/m_p]_{FM21}$, $R_{\infty,18}$, $r_{p,18}$, and $r_{d,18}$. The adjusted proton-electron mass ratio is slightly more accurate than in LSA 1, with an uncertainty three times lower than in CODATA 2018. The value is consistent with the CODATA 2022 value (which includes f_1 in the adjustment).

CONCLUSION

This work is the first demonstration of high-accuracy vibrational spectroscopy of a homonuclear molecular ion and it permitted introducing H_2^+ into the field of fundamental constants, resulting in the first spectroscopic determination of the proton-electron mass ratio at a state-of-the-art level. The value is in agreement but exhibits more than two-fold lower uncertainty than the value obtained from the g-factor of hydrogen-like carbon. Our value is also in agreement with the m_p/m_e value obtained by combining HD^+ laser spectroscopy and a mass spectrometric determination of m_d/m_p.

Furthermore, we performed a stringent test of a specific aspect of MHI spin structure theory, namely the spin-rotation coupling. The obtained experiment-theory agreement supports the suitability of the application of spin structure theory for the analysis of experimental HD^+ data.

Additionally, we deduced a new, spectroscopically determined value for the deuteron-proton mass ratio. This value relies on spectroscopy and the bound-state QED theory of the hydrogen atom, the muonic hydrogen atom, and the MHI. The most accurate value for comparison is from an experiment in which an H_2^+ ion and a deuteron were in classical motion in a Penning trap, with only minor quantum corrections applied in the ratio extraction [14]. The two independent m_d/m_p values agree at a fractional level of 5.4×10^{-11} ; therefore this represents a strong test of the correct description of dynamics in the quantum and classical realm: the mass values in the Schrödinger equation are the same as those of Newtonian physics.

Finally, the finding that two ratios of experimental and theoretical frequencies of HD^+ and H_2^+ agree at the 8.1×10^{-12} level (limited by the present experimental uncertainty) ranks among the most accurate comparisons of a theoretical prediction and an experimental quantity. The uncertainty is within a factor 8 of the most accurate experiment-theory comparison, the g-factor of the bare electron [35]. Near-future experimental improvements may enable the reduction of uncertainties associated with particular ratios to a similar level [8].

OUTLOOK

Within the theme of MHI research, it is desirable to pursue even higher accuracy on H_2^+ and furthermore extension to the remaining homonuclear ions, D_2^+ and T_2^+. Indeed, according to a new analysis [8] important improvements in the accuracy of mass ratios (two-hundred-fold compared to CODATA 2022) and proton, deuteron and triton nuclear charge radii appear feasible. Our results (Methods, Sec. 2.g) indicate that a more than tenfold lower experimental uncertainty is possible with our methods, by removing the uncertainty associated with the limited number of measured AT doublets and by an improved determination of a.c. Stark shifts. We showed that by selecting a suitable transition and measuring all its spin components, it is possible to remove the effect of spin structure entirely in the determination of the spin-averaged frequency, thus avoiding the use of spin theory results. This will become an important advantage compared to HD^+. MHI spectroscopy at even lower uncertainty levels could become possible with quantum logic spectroscopy [36], as proposed early on [37]. This technique has already been applied to molecular ions [38–41] and most recently to H_2^+ [42]. Beyond MHI, our demonstration also supports efforts of utilizing homonuclear diatomic ions for further fundamental physics studies, in particular for testing the time-independence of the electron-nuclear mass ratio [37, 43–45].

The anticipated future improvement of the proton-electron mass ratio may have a substantial impact on ESR spectrometry in Penning traps. There, one measures the ESR frequency $\nu_L(B)$ and the cyclotron frequency $\nu_c(B)$ of one-electron ions in the same magnetic field B. These ions can be hydrogen-like atomic ions or MHI, with mass m_{ion}, charge q_{ion}, and bound-electron g-factor g_{ion}. Combining the two frequencies provides $m_e/m_{ion} = (g_{ion}/2)(e/q_{ion})(\nu_c(B)/\nu_L(B))$. The proton-electron mass ratio $[m_p/m_e]_{MHI}$ from MHI vibrational spectroscopy may be employed to develop the expression into $g_{ion} = 2[m_e/m_p]_{MHI}(m_p/m_{ion})(q_{ion}/e)(\nu_L/\nu_c)$. Since the baryon mass ratio m_p/m_{ion} can be measured separately and with high accuracy by Penning trap cyclotron mass spectrometry, this expression then allows to compare experimental values $g_{ion}^{(expt)}$ with predicted values $g_{ion}^{(theor)}$, for example for testing strong-field QED. Since already with the current MHI theory, near-future MHI vibrational spectroscopy may achieve $u_r([m_e/m_p]_{MHI}) \simeq 5 \times 10^{-14}$ [8], g-factor determinations and g-factor-based QED tests may in principle become possible at the same level. Alternatively, using theoretical g-factors, mass ratios m_p/m_{ion} may be determined

without the necessity of conducting a measurement on the proton.

A future test of CPT symmetry consists in the comparison of a single vibrational transition frequency of anti-H_2^+ with the same in normal H_2^+. In refs. [1, 3, 10] the motivation and accuracy potential for such a test have been discussed. The present work represents progress towards this goal, since E2 spectroscopy is equally applicable to anti-H_2^+. While the present work was performed in a radiofrequency trap, future anti-H_2^+ spectroscopy might be performed in a Penning trap. The recent demonstration of long-term trapping and non-destructive spectroscopy of HD^+ in a Penning trap supports such an approach [46]. More sophisticated Penning trap techniques are under development [47].

ACKNOWLEDGMENTS

AUTHOR CONTRIBUTIONS

S.A. and M.R.S. maintained the apparatus, performed the experiments and analysed the data. S.S. performed theoretical analyses, and mainly wrote the paper. V.I.K. performed ab initio calculations. S.A., M.R.S., S.S. discussed the data, interpretations and text.

COMPETING INTERESTS

The authors declare no competing financial or non-financial interests.

––––––––––––––––––

[1] S. Schiller, Precision spectroscopy of molecular hydrogen ions: an introduction, Contemporary Physics 63 (2022) 247–279. `doi:10.1080/00107514.2023.2180180`.

[2] H. Dehmelt, Economic synthesis and precision spectroscopy of anti-molecular hydrogen ions in Paul trap, Physica Scripta T59 (1995) 423–423. `doi:10.1088/0031-8949/1995/t59/060`.

[3] E. G. Myers, CPT tests with the antihydrogen molecular ion, Phys. Rev. A 98 (2018) 010101. `doi:10.1103/PhysRevA.98.010101`.

[4] S. Alighanbari, G. S. Giri, F. L. Constantin, V. I. Korobov, S. Schiller, Precise test of quantum electrodynamics and determination of fundamental constants with HD^+ ions, Nature 581 (2020) 152 – 158. `doi:10.1038/s41586-020-2261-5`.

[5] S. Patra, M. Germann, J.-P. Karr, M. Haidar, L. Hilico, V. I. Korobov, F. M. J. Cozijn, K. S. E. Eikema, W. Ubachs, J. C. J. Koelemeij, Proton-electron mass ratio from laser spectroscopy of HD^+ at the part-per-trillion level, Science 369 (2020) 1238–1241. `doi:10.1126/science.aba0453`.

[6] I. V. Kortunov, S. Alighanbari, M. G. Hansen, G. S. Giri, V. I. Korobov, S. Schiller, Proton-electron mass ratio by high-resolution optical spectroscopy of ion ensembles in the resolved-carrier regime, Nat. Phys. 17 (2021) 569–573. `doi:10.1038/s41567-020-01150-7`.

[7] S. Alighanbari, I. V. Kortunov, G. S. Giri, S. Schiller, Test of charged baryon interaction with high-resolution vibrational spectroscopy of molecular hydrogen ions, Nat. Phys. 19 (2023) 1263 – 1269. `doi:10.1038/s41567-023-02088-2`.

[8] S. Schiller, J.-P. Karr, Prospects for the determination of fundamental constants with beyond-state-of-the-art uncertainty using molecular hydrogen ion spectroscopy, Phys. Rev. A 109 (2024) 042825. `doi:10.1103/PhysRevA.109.042825`.

[9] S. C. Menasian, High resolution study of the $(F\,F_2) = (3/2\,1/2) \rightarrow (1/2\,1/2)$ HFS transitions in stored H_2^+ molecular ions, Ph.D. thesis, University of Washington (1973).

[10] M. R. Schenkel, S. Alighanbari, S. Schiller, Laser spectroscopy of a rovibrational transition in the molecular hydrogen ion H_2^+, Nature Physics 20 (2024) 383–388. `doi:10.1038/s41567-023-02320-z`.

[11] I. Doran, N. Hölsch, M. Beyer, F. Merkt, Zero-Quantum-Defect Method and the Fundamental Vibrational Interval of H_2^+, Phys. Rev. Lett. 132 (2024) 073001. `doi:10.1103/PhysRevLett.132.073001`.

[12] K. B. Jefferts, Hyperfine Structure in the Molecular Ion H_2^+, Phys. Rev. Lett. 23 (1969) 1476–1478. `doi:10.1103/PhysRevLett.23.1476`.

[13] M. Haidar, V. I. Korobov, L. Hilico, J.-P. Karr, Higher-order corrections to spin-orbit and spin-spin tensor interactions in hydrogen molecular ions: Theory and application to H_2^+, Phys. Rev. A 106 (2022) 022816. `doi:10.1103/PhysRevA.106.022816`.

[14] D. J. Fink, E. G. Myers, Deuteron-to-Proton Mass Ratio from Simultaneous Measurement of the Cyclotron Frequencies of H_2^+ and D^+, Phys. Rev. Lett. 127 (2021) 243001. `doi:`

10.1103/PhysRevLett.127.243001.

[15] V. I. Korobov, J.-P. Karr, Rovibrational spin-averaged transitions in the hydrogen molecular ions, Phys. Rev. A 104 (2021) 032806. doi:10.1103/PhysRevA.104.032806.

[16] V. A. Yerokhin, K. Pachucki, V. Patkós, Theory of the Lamb Shift in Hydrogen and Light Hydrogen-Like Ions, Annalen der Physik 531 (2019) 1800324. doi:10.1002/andp.201800324.

[17] J.-P. Karr, L. Hilico, J. C. J. Koelemeij, V. I. Korobov, Hydrogen molecular ions for improved determination of fundamental constants, Phys. Rev. A 94 (2016) 050501. doi:10.1103/PhysRevA.94.050501.

[18] S. Sturm, F. Köhler, J. Zatorski, A. Wagner, Z. Harman, G. Werth, W. Quint, C. H. Keitel, K. Blaum, High-precision measurement of the atomic mass of the electron, Nature 506 (2014) 467–470. doi:10.1038/nature13026.

[19] G. Paz, An introduction to NRQED, Modern Physics Letters A 30 (2015) 1550128. doi:10.1142/S021773231550128X.

[20] A. Carrington, C. A. Leach, R. E. Moss, T. C. Steimle, M. R. Viant, Y. D. West, Microwave electronic spectroscopy, electric field dissociation and photofragmentation of the H_2^+ ion, J. Chem. Soc., Faraday Trans. 89 (1993) 603–614. doi:10.1039/FT9938900603.

[21] A. Carrington, C. A. Leach, M. R. Viant, Nuclear hyperfine structure in the electronic millimetre wave spectrum of H_2^+, Chemical Physics Letters 206 (1993) 77–82. doi:10.1016/0009-2614(93)85520-X.

[22] A. D. J. Critchley, A. N. Hughes, I. R. McNab, Direct measurement of a pure rotation transition in H_2^+, Phys. Rev. Lett. 86 (2001) 1725–1728. doi:10.1103/PhysRevLett.86.1725.

[23] P. W. Arcuni, Z. W. Fu, S. R. Lundeen, Energy difference between the ($\nu = 0$, $R = 1$) and the ($\nu = 0$, $R = 3$) states of H_2^+, measured with interseries microwave spectroscopy of H_2 Rydberg states, Phys. Rev. A 42 (1990) 6950–6953. doi:10.1103/PhysRevA.42.6950.

[24] C. Haase, M. Beyer, C. Jungen, F. Merkt, The fundamental rotational interval of para-H_2^+ by MQDT-assisted Rydberg spectroscopy of H_2, The Journal of Chemical Physics 142 (2015) 064310. doi:10.1063/1.4907531.

[25] F. Köhler, S. Sturm, A. Kracke, G. Werth, W. Quint, K. Blaum, The electron mass from g-factor measurements on hydrogen-like carbon $^{12}C^{5+}$, At. Mol. Opt. Phys. 48 (2015) 144032. doi:10.1088/0953-4075/48/14/144032.

[26] V. I. Korobov, P. Danev, D. Bakalov, S. Schiller, Laser-stimulated electric quadrupole transitions in the molecular hydrogen ion H$_2^+$, Phys. Rev. A 97 (2018) 032505. `doi:10.1103/PhysRevA.97.032505.`

[27] P. Blythe, B. Roth, U. Fröhlich, H. Wenz, S. Schiller, Production of ultracold trapped molecular hydrogen ions, Phys. Rev. Lett. 95 (2005) 183002. `doi:10.1103/PhysRevLett.95.183002.`

[28] M. R. Schenkel, V. Vogt, S. Schiller, subm.

[29] S. Schiller, V. I. Korobov, Canceling spin-dependent contributions and systematic shifts in precision spectroscopy of molecular hydrogen ions, Phys. Rev. A 98 (2018) 022511. `doi:10.1103/PhysRevA.98.022511.`

[30] K. H. Leung, B. Iritani, E. Tiberi, I. Majewska, M. Borkowski, R. Moszynski, T. Zelevinsky, Terahertz vibrational molecular clock with systematic uncertainty at the 10^{-14} level, Phys. Rev. X 13 (2023) 011047. `doi:10.1103/PhysRevX.13.011047.`

[31] M. Germann, X. Tong, S. Willitsch, Observation of dipole-forbidden transitions in sympathetically cooled, state-selected, homonuclear diatomic molecular ions, Nat. Phys. 10 (2014) 820–824. `doi:10.1038/nphys3085.`

[32] C. G. Parthey, A. Matveev, J. Alnis, R. Pohl, T. Udem, U. D. Jentschura, N. Kolachevsky, T. W. Hänsch, Precision Measurement of the Hydrogen-Deuterium $1S - 2S$ Isotope Shift, Phys. Rev. Lett. 104 (2010) 233001. `doi:10.1103/PhysRevLett.104.233001.`

[33] C. G. Parthey, A. Matveev, J. Alnis, B. Bernhardt, A. Beyer, R. Holzwarth, A. Maistrou, R. Pohl, K. Predehl, T. Udem, T. Wilken, N. Kolachevsky, M. Abgrall, D. Rovera, C. Salomon, P. Laurent, T. W. Hänsch, Improved Measurement of the Hydrogen $1S - 2S$ Transition Frequency, Phys. Rev. Lett. 107 (2011) 203001. `doi:10.1103/PhysRevLett.107.203001.`

[34] A. Matveev, C. G. Parthey, K. Predehl, J. Alnis, A. Beyer, R. Holzwarth, T. Udem, T. Wilken, N. Kolachevsky, M. Abgrall, D. Rovera, C. Salomon, P. Laurent, G. Grosche, O. Terra, T. Legero, H. Schnatz, S. Weyers, B. Altschul, T. W. Hänsch, Precision measurement of the hydrogen $1s-2s$ frequency via a 920-km fiber link, Phys. Rev. Lett. 110 (2013) 230801. `doi:10.1103/PhysRevLett.110.230801.`

[35] X. Fan, T. G. Myers, B. A. D. Sukra, G. Gabrielse, Measurement of the Electron Magnetic Moment, Phys. Rev. Lett. 130 (2023) 071801. `doi:10.1103/PhysRevLett.130.071801.`

[36] P. O. Schmidt, T. Rosenband, C. Langer, W. M. Itano, J. C. Bergquist, D. J. Wineland, Spectroscopy using quantum logic, Science 309 (2005) 749–752. `doi:10.1126/science.1114375.`

[37] S. Schiller, V. Korobov, Test of time-dependence of the electron and nuclear masses with ultracold molecules, Phys. Rev. A 71 (2005) 032505. `doi:10.1103/PhysRevA.71.032505`.

[38] F. Wolf, Y. Wan, J. Heip, F. Gebert, C. Shi, P. Schmidt, Non-destructive state detection for quantum logic spectroscopy of molecular ions, Nature 530 (2016) 457–460. `doi:10.1038/nature16513`.

[39] C. Chou, C. Kurz, D. Hume, P. Plessow, D. R. Leibrandt, D. Leibfried, Preparation and coherent manipulation of pure quantum states of a single molecular ion, Nature 545 (2017) 203–207. `doi:10.1038/nature22338`.

[40] M. Sinhal, Z. Meir, K. Najafian, G. Hegi, S. Willitsch, Quantum-nondemolition state detection and spectroscopy of single trapped molecules, Science 367 (2020) 1213–1218. `doi:10.1126/science.aaz9837`.

[41] C. W. Chou, A. L. Collopy, C. Kurz, Y. Lin, M. E. Harding, P. N. Plessow, T. Fortier, S. Diddams, D. Leibfried, D. R. Leibrandt, Frequency-comb spectroscopy on pure quantum states of a single molecular ion, Science 367 (2020) 1458–1461. `doi:10.1126/science.aba3628`.

[42] D. Holzapfel, F. Schmid, N. Schwegler, O. Stadler, M. Stadler, J. Home, D. Kienzler, Quantum logic spectroscopy of the hydrogen molecular ion, in: Frühjahrstagung der Deutschen Physikalischen Gesellschaft, Freiburg, 2024.
URL `https://www.dpg-verhandlungen.de/year/2024/conference/freiburg/part/q/session/26/contribution/6`

[43] M. Kajita, G. Gopakumar, M. Abe, M. Hada, M. Keller, Test of m_p/m_e changes using vibrational transitions in N_2^+, Phys. Rev. A 89 (2014) 032509. `doi:10.1103/PhysRevA.89.032509`.

[44] D. Hanneke, R. A. Carollo, D. A. Lane, High sensitivity to variation in the proton-to-electron mass ratio in $O_2{}^+$, Phys. Rev. A 94 (2016) 050101. `doi:10.1103/PhysRevA.94.050101`.

[45] F. Wolf, J. C. Heip, M. J. Zawierucha, C. Shi, S. Ospelkaus, P. O. Schmidt, Prospect for precision quantum logic spectroscopy of vibrational overtone transitions in molecular oxygen ions, New Journal of Physics 26 (2024) 013028. `doi:10.1088/1367-2630/ad1ad3`.

[46] C. M. König, F. Heiße, J. Morgner, T. Sailer, B. Tu, K. Blaum, S. Schiller, S. Sturm, Hyperfine Spectroscopy of Single Molecular Hydrogen Ions in a Penning Trap at ALPHATRAP, in: International Conference on Precision Physics of Simple Atomic Systems, 2022.
URL `https://psas.fuw.edu.pl/program/`

[47] J. M. Cornejo, R. Lehnert, M. Niemann, J. Mielke, T. Meiners, A. Bautista-Salvador, M. Schulte, D. Nitzschke, M. J. Borchert, K. Hammerer, S. Ulmer, C. Ospelkaus, Quantum logic inspired techniques for spacetime-symmetry tests with (anti-)protons, New Journal of Physics 23 (2021) 073045. `doi:10.1088/1367-2630/ac136e`.

[48] J.-P. Karr, S. Patra, J. Koelemeij, J. Heinrich, N. Silltoe, A. Douillet, L. Hilico, Hydrogen molecular ions: new schemes for metrology and fundamental physics tests, in: F. Riehle (Ed.), 8th Symp. on Frequency Standards and Metrology 2015, Vol. 723 of Journal of Physics: Conference Series, 2016, p. 012048. `doi:10.1088/1742-6596/723/1/012048`.

[49] S. Schiller, D. Bakalov, A. K. Bekbaev, V. I. Korobov, Static and dynamic polarizability and the Stark and blackbody-radiation frequency shifts of the molecular hydrogen ions H_2^+, HD^+, and D_2^+, Phys. Rev. A 89 (2014) 052521. `doi:10.1103/PhysRevA.89.052521`.

[50] S. H. Autler, C. H. Townes, Stark effect in rapidly varying fields, Phys. Rev. 100 (1955) 703–722. `doi:10.1103/PhysRev.100.703`.

[51] J. Qi, G. Lazarov, X. Wang, L. Li, L. M. Narducci, A. M. Lyyra, F. C. Spano, Autler-Townes Splitting in Molecular Lithium: Prospects for All-Optical Alignment of Nonpolar Molecules, Phys. Rev. Lett. 83 (1999) 288–291. `doi:10.1103/PhysRevLett.83.288`.

[52] J. Kim, J. S. Lim, H.-R. Noh, S. K. Kim, Experimental Observation of the Autler-Townes Splitting in Polyatomic Molecules, J. Phys. Chem. Lett. 11 (2020) 6791–6795. `doi:10.1021/acs.jpclett.0c01918`.

[53] J.-P. Karr, V. I. Korobov, L. Hilico, Vibrational spectroscopy of H_2^+: Precise evaluation of the Zeeman effect, Phys. Rev. A 77 (2008) 062507. `doi:10.1103/PhysRevA.77.062507`.

[54] D. Bakalov, V. Korobov, S. Schiller, Magnetic field effects in the transitions of the HD^+ molecular ion and precision spectroscopy, J. Phys. B: At. Mol. Opt. Phys. 44, 025003 (2011); doi: 10.1088/0953-4075/44/2/025003; Corrigendum, J. Phys. B: At. Mol. Opt. Phys. 45 (2012) 049501. `doi:10.1088/0953-4075/45/4/049501`.

Appendix A: Methods

1. Details of the experiment

We employ the same apparatus that we used in our previous work [10] to perform laser spectroscopy of an E2 transition in H_2^+ and HD^+. We prepare a cluster of trapped and sympathetically cooled molecular ions, where the sympathetic cooling is provided by the Coulomb interaction between the molecular ions and the three dimensional cluster of laser cooled Be^+ ions. By loading a small number of molecular ions, they arrange as an ion chain extending along the symmetry axis of the ion trap. The loading occurs by electron impact ionization from background gas. When the direction of propagation of the spectroscopy beam is perpendicular to the chain, a Doppler-free profile can be observed [7].

A partial state preparation of the trapped H_2^+ ions is carried out by dissociating those in excited vibrational levels $v \geq 2$ [10], using two lasers at 313 nm and 405 nm. We emphasize that our method does not prepare the population in a specific rotational level.

Following the state preparation, the number of trapped H_2^+ ions is determined by recording the beryllium fluorescence signal accompanying the transverse secular excitation of H_2^+, as a function of excitation frequency. The peak strength of this secular spectrum is proportional to the number of trapped ions. Next, the MHI are subjected to resonance-enhanced, multi-photon dissociation (REMPD). It comprises the excitation of the spectroscopy transition by an optical parametric oscillator (OPO) wave and the dissociation from the upper spectroscopy level by a 405 nm laser wave. To prevent a light shift induced by the dissociation laser, an interleaved shuttering scheme is employed. The cycle is concluded with an assessment of the remaining trapped H_2^+ ions. Subsequent cycles alternate between spectroscopy and background measurements (in which the spectroscopy laser is blocked) until sufficient statistics has been gathered. Between cycles, the ion cluster is purged of ions other than Be^+ and a new H_2^+ ensemble is loaded to ensure that the lower spectroscopy level has sufficient population. Throughout the REMPD, a magnetic field of $B_{\mathrm{REMPD}} \simeq 7.14(4)\ \mu T$ was applied, determined as explained in Sec. A 2 g. The spectroscopic signal is derived by comparing the number of trapped H_2^+ ions before and after REMPD. This is computed as the normalized decrease in ion number.

The spectroscopy laser system has been described previously [10]. We use the OPO's idler

wave as the spectroscopy wave, that is stabilized in frequency by referencing it to an ultra-stable optical frequency comb [28]. The upper-bound linewidth of the idler wave depends on the reference laser employed for the optical frequency comb. Over the course of the data acquisition, two different reference lasers were employed. Characterization showed that they produce a spectroscopy wave linewidth of approximately 5 Hz or 20 Hz, respectively, on timescales of $1 - 10^3$ s. The measurements acquired under nominal conditions were taken with a 20 Hz linewidth, while some systematic measurements (see SM) were obtained with a 5 Hz spectroscopy wave linewidth. Since this linewidth is moderately smaller than the observed linewidths, it appears to contribute to the observed molecular transition linewidths. For long-term frequency stability, the optical frequency comb is referenced to a hydrogen maser. Furthermore, we compare our hydrogen maser with the national standard via Global Navigation Satellite System (GNSS), thereby ensuring SI-traceability of the spectroscopy wave's frequency. The combined frequency error of the spectroscopy wave for timescales of one REMPD cycle is ≤ 1 Hz, or $\leq 1 \times 10^{-14}$ in relative terms. This includes fluctuations of the laser, statistical errors of the frequency comb measurement and maser frequency corrections (see Sec. A 2 f).

We deliberately performed a blind experimental search of the transitions, using as input information a value of $f_{\text{spin−avg}}^{(\text{theor})}$ with an added offset that turned out to be approximately 80 kHz after unblinding. The narrow linewidth of the transitions and the large Zeeman shifts of the components rendered their discovery tedious. $f_{\text{spin−avg}}^{(\text{theor})}$ was disclosed only after completion of all measurements. Its value was taken into account in order to identify the observed transitions, a necessary step for performing the complete analysis.

2. Systematics of the H_2^+ E2 transition: experiment

We have measured all systematics effects that we believe to be of significant magnitude compared to our spectroscopic resolution. For each shift, the measurements have been done on a subset of the three Zeeman components f_{a1}, f_{b1} and f_{b2}. Figures of the corresponding lines are displayed in the SM. In total, we have measured 11 individual lines, 4 of which under nominal conditions (Fig. 2). The remaining lines were Zeeman components perturbed by a single parameter setting (a laser intensity or the trap's RF amplitude). To evaluate all systematic effects as well as $f_{\text{spin-avg}}^{(\text{expt})}$ and $c_{\text{e}}^{(\text{expt})}$ we performed an adjustment to all observed

lines (see Sec. A 2). Below, we first enumerate the considered shifts and subsequently discuss the adjustment.

a. Zeeman shift

In order to determine the Zeeman shift of the components, we rely on theoretical results [29, 48]. The three measured components have substantial linear and small quadratic shifts. The predicted shift coefficients are $c_{\mathrm{lin},a1} = 11.2\,\mathrm{kHz}/\mu\mathrm{T}$, $c_{\mathrm{lin},b1} = 16.8\,\mathrm{kHz}/\mu\mathrm{T}$, $c_{\mathrm{lin},b2} = 5.6\,\mathrm{kHz}/\mu\mathrm{T}$ and $c_{\mathrm{quad},a1} = 2.2\,\mathrm{Hz}/(\mu\mathrm{T})^2$, $c_{\mathrm{quad},b1} = -2.2\,\mathrm{Hz}/(\mu\mathrm{T})^2$, $c_{\mathrm{quad},b2} = -1.4\,\mathrm{Hz}/(\mu\mathrm{T})^2$. In Sec. A 2 g we use these coefficients as input parameters in the determination of the Zeeman shifts, and treat the magnetic field value B as an adjustable parameter. The adjusted value $B_{\mathrm{REMPD}} \simeq 7.14(4)\,\mu\mathrm{T}$ is in agreement with, but more precise than, the value determined in our previous spectroscopy experiments on HD^+.

b. a.c. and d.c. Stark shifts

During the REMPD, two laser waves were present: the spectroscopy wave (2.4 μm) and the Doppler cooling wave (313 nm). These cause a.c. Stark shifts (light shifts) of the transition frequencies.

We have therefore measured the component f_{a1} at two different intensities of the spectroscopy wave (SM, Fig. 2). The a.c. Stark shift of other components are determined theoretically relative to this measurement by making use of the ratios of theoretically calculated polarizabilities (see Sec. A 2 g).

We remark that alternatively, an estimate for the shift can be obtained from the theoretical polarisabilities [49] and an approximate value for the spectroscopy wave intensity. This estimate gives maximum 2.4-μm-light shifts on the order of $-60\,\mathrm{Hz}$ for both components f_a and f_b, consistent with our observation, but one order smaller than the bounds resulting from our evaluation (see Tab. II). However, we take a conservative approach, relying more on our experimental data.

Regarding the shift caused by the 313 nm wave, we have measured two components, f_{a1} and f_{b1}, at three intensities each. The more detailed investigation of this shift was motivated by the unexpectedly large observed dependence on 313 nm wave intensity. For this wave,

we similarly use theoretical polarizabilities to infer the shifts not directly measured.

In addition, we assume a linear dependence of the transition frequencies on both wave intensities, with common sensitivity parameters k_{313}, $k_{2.4}$ for all components (see Sec. A 2 g).

We have not measured the shift of the transition frequency due to a spatial offset of the H_2^+ ensemble relative to the nominal location in the trap. This effect is expected to be negligible, given that the trap is well compensated and that the residual static electric field is should be small. This expectation is supported by the fact that we have previously investigated the d.c. Stark effect in HD^+ E2 transitions and have not resolved any shift at the level of 90 Hz [10], and that the static polarizability of the present H_2^+ transition is more than two orders of magnitude smaller than that of the HD^+ transition [49]. For these reasons, we expect the trap offset effect to be negligible and assign it zero value and uncertainty.

c. RF trap shift

We have measured the transition frequency f_{a1} at two different trap RF amplitudes. In contrast to HD^+, where for an E2 transition we observed shifts of approximately 1.2 kHz for two equivalent Zeeman components of the studied spin component [10], here we did not resolve a shift. While a possible shift would increase with increasing RF amplitude, we were unable to perform measurements at RF amplitudes larger or smaller than those presented, because the background loss of the trapped H_2^+ ensemble then increases. The non-observation of a shift confirms our earlier hypothesis [10] that the trap-field induced shift is smaller for homonuclear MHIs compared to heteronuclear ones, due to the absence of off-resonant electric dipole coupling between each spectroscopy level and other rovibrational levels. However, electric dipole couplings to excited electronic states of H_2^+ are nonzero, therefore a shift could still occur, albeit of much smaller magnitude. Therefore, we model the RF trap shift, similarly to the a.c. Stark shifts above, by the use of theoretical polarizabilities, an overall sensitivity parameter k_{RF} and a quadratic dependence on the trap's RF amplitude. The quadratic dependence is known from previous experiments.

d.   Autler-Townes (AT) splitting (or a.c. Stark splitting)

The upper spectroscopy level interacts with two light fields 2.4 μm and 313 nm, of which the latter couples to the continuum. We therefore observe a splitting of the line f_{a1}. This is known as the Autler-Townes effect (or a.c. Stark splitting) [50] and has been observed for multi-photon processes in strong laser fields, both continuous-wave and pulsed. For the case of HD$^+$, we have previously investigated this effect in our apparatus and determined a square-root dependence on the UV-laser intensity, consistent with reports in the literature [51, 52]. We have measured the splitting for component f_{a1}, for nominal and high trap RF amplitudes. Both observed splittings agree within the combined uncertainties and the mean amounts to $\Delta f_{\mathrm{AT,nom},a1} = 196(15)\,\mathrm{Hz}$ at the nominal 313 nm intensity $I_{313,\mathrm{nom}}$. We assume that the ratio $\Delta f_{\mathrm{AT}}/\sqrt{I_{313}} = \Delta f_{\mathrm{AT,nom},a1}/\sqrt{I_{313,\mathrm{nom}}}$ is the same for all lines.

e.   Black-body radiation shift

The black-body radiation shift of H$_2^+$ is predicted to be of order 10^{-17} fractionally at room temperature [49], and is ignored.

f.   Maser shift

As in our previous works [4, 6, 7, 10], the frequency of the spectroscopy wave is measured relative to a hydrogen maser's 5 MHz output. This frequency is continuously compared with a 1 pulse-per-second signal provided by a GNSS receiver. Common-view GNSS data allows us to determine the maser frequency with respect to the German national metrology time standard. We determined the maser's fractional frequency offset to be approximately $+1 \times 10^{-11}$, and the fractional drift was approximately $+3 \times 10^{-15}$/day. The measured laser frequencies are corrected for the time-varying maser offset. The uncertainty of this correction was determined to be approximately 10 mHz.

g. *Evaluation of deperturbed values $f_{\text{spin-avg}}^{(expt)}$ and $c_e^{(expt)}$*

The determination of the quantities of interest in presence of the above systematic effects is performed by a LSA. To this end, we model a measured transition frequency j as follows:

$$f_{\text{obs},i}^{(j)} = f_{\text{spin-avg}}^{(expt)} + c_{\text{spin},i} c_e^{(expt)} + c_{\text{lin},i} B_{\text{REMPD}} + c_{\text{quad},i} B_{\text{REMPD}}^2 + \delta f_{\text{AT}}^{(j)} + \Sigma_{\text{effect}} \delta f_{\text{effect},i}^{(j)} \, .$$

The subscript i refers to both a particular spin-rotation component and a particular Zeeman component. The index j denotes individual measurements, i.e. for a given i, the superscript j may take on different values. $f_{\text{obs},i}^{(j)}$ is the measured line frequency with a statistical uncertainty given by the line's half width at half maximum and $\delta f_{\text{AT}}^{(j)}$ is its shift due to the AT effect. The spin coefficients of the upper spectroscopy level $c_{\text{spin},i} = (F_i'(F_i' + 1) - N(N + 1) - 3/4)/2$ (see main text) and Zeeman coefficients $c_{\text{lin},i}$, $c_{\text{quad},i}$ of component i are taken to be the theoretical values (see Sec. A 2 a).

For each systematic shift, we define the contribution as $\delta f_{\text{effect},i}^{(j)} = r_{\text{effect},i} k_{\text{effect}} Q_{\text{effect}}^{(j)}$, with the relative sensitivity $r_{\text{effect},i}$ of a spin-rotation-Zeeman component i and the global sensitivity k_{effect} of the rovibrational transition. The parameter $Q_{\text{effect}}^{(j)}$ is one of the following: the spectroscopy wave power, $P_{2.4}^{(j)}$, the Doppler cooling wave power $P_{313}^{(j)}$, or the squared trap's RF amplitude $\left(V_{\text{RF}}^{(j)}\right)^2$. The parameters k_{effect} must be adjusted by the LSA, because we do not know the precise light intensities and electric fields at the ions' locations.

The values $r_{\text{effect},i}$ are computed as the ratios of theoretical polarizabilities of the Zeeman components [49]. The total polarizability of a component is the sum of a scalar (spin-independent) and a tensor polarizability, where the latter can be expressed as a spin-independent value multiplied by a state-dependent factor S and a polarization-dependent factor G. The tensor polarisability is zero when $N = 0$, hence it is zero in the lower spectroscopic states. We have $S(f_{a1}) = -24/5$, $S(f_{b1}) = -21/5$ and $S(f_{b2}) = 21/5$. In order to compute the total polarizability of the transitions, it is necessary to combine the values of the scalar and tensor polarizabilities of the lower and upper levels, as given in [10, 49]. Note that the $r_{i,\text{effect}}$ of the same component i are distinct for different effects, since the scalar and tensor polarizabilities are, in general, frequency-dependent. A table of numerical values $r_{\text{effect},i}$ used in the adjustment can be found in SM.

In order to perform the LSA, the equations should be linearized. The only non-linear contribution is the quadratic Zeeman shift. We linearize the equations by expressing the

magnetic field $B_{\mathrm{REMPD}} = B_0 + \delta B$ as the sum of a constant value B_0, approximately known from previous experiments, and an adjustable small deviation δB. The term quadratic in δB may safely be neglected.

In summary, the LSA includes 11 observational equations to which 6 parameters are adjusted, $f_{\mathrm{spin\text{-}avg}}^{(\mathrm{expt})}$, $c_{\mathrm{e}}^{(\mathrm{expt})}$, δB, $k_{2.4}$, k_{313}, k_{RF}. All input data is uncorrelated.

The AT effect is not considered in the same form as the other systematic effects, since it is a splitting rather than a shift. For those lines, for which we have measured the splitting (note that for these $I_{313}^{(j)} = I_{313,\mathrm{nom}}$), the shift is simply given by half the observed splitting, $\delta f_{\mathrm{AT}}^{(j)} = \mp 1/2 \Delta f_{\mathrm{AT,nom}}$. Positive and negative signs correspond to the smaller and larger frequency component, respectively. For the other lines, we present two approaches for accounting for the effect:

Approach (I): Since the sign of $\delta f_{\mathrm{AT}}^{(j)}$ is unknown for these cases, we set $\delta f_{\mathrm{AT}}^{(j)} = 0$, but with uncertainty $u(\delta f_{\mathrm{AT}}^{(j)}) = \Delta f_{\mathrm{AT}}^{(j)}/2$. Furthermore, the scaling with intensity is $\Delta f_{\mathrm{AT}}^{(j)} = \sqrt{I_{313}^{(j)}/I_{313,\mathrm{nom}}} \times \Delta f_{\mathrm{AT,nom},a1}$. Since $\Delta f_{\mathrm{AT,nom},a1}$ is much larger than the statistical uncertainty of the lines, and combined with the fact, that our measurements can neither resolve a shift due to $I_{2.4}$ nor due to V_{RF}, the resulting uncertainty of $f_{\mathrm{spin\text{-}avg}}^{(\mathrm{expt})}$ and $c_{\mathrm{e}}^{(\mathrm{expt})}$ is far exceeds our line resolution. The values presented in the main text of the manuscript result from this approach. The values of systematic shifts of individual Zeeman components $\delta f_{\mathrm{effect}}^{(j)}$ given in Tab. II are computed using the resulting sensitivities k_{effect}.

Approach (II) is described in SM.

3. *Ab initio* theory of $f_{\mathrm{spin-avg}}$

Theoretical data have been obtained in two steps. First, the spin-averaged transition frequency was calculated as an expansion in terms of the coupling parameter, the fine structure constant α. We started from the nonrelativistic solution of the Schrödinger equation. Second, higher-order corrections were obtained in a perturbative way along the lines of the NRQED effective field theory [15]. The individual contributions are: $f^{(0)} = 124\,485\,554\,550.71$ kHz (nonrelativistic three-body Schrödinger solution), $f^{(2)} = 2\,002\,698.73$ kHz (relativistic corrections in Breit–Pauli approximation; nuclear radii), $f^{(3)} = -521\,345.53$ kHz (leading-order one-loop radiative corrections), $f^{(4)} = -3\,689.05$ kHz (one- and two-loop radiative corrections; relativistic corrections), $f^{(5)} = 228.67$ kHz (radia-

tive corrections up to three loops, Wichmann–Kroll contribution), $f^{(6)} = -1.62$ kHz (one- and two-loop radiative diagrams, Wichmann-Kroll contribution), $f^{\text{other}} = 0.54$ kHz (muon and hadron vacuum polarization). Here, $f^{(n)}$ denotes a contribution proportional to $cR_\infty \alpha^n$. The sum of all these contributions, $f_{\text{spin-avg}}^{(\text{theor})}$, together with the theoretical uncertainty, is given in the main text. The above values are for CODATA 2022.

The sensitivity of the spin-averaged frequency to m_p/m_e has been reported in [10], $\partial f_{\text{spin-avg}}/\partial(m_\text{p}/m_\text{e}) = -0.43976 \times f_{\text{spin-avg}}/(m_\text{p}/m_\text{e})$.

4. *Ab initio* theory of the spin-rotation coupling

$c_e^{(\text{theor})}$, given in the main text, is calculated theoretically using the Breit-Pauli Hamiltonian and then including higher-order corrections up to order $m\,\alpha^7 \ln\alpha$. When higher-order corrections are considered, other spin interaction terms may also appear, for example proportional to $\mathbf{I}_1 \cdot \mathbf{I}_2$. Firstly, they are a factor $\alpha^2(m_e/m_p)^2$ smaller than the leading-order hyperfine structure splitting of the state. Secondly, the total nuclear spin in every rotational state N is fixed and thus also the value of $\mathbf{I}_1 \cdot \mathbf{I}_2$ is uniquely determined. This means that these new terms do not contribute to the splitting, but to the spin-averaged energy. They are included in $f^{(4)}$ above.

5. *Ab initio* theory of the Zeeman interaction

The interaction of para-H_2^+ with an external magnetic field is described by the effective Hamiltonian:

$$H_{mag} = -\mu_B \left(g_N \mathbf{N} + g_e \mathbf{s}_e\right) \cdot \mathbf{B},$$

where $\mu_B = |e|\hbar/(2m_e c)$ is the Bohr magneton, $g_N(v, N)$ is the orbital g factor, and $g_e(v, N) \simeq -2.002319$ is the bound-electron g factor. g_N is calculated numerically from the nonrelativistic three-body-bound-state wave function [53, 54]. For the upper level of the transition, $g_N(v = 3, N = 2) = 0.48156 \times 10^{-3}$. The computation of the Zeeman shifts is given in the Supplemental material of ref. [1].

6. Results and discussion

In this chapter the principal findings from the spectroscopic studies detailed in sections 5.2 and 5.3 will be summarized and consequences for the research aims will be discussed.

6.1. Observation of a laser induced transition in H_2^+

With the first study in Section 5.2, we have demonstrated the detection of the rovibrational transition $(v, N) : (1, 0) \rightarrow (3, 2)$ in H_2^+. By irradiating the spectroscopy wave along the axis of the RF trap, we were able to measure a Doppler-broadened transition of both f_a and f_b (see Fig. 4.4). This study represents the second instance of driving and detecting an electric quadrupole transition in a molecular ion using lasers, and the first instance of doing so in H_2^+. Due to the Doppler-broadening, which was on the order of a few megahertz, it was not possible to resolve individual Zeeman components. Interpreting the observed linewidth to be fully attributable to the Doppler-effect, a temperature of 3.4 mK was determined for the ensemble of H_2^+ ions.

With the acquisition of f_a and f_b, the measurement comprises the full structure of the transition. These have been determined to be

$$f_a^{(\text{expt})} = 124\,487\,066.7(1.9)_{\text{expt}}\,\text{MHz}\,,$$
$$f_b^{(\text{expt})} = 124\,486\,979.9(2.3)_{\text{expt}}\,\text{MHz}\,.$$

Note that the notation has been adapted from Sec. 5.2 to align with the one used in Sec. 5.3.

Given the slow nature of the H_2^+-spectroscopy procedure, it was deemed more prudent to examine potential systematic shifts through an investigation of a comparable E2 transition in HD^+: $(0, 0) \rightarrow (2, 2)$. By employing analogous methods as developed for E1 spectroscopy of HD^+ to measure single Doppler-free Zeeman components [21, 12, 23], a comprehensive systematic investigation of the transition could be performed. With linewidths as narrow as $\sim 40\,\text{Hz}$ and corresponding line resolutions of 2.7×10^{12}, the measurements represent a significant improvement in resolution by a factor of $\sim 10^6$ compared to the first observation of electric quadrupole transitions in molecular ions [100]. Moreover, the resolution of these measurements is comparable to that of the most precise electric dipole transition measurements performed on HD^+ [12, 97]. The present study demonstrates that E2 transitions in MHIs can be investigated systematically at a level that is sufficient for fundamental physics purposes.

The shifts of the H_2^+-transition could be inferred from those measured on HD^+ and were found to be negligible in comparison to the H_2^+ spectroscopic resolution. Consequently, the spin-averaged frequency and the spin-rotation coefficient can be directly computed from $f_a^{(\text{expt})}$ and $f_b^{(\text{expt})}$: $f_{\text{spin-avg}}^{(\text{expt})} = 124\,487\,032.7(1.5)\,\text{MHz}$ and $c_e^{(\text{expt})} = 34.8(1.2)\,\text{MHz}$. The values are in agreement with the theoretical prediction. Due to the Doppler-broadening, the experimental uncertainties

are significantly larger than those of the theory, and are not yet sufficiently small to allow for competitive fundamental physics evaluations. Nevertheless, a value for the proton-electron mass ratio could be computed and was found to be in agreement with the CODATA18 value, although with an uncertainty that is more than two orders of magnitude larger.

6.2. Doppler-free measurement of a H_2^+ transition

Following the observation of Doppler-broadened lines, an investigation into Doppler-free transitions using TICTES was conducted in the second study (Sec. 5.3). Accordingly, the spectroscopy laser was irradiated in a transverse arrangement with respect to the trap axis. Given the narrow width of the transitions due to their small natural linewidth and a deliberately imposed uncertainty in the theoretical prediction for the purpose of a blind search, the detection of Doppler-free transitions in H_2^+ proved to be a challenging endeavor. Nevertheless, over the course of approximately one year, a measurement of Doppler-free lines including a study of the systematic effects of the transition $(1,0) \rightarrow (3,2)$ was realized. Three single Zeeman components f_{a1}, f_{b1} and f_{b2} have been resolved, with a minimum of one for each spin-rotation component (see Fig. 4.4). Linewidths as small as $\simeq 6\,\mathrm{Hz}$ were observed, corresponding to line quality factors of 2.2×10^{13}, a factor of 10 better than the first measurement presented in this thesis (Sec. 6.1). From these measurements, the accuracy of the aforementioned spin-rotation components could be improved by more than three orders of magnitude:

$$f_a^{(\mathrm{expt})} = 124\,487\,067\,172.9(6)_{\mathrm{expt}}\,\mathrm{kHz}\,,$$
$$f_b^{(\mathrm{expt})} = 124\,486\,980\,347.5(8)_{\mathrm{expt}}\,\mathrm{kHz}\,.$$

Due to the particularities of the systematic shift determination, the uncertainties associated with these two values are correlated. As a result, the reduction in uncertainty of $f_{\mathrm{spin\text{-}avg}}$ and c_e in comparison to the initial observation is not as substantial as that observed for the individual spin-rotation components. The deduced values for these are

$$f_{\mathrm{spin\text{-}avg}}^{(\mathrm{expt})} = 124\,487\,032\,442.69(95)_{\mathrm{expt}}\,\mathrm{kHz}\,,$$
$$c_e^{(\mathrm{expt})} = 34\,730.18(10)_{\mathrm{expt}}\,\mathrm{kHz}\,.$$

They agree with the most recent theoretical computations

$$f_{\mathrm{spin\text{-}avg}}^{(\mathrm{theor})} = 124\,487\,032\,442.5(0.9)_{\mathrm{QED}}(0.96)_{\mathrm{CODATA22}}\,\mathrm{kHz}\,,$$
$$c_e^{(\mathrm{theor})} = 34\,730.25(12)_{\mathrm{QED}}\,\mathrm{kHz}\,,$$

provided in Sec. 5.3 and [44], respectively. The uncertainties are here distinguished between contributions stemming from uncomputed theoretical terms ("QED") and uncertainties of fundamental constants ("CODATA22"). Notably, for the first time in history, the uncertainties of an experimental and theoretical determination of a spin-averaged frequency of a rovibrational transition in H_2^+ are approximately equal.

6.3. The proton-electron mass ratio

It has been discussed extensively in Chapter 1, that a spectroscopy result of the kind presented in the preceding section 6.2 enables the determination of fundamental constants, most notably

the mass ratio of the proton and the electron. It is computed by adjusting its input value to the theoretical computation of $f_{\text{spin-avg}}^{(\text{theor})}$ in such a way that theory and experiment agree (see eq. 1.4 in Sec. 1.1). Note, that the Rydberg constant and the proton charge radius are input data used in the adjustment, with initial values taken from CODATA22. They are not effectively adjusted however, since the measured transition does not express a large enough sensitivity to these constants (see eq. 1.4). From $f_{\text{spin-avg}}^{(\text{expt})}$ of the previous section, we obtain

$$\frac{m_p}{m_e} = 1836.152673416(44)\,,$$

where the uncertainty arises in equal parts from theory and experiment. A notable aspect of this value is that it is derived purely through spectroscopic means, as all underlying experiments investigate the quantized nature of matter: optical spectroscopy of the hydrogen atom furnishes the necessary input values R_∞ and r_p, which are then utilized in conjunction with the present result to yield m_p/m_e.

The present value is in agreement with the most recent international standard of CODATA22, with an uncertainty that is 1.4 times larger. Furthermore, it is in agreement with the former value of CODATA18, but compared herewith has an uncertainty smaller by a factor of 2.5. A graphical representation of these comparisons and earlier CODATA values is provided in Fig. 6.1. It is sensible to make a comparison with both standards, since results obtained for HD$^+$ are partially considered in the CODATA22 adjustment, which was not the case prior. As a consequence, only the CODATA18 value can be understood as a constant independent of MHI spectroscopy results. The comparison of the present value and the CODATA18 value therefore can be understood as two independent measurements originating from different experiments and theories developed and performed by different groups of researchers. Their agreement is thus a powerful consistency test of the underlying work.

It should be noted that other constants, primarily the proton charge radius and the Rydberg constant, are required as input data to obtain the proton-electron mass ratio. An adjustment of these constants may also be considered, using the present result in addition to hydrogen spectroscopy data as input. Doing so, it becomes evident that the present result is not yet sufficiently accurate to allow for the determination of these quantities with a competitive degree of accuracy. Consequently, the present result is not yet able to contribute to the discussion that has evolved around the value of the proton charge radius. This is discussed in more detail in Sec. 5.3.

The evaluation can be expanded to include recent measurements of transitions in HD$^+$. A value of the deuteron-proton mass ratio can then be extracted in a similar manner, thus enabling a pure spectroscopic determination of both mass ratios from MHI data. The deduced value for the deuteron-proton mass ratio

$$\frac{m_d}{m_p} = 1.99900750139(11)\,,$$

is in agreement with a value obtained from cyclotron frequency measurements performed in a Penning trap [27], although not as accurate. The fractional deviation of the two values is $5.9(5.5) \times 10^{-11}$, showing agreement at approximately one times their combined uncertainties. This value realizes the comparison of Newtonian and quantum mechanics, as discussed in Sec. 1.1, where agreement is seen.
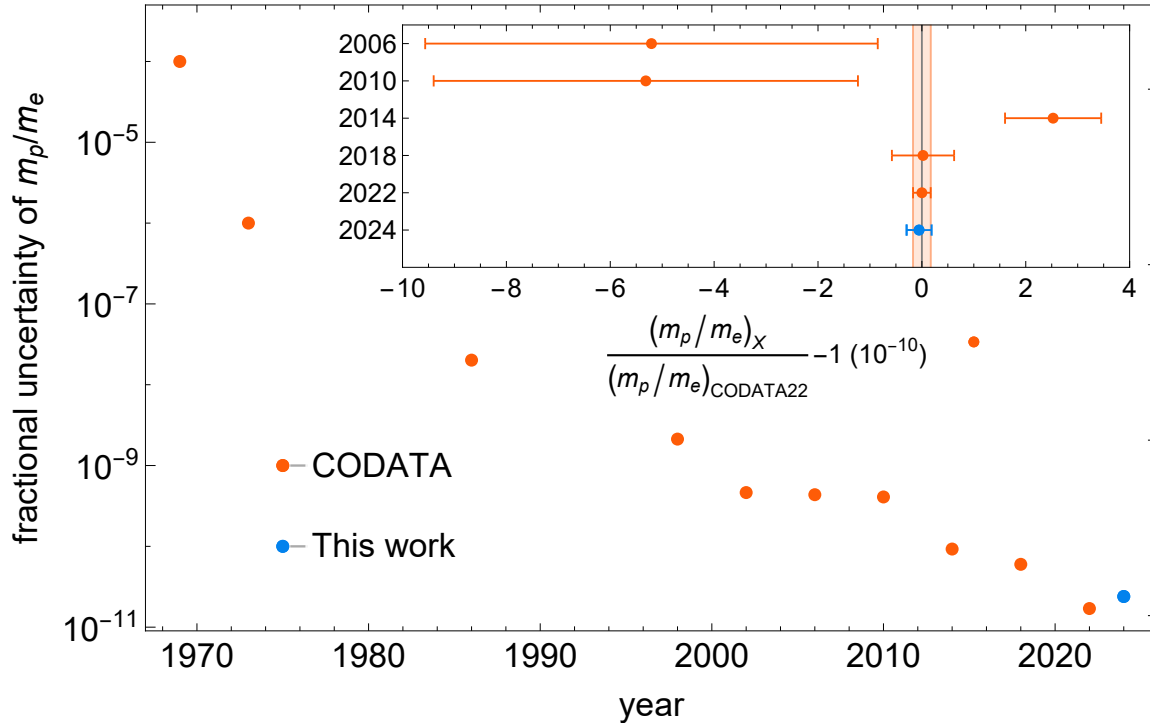
Figure 6.1.: The uncertainty and relative value of the proton-electron mass ratio over the course of time. The fractional uncertainty of historical CODATA values (orange) is shown in comparison to the uncertainty achieved in this work (blue). Additionally, the inset shows the fractional offset of a selection of the values, with the same uncertainties displayed as error bars. The shaded area represents the uncertainty range of the most recent CODATA22 value. The result of this work is in very good agreement with recent CODATA values (2018, 2022).

6.4. Frequency ratios

The agreement of experimental and theoretical values seen in Sec. 6.2 can be considered as a confirmation of the underlying theoretical framework at relative level of 1.3×10^{-11}. Similarly, a confirmation is inferred from the agreement seen for the values of the proton-electron mass ratio. However, this test relies on fundamental constants derived from various measurements and corresponding theories.

One may circumvent this dependency and improve the test by employing the frequency ratios discussed in Sec. 1.2. A second measurement of a MHI transition is required, for which the recent transition $(0,0) \to (5,1)$ of HD^+ is taken [12], denoted as f_5. The test is performed by comparing the ratio $\mathcal{R} = f_5/f_{\text{spin-avg}}$ of experimental and theoretical values. Their fractional deviation is

$$\frac{\mathcal{R}^{(\text{expt})} - \mathcal{R}^{(\text{theor})}}{\mathcal{R}} = -2.4(8.0)_{\text{expt}}(0.9)_{\text{theor}}(1.0)_{\text{CODATA18*}} \times 10^{-12} .$$

The asterisk indicates that, in addition to the CODATA18 set of fundamental constants, a recent value for the deuteron-proton mass ratio was used [27].

This value has a combined uncertainty of 8.1×10^{-12} and therefore infers correctness of MHI theory at that level. It represents a marginal improvement over the direct experiment-theory

comparison mentioned at the beginning of this section, which is representative of the fact that the frequency ratios can only serve to reduce theoretical errors. The leading contribution to the uncertainty of the ratio is that of the experiment. Nevertheless, this value represents one of the most precise matches between experiment and theory in physics, with a precision that is only a factor $\simeq 8$ less precise than that achieved in the g-factor measurement of the electron [1].

7. Outlook

The groundwork for the optical spectroscopy of the molecular hydrogen ion H_2^+ established in this thesis paves the way for a variety of further studies.

As an immediate next step, the accuracy of the present work's findings could be improved through a more rigorous determination of systematic effects. This is a particularly attractive proposition, given that the accuracy of the spin-averaged transition frequency is inferior to the spectroscopic resolution by two orders of magnitude. The primary reason is the conservative evaluation of systematic effects necessitated by the observed Autler-Townes splitting. In principle, it should be feasible to determine the systematic shifts with an uncertainty that is comparable to the resolution, thereby allowing an increase in accuracy by two orders of magnitude. To achieve this, further measurements conducted under a range of parameter settings are required in order to precisely characterize the Autler-Townes splitting and reduce the associated uncertainty. However, this alone would not be sufficient to obtain the same level of improvement in the accuracy of fundamental constants, as a comparable advancement in theory is also necessary. Nevertheless, an improved experimental result that would then be better than the theory by two orders of magnitude would undoubtedly stimulate further research on the theoretical side. Such an improvement would also facilitate a more rigorous test of QED.

Concurrently, the aforementioned improvement would render it a realistic prospect to contribute to the determination of other fundamental constants, primarily the proton charge radius. This property has been the subject of numerous studies, with partially conflicting results, which is known as the proton radius puzzle. An improved determination of H_2^+ transition frequencies will, at some point, become sensitive to r_p and could contribute to the discussion.

A comparable improvement could be achieved by transitioning to more sophisticated trapping techniques. At the forefront of the field are single-particle traps that no longer rely on destructive spectroscopy, as is the case here. Instead, non-destructive techniques, such as quantum-logic spectroscopy [101] or optical-dipole force detection [95, 102], are utilized. These techniques reduce the spectroscopy cycle time by orders of magnitude, thereby increasing the sample statistics and improving the resulting determination of line frequencies and systematic effects. Non-destructive readout techniques have been demonstrated on MHIs, both in a linear RF trap on H_2^+ [67] as well as in a Penning trap on HD^+ [78].

In addition to the evaluations presented in this thesis, the H_2^+ spectroscopy results could be employed to contribute to the search for a potential fifth force (Sec. 1.2.2), as has been done for HD^+ [12]. Such an analysis would be most sensitive when testing for a hypothetical baryon-baryon interaction between the two nuclei. Since the present result agrees with the theoretical prediction, it is evident that no conclusive determination can be made regarding the existence of a fifth force. However, the result could likely improve the constraints on the free parameters of a fifth force, given that the accuracy is comparable to that obtained in HD^+ spectroscopy.

Further down the road lies the measurement of a set of transitions in MHIs, which would allow for a stand-alone and improved determination of the involved fundamental constants. A

recent study projects that an improvement in the accuracy of multiple constants compared to CODATA18 is possible, but will require the accurate measurement of multiple transitions in H_2^+, HD^+ and D_2^+ [7].

In the far future, a similar study to the one presented here could be conducted on the antimatter counterpart of H_2^+. This would realize a matter-antimatter comparison that has been a long-standing aspiration [18]. Currently, analogous experiments on proton-antiproton comparisons are performed in Penning traps. Consequently, optical spectroscopy experiments on H_2^+ in Penning traps would be highly desirable.

Acknowledgments

Appendix

A. Data for Fig. 2.6

Table A.1.: Raw data and references of experimental works for Fig. 2.6. Values given as relative accuracy are best estimates based on details given in the corresponding work and always correspond to the most accurate measurement performed. For a list of theoretical works used in Fig. 2.6, see Tab. A.2.

Experiments			
Name	Year	rel. accuracy	Source
Marmet and Kerwin	1960	7.4×10^{-2}	[103]
Jefferts	1969	1.2×10^{-6}	[50]
Asbrink	1970	1.8×10^{-4}	[104]
Takezawa	1970	4.6×10^{-4}	[105]
Herzberg and Jungen	1972	9.1×10^{-1}	[106]
Menasian and Dehmelt	1973	1.3×10^{-6}	[65]
Carrington et al.	1989	1.1×10^{-4}	[107]
Arcuni et al. (spin structure)	1990	2.1×10^{-4}	[108]
Arcuni et al. (rotational)	1990	2.8×10^{-7}	[68]
Fu et al.	1992	2.6×10^{-5}	[108]
Carrington et al.	1993	5.2×10^{-6}	[109]
Carrington et al.	1993	6.4×10^{-7}	[66]
Critchley et al.	2001	7.4×10^{-5}	[110]
Osterwalder et al.	2004	2.3×10^{-4}	[111]
Haase et al.	2015	4.4×10^{-7}	[112]
Schenkel et al.	2024	1.2×10^{-8}	[99]
Doran et al.	2024	7.8×10^{-9}	[69]
Alighanbari et al.	2024	7.9×10^{-12}	[42]

Table A.2.: Raw data and references of theoretical works for Fig. 2.6. Values given
as relative accuracy are best estimates based on details given in the corresponding work
and always correspond to the most accurate calculation performed. The first table gives the
result from the theory of rovibrational energies, and the second those from the theory of spin
energies. For a list of experimental works used in Fig. 2.6, see Tab. A.1.

Theory, rovibrational			
Name	Year	rel. accuracy	Source
Johnson	1941	2.5×10^{-4}	[35]
Cohen et al.	1960	1.0×10^{-4}	[113]
Wind	1965	1.0×10^{-7}	[114]
Moss	1993	4.6×10^{-8}	[33]
Korobov	2006	1.2×10^{-9}	[39]
Korobov et al.	2014	4.0×10^{-11}	[115]
Korobov et al.	2021	8.0×10^{-12}	[25]

Theory, spin			
Name	Year	rel. accuracy	Source
Dalgarno et al.	1961	1.0×10^{-2}	[46]
Somerville	1968	7.1×10^{-4}	[116]
McEachran et al.	1978	5.3×10^{-4}	[48]
Babb and Dalgarno	1992	1.1×10^{-4}	[49]
Korobov et al.	2006	6.3×10^{-5}	[43]
Korobov et al.	2009	1.1×10^{-5}	[117]
Haidar et al.	2022	3.5×10^{-6}	[44]

B. Supplementary Material of Sec. 5.1

Metrology-grade spectroscopy source based on an optical parametric oscillator: supplement

M. R. Schenkel,[1,2] **V. A. Vogt,**[1] **and S. Schiller**[1,3]

[1]*Heinrich-Heine-Universität Düsseldorf, Mathematisch-Naturwissenschaftliche Fakultät, Institut für Experimentalphysik, 40225 Düsseldorf, Germany*
[2]*magnus.schenkel@hhu.de*
[3]*step.schiller@hhu.de*

A metrology-grade spectroscopy source based on an optical parametric oscillator: Supplement 1

1. FIGURE OF PLL BEATS AT VARIOUS WAVELENGTHS

Figure S1 shows the linewidths and phase noise spectra of the PLL for three different idler wavelengths in the same style as Fig. 3 of the main text.
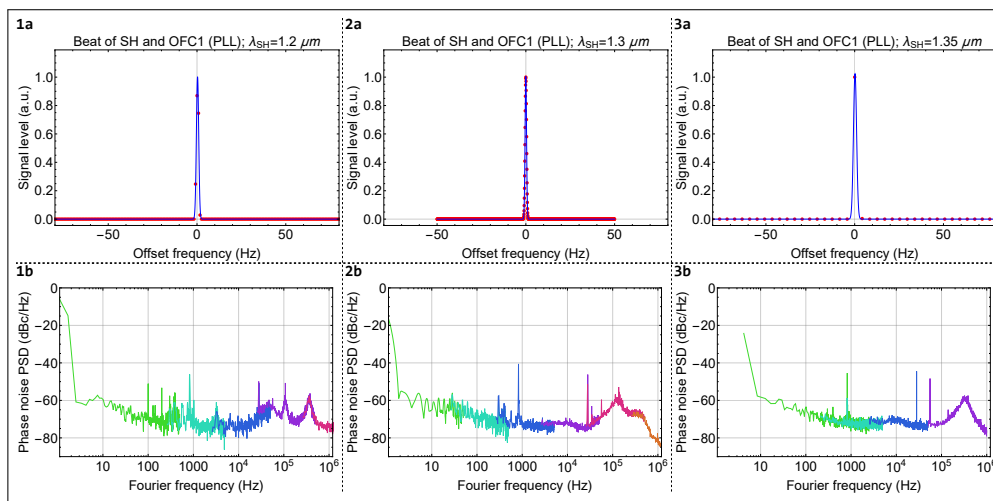
Fig. S1. Beat spectrum shown as a zoom-in of the beat (top row) and the phase-noise power spectral density (PSD, bottom row) of the beat between the idler SH and OFC1 in the locked state for three different idler wavelengths. Columns 1, 2, 3 correspond to idler wavelengths of 2.4, 2.6, 2.7 μm, respectively. For the top row, all data are taken with a RBW of 1 Hz and are normalized to the peak level of the fitted function. Due to a different frequency resolution used for the individual data sets, the center peak in panel 3a is not well resolved. In this case, the Gaussian fit function is shown for illustrative purposes only. For the bottom row, individual colors correspond to individual measurements, which are normalized to their RBW. The signal-to-noise ratio is in all cases similar to the 70 dB stated in the main text. Compared to the PSD measurement in Fig. 3, panel 2b of the main text, the PSDs exhibit additional noise peaks. This is due to an incomplete optimization of the lock settings. Such an optimization is required after tuning the wavelength of the idler, which results in a change of the beat signal level.

C. Supplementary Material of Sec. 5.3

Determination of the proton-electron mass ratio by high-accuracy laser spectroscopy of $\mathbf{H}_2^+$

S. Alighanbari, M. R. Schenkel, and S. Schiller*

Institut für Experimentalphysik, Heinrich-Heine-Universität Düsseldorf, 40225 Düsseldorf, Germany

V. I. Korobov

Bogoliubov Laboratory of Theoretical Physics,
Joint Institute for Nuclear Research, 141980 Dubna, Russia

(Dated: July 30, 2024)

1

SUPPLEMENTARY INFORMATION

A. Figures of measurements of systematics
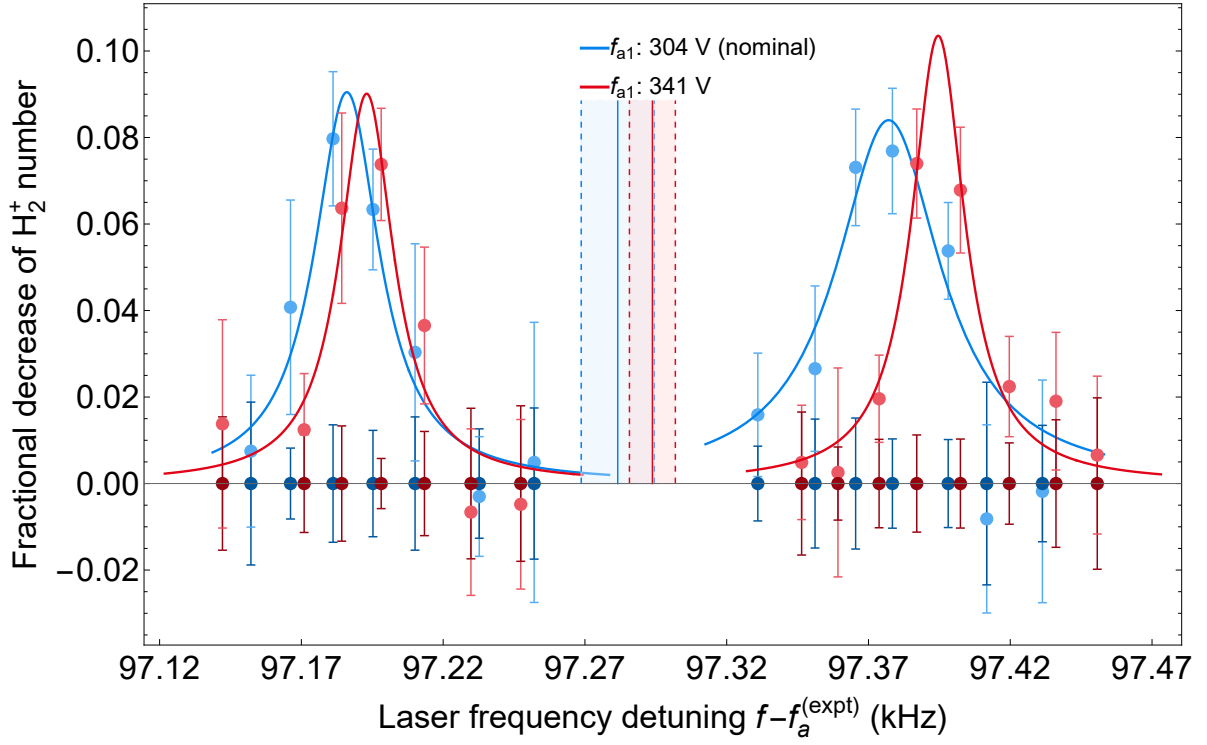
Supplementary Information Figure 1:

The two AT doublets of Zeeman component f_{a1} for two different values of the trap RF amplitude. The two lines measured under nominal conditions (blue) are identical to the data shown in Fig. 3 of the main text. The laser frequency detuning is given relative to the deperturbed frequency of spin component $f_a^{(\text{expt})}$. The deperturbed frequencies and their uncertainty ranges are indicated by full and dashed lines in corresponding colours. Points in brighter colour are the signal values, while the darker ones are background. The coloured curves are guides to the eye.

1
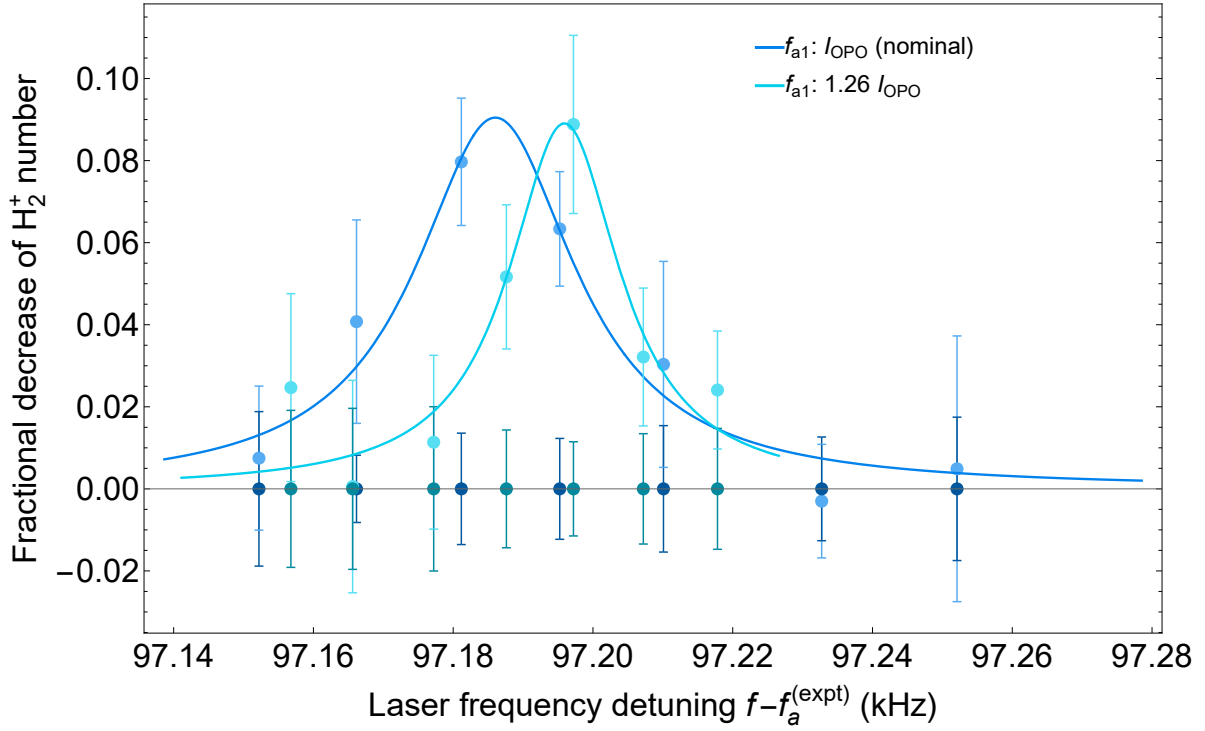
Supplementary Information Figure 2:

The Zeeman component f_{a1} for two different values of the intensity of the spectroscopy wave (wavelength 2.4 μm). The line measured under nominal condition is identical to the lower component of the AT doublet shown in Fig. 3 of the main text. The laser frequency detuning is given relative to the deperturbed frequency of spin component f_a. Points in brighter colour are the signal values, while the darker ones are background. The coloured curves are guides to the eye.

2
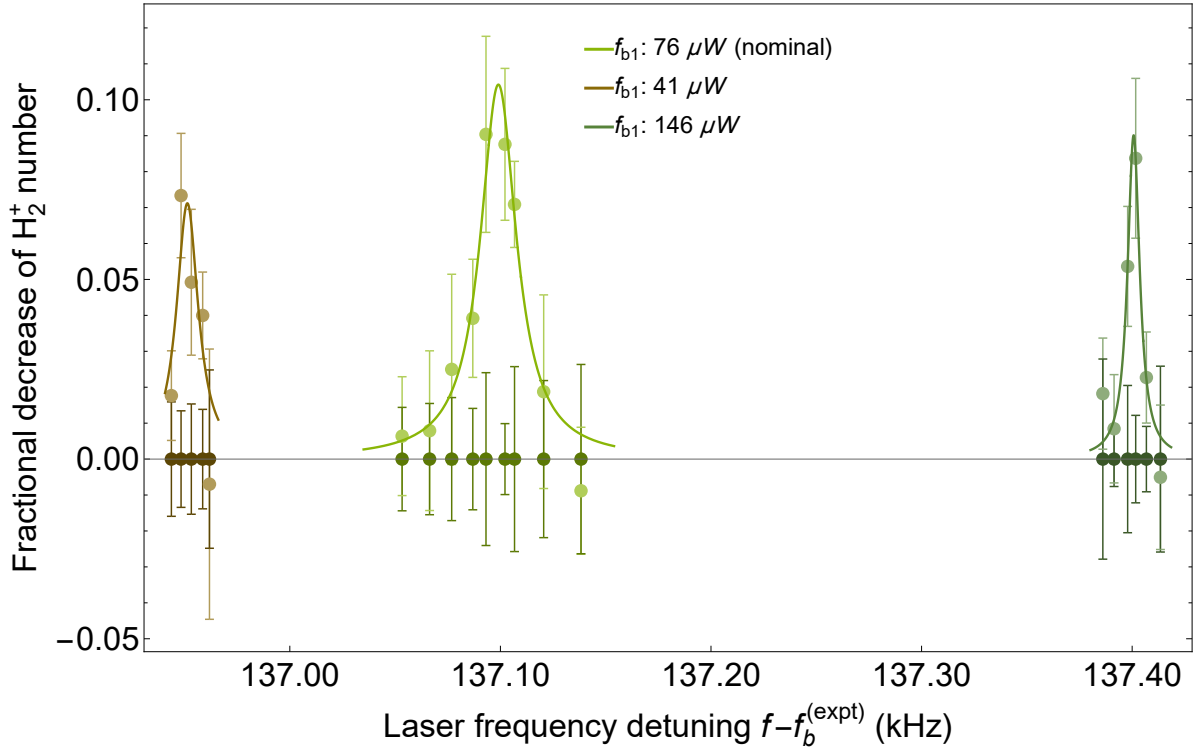
Supplementary Information Figure 3:

The Zeeman component f_{b1} for three different values of the power of the 313 nm wave. In this case, a change in power is proportional to a change in intensity, since the beam size was kept constant. The line measured under nominal condition is identical to the data shown in Fig. 3 of the main text. For each intensity setting, only one line of the AT doublet was measured and we did not indentify which of the two lines was observed. However, a light-induced shift that exhibits a cleanly linear dependence on the 313 nm wave power is only obtained if it is assumed that the three displayed lines are the same component of the AT doublet. The laser frequency detuning is given relative to the deperturbed frequency of spin component f_b. Points in brighter colour are the signal values, while the darker ones are background. The coloured curves are guides to the eye. We attribute the different linewidths of the observed lines in part to a change in the reference laser of the optical frequency comb that occured inbetween the measurements.
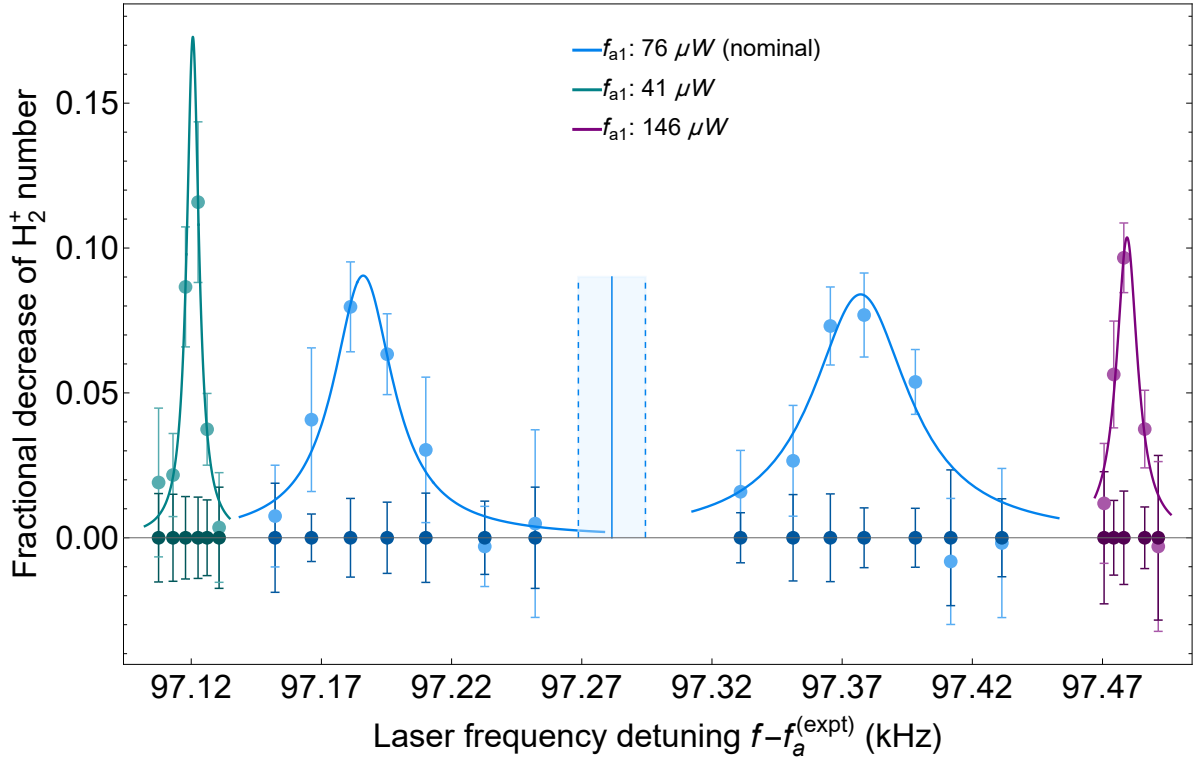
Supplementary Information Figure 4:

Zeeman component f_{a1} for three different values of the power of the 313 nm wave. In this case, a change in power is proportional to a change in intensity, since the beam size was kept constant. The AT doublet measured under nominal conditions (blue) is identical to the data shown in Fig. 3 of the main text. The laser frequency detuning is given relative to the deperturbed frequency of spin component f_a. Points in brighter colour are the signal values, while the darker ones are background. The coloured curves are guides to the eye. We attribute the different linewidths of the observed lines in part to a change in the reference laser of the optical frequency comb.

4

5

B. Polarizability ratios

effect	$r_{\text{effect,a1}}$	$r_{\text{effect,b1}}$	$r_{\text{effect,b2}}$
a.c. Stark (2.4 μm)	1.000	1.080	2.197
a.c. Stark (313 nm)	1.000	1.052	1.784
RF trap shift	1.000	1.080	2.203

Supplementary Information Table 1:

Table of polarizability ratios $r_{\text{effect},i}$. The ratios are normalized to the polarizability of Zeeman component f_{a1}. Consequently, the adjusted k_{effect} is the sensitivity of this particular component. The values are distinct for each effect, since the polarizabilities depend on the field frequency. For the last column (RF trap shift), the values of the static polarizabilities were used, since the RF frequency is small.

C.   Approach (II) for spin-averaged frequency and spin-rotation coefficient

Here, we attempt to incorporate the knowledge of the discrete nature of the AT shift and to identify the unknown AT shift signs. For this purpose, we assume a particular sign $\sigma^{(j)} = \pm 1$ for each line j and set $\delta f_{\mathrm{AT}}^{(j)} = \sigma^{(j)} \Delta f_{\mathrm{AT}}^{(j)}/2$. $\Delta f_{\mathrm{AT}}^{(j)}$ has an uncertainty stemming from $\Delta f_{\mathrm{AT,nom},a1}^{(j)}$, and we introduce an additional uncertainty u_{AT} (independent of j) in order to obtain agreement between the fitted model and the data, as follows. Evaluating the LSA with this input, the uncertainties of both $f_{\mathrm{spin\text{-}avg}}^{(\mathrm{expt})}$ and $c_{\mathrm{e}}^{(\mathrm{expt})}$ are reduced by approximately a factor of 5 compared to the approach (I). Since seven signs $\sigma^{(j=1\ldots7)}$ are unknown, there are $2^7 = 128$ possible combinations to consider. To determine the likelihood of particular combinations we can make use of the frequency ratios $\mathcal{R}_{5,2'}$ and $\mathcal{R}_{1,2'}$ discussed in the main text, as well as the reduced chi-squared parameter χ_ν^2 resulting from the LSA. We may assume that not only the present but also our own previous experiments on HD$^+$ and its theory are correct at the level of the presented uncertainties. We then do not expect a substantial disagreement between the experimental and theoretical ratios. And secondly, we assume that the reduced chi-squared parameter shows a consistency between the model and the data. Our criterion for absence of disagreement in both cases is a deviation smaller than or equal to 3 sigma. For the ratios this is evaluated through their uncertainties, while for the reduced chi-squared parameter we rely on the canonical bound $\chi_\nu^2 \leq \chi_{\nu,\max}^2 = 2.9$ for the present number of degrees of freedom. If the uncertainty $u_{\mathrm{AT}} = 0$, the minimum χ_ν^2 for all 128 combinations is 4.1, indicating an underestimation of the experimental errors. A total of 12 combinations have a χ_ν^2 similar to this value, while the next larger χ_ν^2 is 12.5, showing a clear preference of the model for these combinations. We therefore increase the uncertainty u_{AT} to reduce χ_ν^2 until the above bound is fulfilled for the 12 combinations. We obtain χ_ν^2 values in the range of 2.8 to 2.9 for $u_{\mathrm{AT}} \simeq 11\,\mathrm{Hz}$. Turning to the frequency ratios, only six of the 12 combinations show no disagreement regarding $\mathcal{R}_{5,2'}$, $\mathcal{R}_{1,2'}$. From these six cases we derive values for $f_{\mathrm{spin\text{-}avg,II}}^{(\mathrm{expt})}$ and $c_{\mathrm{e,II}}^{(\mathrm{expt})}$. We conservatively estimate them as the mid-values of the intervals containing all individual values with their uncertainties. The uncertainties are taken as equal to half the widths of the intervals. We obtain $f_{\mathrm{spin\text{-}avg, II}}^{(\mathrm{expt})} = 124\,487\,032\,442.59(67)\,\mathrm{kHz}$ and $c_{\mathrm{e, II}}^{(\mathrm{expt})} = 34\,730.176(69)\,\mathrm{kHz}$. In summary, these uncertainties are smaller by approximately a factor 1.4 compared to approach (I).

<center>6</center>

D.   Least-squares adjustment (LSA)

We perform the LSAs following ref. [1]. The basic algorithm is described in Appendix E of ref. [2]. The number of input data is n, and this input can be experimental data, theoretical data, or previously measured constants. This data can have correlations. The number of adjusted constants is M, where this output are fundamental constants and other parameters. n, M are given by

$$n = 2\mathcal{N}(\text{MHI input}) + \mathcal{N}(\text{mass ratio input and other input} : R_{\infty,18}, r_{p,18}, r_{d,18}) +$$
$$\mathcal{N}(\text{other input} : \text{H}, \text{H - D}) + \mathcal{N}(2^{\text{nd}} \text{ H - D datum}) \quad,$$
$$M = \mathcal{N}(\text{MHI input}) + \mathcal{N}(\text{other input} : \text{H}, \text{H - D}) + \mathcal{N}(\text{fund. const.}) \;,$$

where $\mathcal{N}(Y)$ denotes the number of items of type Y.

(i) The M adjusted constants include, depending on the particular LSA, the fundamental constants μ_{pd}/m_e, m_p/m_e, R_∞, r_p, r_d or a subset thereof. The value of m_d/m_p is computed from the adjusted μ_{pd}/m_e and m_p/m_e using the definition $\mu_{pd}/m_e = m_p m_d/m_e(m_p + m_d)$. Further adjusted "constants" are the theoretical additive corrections for the MHI, $\delta f^{(\text{theor})}(\text{HD}^+)$ and/or $\delta f^{(\text{theor})}(\text{H}_2^+)$, the so-called missing contributions. The number of adjusted MHI $\delta f^{(\text{theor})}$ is equal to the number of frequencies listed in the column "MHI input".

(ii) Every MHI input data consists of the experimental frequency $f_k^{(\text{exp})}$, the theoretical frequency $f_k^{(\text{theor})}([\mu_{pd}/m_e]_{18}, [m_p/m_e]_{18}, R_{\infty,18}, r_{p,18}, r_{d,18})$, evaluated for the CODATA 2018 fundamental constants (fiducial value), and an associated theoretical additive correction δf_k. The latter is nominally zero but has nonzero uncertainty. The δf_k of different MHI and different transitions are correlated, the correlation coefficients being given in [1].

(iii) In those LSAs where "H, H - D" is listed under "other input", "H" refers to two hydrogen 1s - 2s transition measurements (items A6, A7 in table X of ref. [3]) and "H - D" refers to one hydrogen-deuterium isotope shift measurement (A5 in table X). For the 1s - 2s measurements there is a corresponding single theoretical correction $\delta f(\text{H})$, described by B1, B2 in table VIII. For the isotope shift the theory correction $\delta f(\text{H - D})$ stems from items B1, B2, B17, B18 in table VIII. Correlation coefficients between the corrections δf are given in table IX.

Input data is analogous to the MHI input data, see (v) below. The additional adjusted

constants are $\delta f^{(\text{theor})}(\text{H})$ and $\delta f^{(\text{theor})}(\text{H - D})$. Analogous constants are considered in the CODATA adjustments, see Tab. XI in ref. [3].

(iv) In the column "Other input", we have used the short-hand notations $R_{\infty,18}$, $r_{p,18}$, $r_{d,18}$, to indicate the values of the CODATA 2018 compilation. The correlations between these values are taken into account.

(v) For each spectroscopy input datum k (from MHI, H and H - D), the observational equations are $f_k^{(\text{exp})} \dot{=} f_k^{(\text{theor})}(\mu_{pd}/m_e, m_p/m_e, R_\infty, r_p, r_p) + \delta f_k^{(\text{theor})}$, $\delta f_k \dot{=} \delta f_k^{(\text{theor})}$. If the CODATA 2018 fundamental constants are used as input instead of hydrogen spectroscopy data, then the corresponding equations are: $R_{\infty,18} \dot{=} R_\infty$, $r_{p18} \dot{=} r_p$, $r_{d,18} \dot{=} r_d$.

(vi) If the deuteron-proton mass ratio is an input, we include the observational equation $[m_d/m_p]_{\text{FM21}} \dot{=} ((m_p/m_e)/(\mu_{pd}/m_e) - 1)^{-1}$.

The observational equations are linearized around the fiducial values of the fundamental constants, i.e. the CODATA 2018 values.

In LSA 1, the constants R_∞, r_p, r_d are effectively not adjusted.

---

[1] S. Schiller, J.-P. Karr, Prospects for the determination of fundamental constants with beyond-state-of-the-art uncertainty using molecular hydrogen ion spectroscopy, Phys. Rev. A 109 (2024) 042825. doi:10.1103/PhysRevA.109.042825.

[2] P. J. Mohr, B. N. Taylor, CODATA recommended values of the fundamental physical constants: 1998, Rev. Mod. Phys. 72 (2000) 351–495. doi:10.1103/RevModPhys.72.351.

[3] E. Tiesinga, P. J. Mohr, D. B. Newell, B. N. Taylor, CODATA recommended values of the fundamental physical constants: 2018, Rev. Mod. Phys. 93 (2021) 025010. doi:10.1103/RevModPhys.93.025010.

Bibliography

[1] X. Fan, T. G. Myers, B. A. D. Sukra, G. Gabrielse, Measurement of the Electron Magnetic Moment, Phys. Rev. Lett. 130 (2023) 071801. `doi:10.1103/PhysRevLett.130.071801`.

[2] S. Schiller, Precision spectroscopy of molecular hydrogen ions: an introduction, Contemporary Physics 63 (2022) 247–279. `doi:10.1080/00107514.2023.2180180`.

[3] E. Tiesinga, P. J. Mohr, D. B. Newell, B. N. Taylor, The 2022 CODATA Recommended Values of the Fundamental Physical Constants (Web Version 9.0), Database developed by J. Baker, M. Douma, and S. Kotochigova, National Institute of Standards and Technology, Gaithersburg, MD 20899 (2024).
URL `https://physics.nist.gov/constants`

[4] E. Tiesinga, P. J. Mohr, D. B. Newell, B. N. Taylor, CODATA recommended values of the fundamental physical constants: 2018, Rev. Mod. Phys. 93 (2021) 025010. `doi:10.1103/RevModPhys.93.025010`.

[5] P. Mohr, D. Newell, B. Taylor, E. Tiesinga, CODATA Recommended Values of the Fundamental Physical Constants: 2022 (2024). `arXiv:2409.03787`.
URL `https://arxiv.org/abs/2409.03787`

[6] I. Angeli, K. Marinova, Table of experimental nuclear ground state charge radii: An update, Atomic Data and Nuclear Data Tables 99 (2013) 69–95. `doi:https://doi.org/10.1016/j.adt.2011.12.006`.

[7] S. Schiller, J.-P. Karr, Prospects for the determination of fundamental constants with beyond-state-of-the-art uncertainty using molecular hydrogen ion spectroscopy, Phys. Rev. A 109 (2024) 042825. `doi:10.1103/PhysRevA.109.042825`.

[8] J.-P. Karr, J. C. J. Koelemeij, Extraction of spin-averaged rovibrational transition frequencies in HD^+ for the determination of fundamental constants, Molecular Physics 121 (2023) e2216081. `doi:10.1080/00268976.2023.2216081`.

[9] J.-P. Karr, L. Hilico, J. C. J. Koelemeij, V. I. Korobov, Hydrogen molecular ions for improved determination of fundamental constants, Phys. Rev. A 94 (2016) 050501. `doi:10.1103/PhysRevA.94.050501`.

[10] W. J. Marciano, Time Variation of the Fundamental "Constants" and Kaluza-Klein Theories, Phys. Rev. Lett. 52 (1984) 489–491. `doi:10.1103/PhysRevLett.52.489`.

[11] S. Schiller, V. Korobov, Test of time-dependence of the electron and nuclear masses with ultracold molecules, Phys. Rev. A 71 (2005) 032505. `doi:10.1103/PhysRevA.71.032505`.

[12] S. Alighanbari, I. V. Kortunov, G. S. Giri, S. Schiller, Test of charged baryon interaction with high-resolution vibrational spectroscopy of molecular hydrogen ions, Nat. Phys. 19 (2023) 1263 – 1269. `doi:10.1038/s41567-023-02088-2`.

[13] G. Lüders, Proof of the TCP theorem, Annals of Physics 2 (1957) 1–15. `doi:10.1016/0003-4916(57)90032-5`.

[14] G. Schneider, A. Mooser, M. Bohman, N. Schön, J. Harrington, T. Higuchi, H. Nagahama, S. Sellner, C. Smorra, K. Blaum, Y. Matsuda, W. Quint, J. Walz, S. Ulmer, Double-trap measurement of the proton magnetic moment at 0.3 parts per billion precision, Science 358 (2017) 1081–1084. `doi:10.1126/science.aan0207`.

[15] M. J. Borchert, J. A. Devlin, S. R. Erlewein, M. Fleck, J. A. Harrington, T. Higuchi, B. M. Latacz, F. Voelksen, E. J. Wursten, F. Abbass, M. A. Bohman, A. H. Mooser, D. Popper, M. Wiesinger, C. Will, K. Blaum, Y. Matsuda, C. Ospelkaus, W. Quint, J. Walz, Y. Yamazaki, C. Smorra, S. Ulmer, A 16-parts-per-trillion measurement of the antiproton-to-proton charge-mass ratio, Nature 601 (2022) 53–57. `doi:10.1038/s41586-021-04203-w`.

[16] The ALPHA Collaboration, Investigation of the fine structure of antihydrogen, Nature 578 (2020) 375–380. `doi:10.1038/s41586-020-2006-5`.

[17] C. L. Cesar, Antihydrogen laser spectroscopy to 13 significant figures and beyond, in: International Conference on Precision Physics of Simple Atomic Systems, 2024. URL `https://indico.cern.ch/event/1329533/contributions/5917695/`

[18] H. Dehmelt, Economic synthesis and precision spectroscopy of anti-molecular hydrogen ions in Paul trap, Physica Scripta T59 (1995) 423–423. `doi:10.1088/0031-8949/1995/t59/060`.

[19] E. G. Myers, CPT tests with the antihydrogen molecular ion, Phys. Rev. A 98 (2018) 010101. `doi:10.1103/PhysRevA.98.010101`.

[20] S. Sellner, M. Besirli, M. Bohman, M. J. Borchert, J. Harrington, T. Higuchi, A. Mooser, H. Nagahama, G. Schneider, C. Smorra, T. Tanaka, K. Blaum, Y. Matsuda, C. Ospelkaus, W. Quint, J. Walz, Y. Yamazaki, S. Ulmer, Improved limit on the directly measured antiproton lifetime, New Journal of Physics 19 (2017) 083023. `doi:10.1088/1367-2630/aa7e73`.

[21] I. V. Kortunov, S. Alighanbari, M. G. Hansen, G. S. Giri, V. I. Korobov, S. Schiller, Proton-electron mass ratio by high-resolution optical spectroscopy of ion ensembles in the resolved-carrier regime, Nat. Phys. 17 (2021) 569–573. `doi:10.1038/s41567-020-01150-7`.

[22] V. I. Korobov, Precision Spectroscopy of the Hydrogen Molecular Ions: Present Status of Theory and Experiment, Physics of Particles and Nuclei 53 (2022) 787–789. `doi:10.1134/S1063779622040086`.

[23] S. Alighanbari, G. S. Giri, F. L. Constantin, V. I. Korobov, S. Schiller, Precise test of quantum electrodynamics and determination of fundamental constants with HD^+ ions, Nature 581 (2020) 152 – 158. `doi:10.1038/s41586-020-2261-5`.

[24] M. Germann, S. Patra, J.-P. Karr, L. Hilico, V. I. Korobov, E. J. Salumbides, K. S. E. Eikema, W. Ubachs, J. C. J. Koelemeij, Three-body QED test and fifth-force constraint from vibrations and rotations of HD^+, Phys. Rev. Research 3 (2021) L022028. `doi:10.1103/physrevresearch.3.l022028`.

[25] V. I. Korobov, J.-P. Karr, Rovibrational spin-averaged transitions in the hydrogen molecular ions, Phys. Rev. A 104 (2021) 032806. `doi:10.1103/PhysRevA.104.032806`.

[26] V. I. Korobov, J.-P. Karr, Spin-orbit interaction in the HD^+ ion, Eur. Phys. J. D 76 (2022) 197. `doi:10.1140/epjd/s10053-022-00522-3`.

[27] D. J. Fink, E. G. Myers, Deuteron-to-Proton Mass Ratio from Simultaneous Measurement of the Cyclotron Frequencies of H_2^+ and D^+, Phys. Rev. Lett. 127 (2021) 243001. `doi:10.1103/PhysRevLett.127.243001`.

[28] M. C. Zammit, M. Charlton, S. Jonsell, J. Colgan, J. S. Savage, D. V. Fursa, A. S. Kadyrov, I. Bray, R. C. Forrey, C. J. Fontes, J. A. Leiding, D. P. Kilcrease, P. Hakel, E. Timmermans, Laser-driven production of the antihydrogen molecular ion, Phys. Rev. A 100 (2019) 042709. `doi:10.1103/PhysRevA.100.042709`.

[29] J. Taylor, B. Vargo, D. Hoffman, T. J. Price, R. C. Forrey, Formation of antihydrogen molecular ions by associative ionization, Phys. Rev. A 109 (2024) 052816. `doi:10.1103/PhysRevA.109.052816`.

[30] S. Schiller, V. I. Korobov, Canceling spin-dependent contributions and systematic shifts in precision spectroscopy of molecular hydrogen ions, Phys. Rev. A 98 (2018) 022511. `doi:10.1103/PhysRevA.98.022511`.

[31] M. Haidar, V. I. Korobov, L. Hilico, J.-P. Karr, Higher-order corrections to the spin-orbit and spin-spin tensor interactions in HD^+, Phys. Rev. A 106 (2022) 042815. `doi:10.1103/PhysRevA.106.042815`.

[32] D. R. Bates, K. Ledsham, A. L. Stewart, Wave functions of the hydrogen molecular ion, Philosophical Transactions of the Royal Society of London A: Mathematical, Physical and Engineering Sciences 246 (1953) 215–240. `doi:10.1098/rsta.1953.0014`.

[33] R. Moss, Calculations for the vibration-rotation levels of H_2^+ in its ground and first excited electronic states, Molecular Physics 80 (1993) 1541–1554. `doi:10.1080/00268979300103211`.

[34] M. Born, R. Oppenheimer, Zur Quantentheorie der Molekeln, Annalen der Physik 389 (1927) 457–484. `doi:10.1002/andp.19273892002`.

[35] V. A. Johnson, Correction for Nuclear Motion in H_2^+, Phys. Rev. 60 (1941) 373–377. `doi:10.1103/PhysRev.60.373`.

[36] G. Paz, An introduction to NRQED, Modern Physics Letters A 30 (2015) 1550128. `doi:10.1142/S021773231550128X`.

[37] V. I. Korobov, Coulomb three-body bound-state problem: Variational calculations of nonrelativistic energies, Phys. Rev. A 61 (2000) 064503. `doi:10.1103/PhysRevA.61.064503`.

[38] V. I. Korobov, Variational methods in the quantum mechanical three-body problem with a coulomb interaction, Physics of Particles and Nuclei 53 (1) 1–20. `doi:10.1134/S1063779622010038`.

[39] V. I. Korobov, Leading-order relativistic and radiative corrections to the rovibrational spectrum of H_2^+ and HD^+ molecular ions, Phys. Rev. A 74 (2006) 052506. `doi:10.1103/PhysRevA.74.052506`.

[40] O. Kullie, S. Schiller, Solution of the two-center Dirac equation with 20-digit precision using the finite-element technique, Phys. Rev. A 105 (2022) 052801. `doi:10.1103/PhysRevA.105.052801`.

[41] H. D. Nogueira, J.-P. Karr, High-precision solution of the Dirac equation for the hydrogen molecular ion using a basis-set expansion, Phys. Rev. A 107 (2023) 042817. `doi:10.1103/PhysRevA.107.042817`.

[42] S. Alighanbari, M. R. Schenkel, V. I. Korobov, S. Schiller, subm.

[43] V. I. Korobov, L. Hilico, J.-P. Karr, Hyperfine structure in the hydrogen molecular ion, Phys. Rev. A 74 (2006) 040502. `doi:10.1103/PhysRevA.74.040502`.

[44] M. Haidar, V. I. Korobov, L. Hilico, J.-P. Karr, Higher-order corrections to spin-orbit and spin-spin tensor interactions in hydrogen molecular ions: Theory and application to H_2^+, Phys. Rev. A 106 (2022) 022816. `doi:10.1103/PhysRevA.106.022816`.

[45] J.-P. Karr, S. Patra, J. Koelemeij, J. Heinrich, N. Silltoe, A. Douillet, L. Hilico, Hydrogen molecular ions: new schemes for metrology and fundamental physics tests, in: F. Riehle (Ed.), 8th Symp. on Frequency Standards and Metrology 2015, Vol. 723 of Journal of Physics: Conference Series, 2016, p. 012048. `doi:10.1088/1742-6596/723/1/012048`.

[46] A. Dalgarno, T. N. L. Patterson, W. B. Somerville, The hyperfine structure of the hydrogen molecular ion, Proceedings of the Royal Society of London A: Mathematical, Physical and Engineering Sciences 259 (1961) 100–109. `doi:10.1098/rspa.1960.0213`.

[47] W. B. Somerville, A Revised Radio-Frequency Spectrum for H_2^+, Monthly Notices of the Royal Astronomical Society 147 (1970) 201–205. `doi:10.1093/mnras/147.2.201`.

[48] R. McEachran, C. Veenstra, M. Cohen, Hyperfine structure in the hydrogen molecular ion, Chemical Physics Letters 59 (1978) 275–280. `doi:10.1016/0009-2614(78)89095-2`.

[49] J. F. Babb, A. Dalgarno, Spin coupling constants and hyperfine transition frequencies for the hydrogen molecular ion, Phys. Rev. A 46 (1992) R5317–R5319. `doi:10.1103/PhysRevA.46.R5317`.

[50] K. B. Jefferts, Hyperfine Structure in the Molecular Ion H_2^+, Phys. Rev. Lett. 23 (1969) 1476–1478. `doi:10.1103/PhysRevLett.23.1476`.

[51] V. I. Korobov, J. C. J. Koelemeij, L. Hilico, J.-P. Karr, Theoretical Hyperfine Structure of the Molecular Hydrogen Ion at the 1 ppm Level, Phys. Rev. Lett. 116 (2016) 053003. `doi:10.1103/PhysRevLett.116.053003`.

[52] D. R. Bates, G. Poots, Properties of the Hydrogen Molecular Ion I: Quadrupole Transitions in the Ground Electronic State and Dipole Transitions of the Isotopic Ions, Proc. Phys. Soc. A 66 (1953) 784. `doi:10.1088/0370-1298/66/9/302`.

[53] A. G. Posen, A. Dalgarno, J. M. Peek, The quadrupole vibration-rotation transition probabilities of the molecular hydrogen ion, Atomic Data and Nuclear Data Tables 28 (1983) 265–277. `doi:10.1016/0092-640X(83)90017-7`.

[54] H. Olivares Pilón, D. Baye, Quadrupole transitions in the bound rotational-vibrational spectrum of the hydrogen molecular ion, Journal of Physics B: Atomic, Molecular and Optical Physics 45 (2012) 065101. `doi:10.1088/0953-4075/45/6/065101`.

[55] V. I. Korobov, P. Danev, D. Bakalov, S. Schiller, Laser-stimulated electric quadrupole transitions in the molecular hydrogen ion H_2^+, Phys. Rev. A 97 (2018) 032505. `doi:10.1103/PhysRevA.97.032505`.

[56] D. T. Aznabayev, A. K. Bekbaev, V. I. Korobov, Magnetic dipole transitions in the H_2^+ ion, Phys. Rev. A 108 (2023) 052827. `doi:10.1103/PhysRevA.108.052827`.

[57] V. I. Korobov, D. Bakalov, Forbidden ortho-para electric dipole transitions in the H_2^+ ion, Phys. Rev. A 107 (2023) 022812. `doi:10.1103/PhysRevA.107.022812`.

[58] C. Cohen-Tannoudji, B. Diu, F. Laloë, Quantum Mechanics, Volume II, Wiley-VCH, 2020.

[59] D. James, Quantum dynamics of cold trapped ions with application to quantum computation, Applied Physics B: Lasers and Optics 66 (1998) 181–190. `doi:10.1007/s003400050373`.

[60] S. Alighanbari, private communications.

[61] Q.-L. Tian, L.-Y. Tang, Z.-X. Zhong, Z.-C. Yan, T.-Y. Shi, Oscillator strengths between low-lying ro-vibrational states of hydrogen molecular ions, The Journal of Chemical Physics 137 (2012) 024311. `doi:10.1063/1.4733988`.

[62] H. Olivares Pilón, D. Baye, Dipole transitions in the bound rotational-vibrational spectrum of the heteronuclear molecular ion HD^+, Phys. Rev. A 88 (2013) 032502. `doi:10.1103/PhysRevA.88.032502`.

[63] D. Holzapfel, F. Schmid, N. Schwegler, O. Stadler, M. Stadler, J. Home, D. Kienzler, Quantum Logic Spectroscopy of the Hydrogen Molecular Ion, in: DPG Spring Meeting 2024 of the Atomic, Molecular, Quantum Optics and Photonics Section, 2024.
URL `https://www.dpg-verhandlungen.de/year/2024/conference/freiburg/part/q/session/26/contribution/6`

[64] J.-P. Karr, M. Haidar, L. Hilico, Z.-X. Zhong, V. I. Korobov, Higher-order corrections to spin-spin scalar interactions in HD^+ and H_2^+, Phys. Rev. A 102 (2020) 052827. `doi:10.1103/PhysRevA.102.052827`.

[65] S. C. Menasian, High resolution study of the $(F, F_2) = (3/2, 1/2) \rightarrow (1/2, 1/2)$ HFS transitions in stored H_2^+ molecular ions, Ph.D. thesis, University of Washington (1973).

[66] A. Carrington, C. A. Leach, M. R. Viant, Nuclear hyperfine structure in the electronic millimetre wave spectrum of H_2^+, Chemical Physics Letters 206 (1993) 77–82. `doi:10.1016/0009-2614(93)85520-X`.

[67] D. Holzapfel, F. Schmid, N. Schwegler, O. Stadler, M. Stadler, A. Ferk, J. P. Home, D. Kienzler, Quantum control of a single H_2^+ molecular ion (2024). `arXiv:2409.06495`.
URL `https://arxiv.org/abs/2409.06495`

[68] P. W. Arcuni, Z. W. Fu, S. R. Lundeen, Energy difference between the ($\nu = 0$, $R = 1$) and the ($\nu = 0$, $R = 3$) states of H_2^+, measured with interseries microwave spectroscopy of H_2 Rydberg states, Phys. Rev. A 42 (1990) 6950–6953. `doi:10.1103/PhysRevA.42.6950`.

[69] I. Doran, N. Hölsch, M. Beyer, F. Merkt, Zero-Quantum-Defect Method and the Fundamental Vibrational Interval of H_2^+, Phys. Rev. Lett. 132 (2024) 073001. `doi:10.1103/PhysRevLett.132.073001`.

[70] H. G. Dehmelt, Nobel lecture: Experiments with an isolated subatomic particle at rest (December 1989).
URL `https://www.nobelprize.org/prizes/physics/1989/dehmelt/lecture/`

[71] W. Paul, Nobel lecture: Electromagnetic traps for charged and neutral particles (December 1989).
URL `https://www.nobelprize.org/prizes/physics/1989/paul/lecture/`

[72] P. Blythe, B. Roth, U. Fröhlich, H. Wenz, S. Schiller, Production of ultracold trapped molecular hydrogen ions, Phys. Rev. Lett. 95 (2005) 183002. `doi:10.1103/PhysRevLett.95.183002`.

[73] B. Roth, J. C. J. Koelemeij, H. Daerr, S. Schiller, Rovibrational spectroscopy of trapped molecular hydrogen ions at millikelvin temperatures, Phys. Rev. A 74 (2006) 040501. doi:10.1103/PhysRevA.74.040501.

[74] J. Schmidt, T. Louvradoux, J. Heinrich, N. Sillitoe, M. Simpson, J.-P. Karr, L. Hilico, Trapping, Cooling, and Photodissociation Analysis of State-Selected H_2^+ Ions Produced by $(3+1)$ Multiphoton Ionization, Phys. Rev. Applied 14 (2020) 024053. doi:10.1103/PhysRevApplied.14.024053.

[75] Y. Zhang, Q.-Y. Zhang, W.-L. Bai, W.-C. Peng, S.-G. He, X. Tong, An efficient preparation of HD^+ molecular ions in an ion trap by REMPI, Chinese Journal of Physics 84 (2023). doi:10.1016/j.cjph.2023.01.004.

[76] C. Wellers, M. R. Schenkel, G. S. Giri, K. R. Brown, S. Schiller, Controlled preparation and vibrational excitation of single ultracold molecular hydrogen ions 120 (2022) e2001599. doi:10.1080/00268976.2021.2001599.

[77] N. Schwegler, D. Holzapfel, M. Stadler, A. Mitjans, I. Sergachev, J. P. Home, D. Kienzler, Trapping and Ground-State Cooling of a Single H_2^+, Phys. Rev. Lett. 131 (2023) 133003. doi:10.1103/PhysRevLett.131.133003.

[78] C. M. König, F. Heiße, J. Morgner, T. Sailer, B. Tu, K. Blaum, S. Schiller, S. Sturm, Hyperfine Spectroscopy of Single Molecular Hydrogen Ions in a Penning Trap at AL-PHATRAP, in: International Conference on Precision Physics of Simple Atomic Systems, 2022.
URL https://psas.fuw.edu.pl/program/

[79] H. Schnitzler, Development of an experiment for trapping, cooling, and spectroscopy of molecular hydrogen ions, Ph.D. thesis, Universität Konstanz (2001).

[80] U. Fröhlich, Coulomb Crystal Studies, Sympathetic Cooling, and Mass Spectrometry Using Laser-Cooled Be^+ Ions, Ph.D. thesis, Heinrich-Heine-Universität Düsseldorf (2008).

[81] S. Alighanbari, Frequency metrology of HD^+ by ultra-high resolution rotational spectroscopy, Ph.D. thesis, Heinrich-Heine-Universität Düsseldorf (2020).

[82] S. Alighanbari, M. G. Hansen, V. I. Korobov, S. Schiller, Rotational spectroscopy of cold and trapped molecular ions in the Lamb-Dicke regime, Nat. Phys. 14 (2018) 555. doi:10.1038/s41567-018-0074-3.

[83] M. Dunn, M. Ebrahim-Zadeh, Optical parametric oscillators, in: OSA Handbook of Optics, Vol. 4, McGraw-Hill, New York, 2000, pp. 2201–2272.

[84] Q.-F. Chen, A. Nevsky, M. Cardace, S. Schiller, T. Legero, S. Häfner, A. Uhde, U. Sterr, A compact, robust, and transportable ultra-stable laser with a fractional frequency instability of 1×10^{-15}, Rev. Sci. Instrum. 85 (2014) 113107. doi:10.1063/1.4898334.

[85] C. J. Kwong, M. G. Hansen, J. Sugawara, S. Schiller, Characterization of the long-term dimensional stability of a NEXCERA block using the optical resonator technique, Measurement Science and Technology 29 (2018) 075011. doi:10.1088/1361-6501/aac3b0.

[86] S. Häfner, S. Falke, C. Grebing, S. Vogt, T. Legero, M. Merimaa, C. Lisdat, U. Sterr, 8×10^{-17} fractional laser frequency instability with a long room-temperature cavity, Opt. Lett. 40 (2015) 2112–2115. doi:10.1364/OL.40.002112.

[87] A. Didier, J. Millo, C. Lacroûte, M. Ouisse, J. Delporte, V. Giordano, E. Rubiola, Y. Kersalé, Design of an ultra-compact reference ULE cavity, J. Phys. Conf. Ser. 723 (2016) 012029. `doi:10.1088/1742-6596/723/1/012029`.

[88] K. Predehl, G. Grosche, S. M. F. Raupach, S. Droste, O. Terra, J. Alnis, T. Legero, T. W. Hänsch, T. Udem, R. Holzwarth, H. Schnatz, A 920-kilometer optical fiber link for frequency metrology at the 19th decimal place, Science 336 (2012) 441–444. `doi:10.1126/science.1218442`.

[89] D. Husmann, L.-G. Bernier, M. Bertrand, D. Calonico, K. Chaloulos, G. Clausen, C. Clivati, J. Faist, E. Heiri, U. Hollenstein, A. Johnson, F. Mauchle, Z. Meir, F. Merkt, A. Mura, G. Scalari, S. Scheidegger, H. Schmutz, M. Sinhal, S. Willitsch, J. Morel, SI-traceable frequency dissemination at 1572.06 nm in a stabilized fiber network with ring topology, Opt. Express 29 (2021) 24592–24605. `doi:10.1364/OE.427921`.

[90] C. Clivati, M. Pizzocaro, E. Bertacco, S. Condio, G. Costanzo, S. Donadello, I. Goti, M. Gozzelino, F. Levi, A. Mura, M. Risaro, D. Calonico, M. Tønnes, B. Pointard, M. Mazouth-Laurol, R. Le Targat, M. Abgrall, M. Lours, H. Le Goff, L. Lorini, P.-E. Pottie, E. Cantin, O. Lopez, C. Chardonnet, A. Amy-Klein, Coherent Optical-Fiber Link Across Italy and France, Phys. Rev. Appl. 18 (2022) 054009. `doi:10.1103/PhysRevApplied.18.054009`.

[91] T. Schneider, B. Roth, H. Duncker, I. Ernsting, S. Schiller, All-optical preparation of molecular ions in the rovibrational ground state, Nat. Phys. 6 (2010) 275 – 278. `doi:10.1038/NPHYS1605`.

[92] W. Yang, R. Alheit, G. Werth, Vibrational population of H_2^+ after electroionization of thermal H_2, Z. Phys. D: At., Mol. Clusters 28 (1993) 87–88. `doi:10.1007/BF01436971`.

[93] G. Dunn, Photodissociation of H_2^+ and D_2^+: Theory and Tables (92) (1968) 1–54, JILA Pub. 381.

[94] Z. Amitay, D. Zajfman, P. Forck, Rotational and vibrational lifetime of isotopically asymmetrized homonuclear diatomic molecular ions, Phys. Rev. A 50 (1994) 2304–2308. `doi:10.1103/PhysRevA.50.2304`.

[95] J. C. J. Koelemeij, B. Roth, S. Schiller, Blackbody thermometry with cold molecular ions and application to ion-based frequency standards, Phys. Rev. A 76 (2007) 023413. `doi:10.1103/PhysRevA.76.023413`.

[96] R. H. Dicke, The effect of collisions upon the Doppler width of spectral lines, Phys. Rev. 89 (1953) 472–473. `doi:10.1103/PhysRev.89.472`.

[97] S. Patra, M. Germann, J.-P. Karr, M. Haidar, L. Hilico, V. I. Korobov, F. M. J. Cozijn, K. S. E. Eikema, W. Ubachs, J. C. J. Koelemeij, Proton-electron mass ratio from laser spectroscopy of HD^+ at the part-per-trillion level, Science 369 (2020) 1238–1241. `doi:10.1126/science.aba0453`.

[98] M. R. Schenkel, V. Vogt, S. Schiller, Metrology-grade spectroscopy source based on an optical parametric oscillator, Opt. Express 32 (2024) 43350–43365. `doi:10.1364/OE.538442`.

[99] M. R. Schenkel, S. Alighanbari, S. Schiller, Laser spectroscopy of a rovibrational transition in the molecular hydrogen ion H_2^+, Nature Physics 20 (2024) 383–388. `doi:10.1038/s41567-023-02320-z`.

[100] M. Germann, X. Tong, S. Willitsch, Observation of dipole-forbidden transitions in sympathetically cooled, state-selected, homonuclear diatomic molecular ions, Nat. Phys. 10 (2014) 820–824. `doi:10.1038/nphys3085`.

[101] P. O. Schmidt, T. Rosenband, C. Langer, W. M. Itano, J. C. Bergquist, D. J. Wineland, Spectroscopy using quantum logic, Science 309 (2005) 749–752. `doi:10.1126/science.1114375`.

[102] M. Sinhal, Z. Meir, K. Najafian, G. Hegi, S. Willitsch, Quantum-nondemolition state detection and spectroscopy of single trapped molecules, Science 367 (2020) 1213–1218. `doi:10.1126/science.aaz9837`.

[103] P. Marmet, L. Kerwin, Experimentally measured vibrational levels in H_2^+, Canadian Journal of Physics 38 (1960) 972–974. `doi:10.1139/p60-107`.

[104] L. Aasbrink, The photoelectron spectrum of H_2, Chemical Physics Letters 7 (1970) 549–552. `doi:10.1016/0009-2614(70)80169-5`.

[105] S. Takezawa, Absorption Spectrum of H_2 in the Vacuum-uv Region. II. Rydberg Series Converging to the First Six Vibrational Levels of the H_2^+ Ground State, The Journal of Chemical Physics 52 (1970) 5793–5799. `doi:10.1063/1.1672861`.

[106] G. Herzberg, C. Jungen, Rydberg series and ionization potential of the H_2 molecule, Journal of Molecular Spectroscopy 41 (1972) 425–486. `doi:10.1016/0022-2852(72)90064-1`.

[107] A. Carrington, I. R. McNab, C. A. Montgomerie, Microwave electronic spectrum of the H_2^+ ion, Chemical Physics Letters 160 (1989) 237–242. `doi:10.1016/0009-2614(89)87589-X`.

[108] Z. W. Fu, E. A. Hessels, S. R. Lundeen, Determination of the hyperfine structure of $H_2^+(\nu = 0, R = 1)$ by microwave spectroscopy of high-L, $n = 27$ Rydberg states of H_2, Phys. Rev. A 46 (1992) R5313–R5316. `doi:10.1103/PhysRevA.46.R5313`.

[109] A. Carrington, C. A. Leach, R. E. Moss, T. C. Steimle, M. R. Viant, Y. D. West, Microwave electronic spectroscopy, electric field dissociation and photofragmentation of the H_2^+ ion, J. Chem. Soc., Faraday Trans. 89 (1993) 603–614. `doi:10.1039/FT9938900603`.

[110] A. D. J. Critchley, A. N. Hughes, I. R. McNab, Direct measurement of a pure rotation transition in H_2^+, Phys. Rev. Lett. 86 (2001) 1725–1728. `doi:10.1103/PhysRevLett.86.1725`.

[111] A. Osterwalder, A. Wüest, F. Merkt, C. Jungen, High-resolution millimeter wave spectroscopy and multichannel quantum defect theory of the hyperfine structure in high Rydberg states of molecular hydrogen H_2^+, The Journal of Chemical Physics 121 (2004) 11810–11838. `doi:10.1063/1.1792596`.

[112] C. Haase, M. Beyer, C. Jungen, F. Merkt, The fundamental rotational interval of para-H_2^+ by MQDT-assisted Rydberg spectroscopy of H_2, The Journal of Chemical Physics 142 (2015) 064310. `doi:10.1063/1.4907531`.

[113] S. Cohen, J. R. Hiskes, R. J. Riddell, Vibrational States of the Hydrogen Molecular Ion, Phys. Rev. 119 (1960) 1025–1027. `doi:10.1103/PhysRev.119.1025`.

[114] H. Wind, Vibrational States of the Hydrogen Molecular Ion, The Journal of Chemical Physics 43 (1965) 2956–2958. `doi:10.1063/1.1697256`.

[115] V. I. Korobov, L. Hilico, J. P. Karr, Theoretical transition frequencies beyond 0.1 ppb accuracy in H_2^+, HD^+, and antiprotonic helium, Phys. Rev. A 89 (2014) 032511. `doi:10.1103/PhysRevA.89.032511`.

[116] W. B. Somerville, The radio-frequency spectrum of H_2^+, Mon. Not. R. astr. Soc. 139 (1968) 163. `doi:10.1093/mnras/139.2.163`.

[117] V. I. Korobov, L. Hilico, J.-P. Karr, Relativistic corrections of $m\alpha^6(m/M)$ order to the hyperfine structure of the H_2^+ molecular ion, Phys. Rev. A 79 (2009) 012501. `doi:10.1103/PhysRevA.79.012501`.

Nomenclature

BASE	Baryon Antibaryon Symmetry Experiment
BBR	Black-body radiation
CODATA	Commitee on Data (of the International Science Council)
CPT theorem	charge, paritiy and time reversal theorem
CW	continuous-wave
E1	electric-dipole (transition)
E2	electric-quadrupole (transition)
GNSS	global navigation satellite system
M1	magnetic-dipole (transition)
MHI(s)	molecular hydrogen ion(s)
NRQED	non-relativistic quantum electrodynamics
OFC	optical frequency comb
OPO	optical-parametric oscillator
PLL	phase-locked loop
QED	quantum electrodynamics
SHG	second-harmonic generation
SI	International System of Units
SM	Standard Model of particle physics
TICTES	Trapped ion cluster transverse excitation spectroscopy

List of Figures

List of Tables